# Charge and Spin Transport in Organic Systems: From Molecules to Materials

by

**Caleb Clever**

B.S., Muhlenberg College, 2016

Submitted to the Graduate Faculty of the

Dietrich School of Arts and Sciences in partial fulfillment

of the requirements for the degree of

Doctor of Philosophy

University of Pittsburgh

2023

UNIVERSITY OF PITTSBURGH

DIETRICH SCHOOL OF ARTS AND SCIENCES

This dissertation was presented

by

**Caleb Clever**

It was defended on

August 10, 2023

and approved by

Dr. Seth Horne, Professor, Department of Chemistry

Dr. Geoffrey Hutchison, Associate Professor, Department of Chemistry

Dr. Jeremy Levy, Distinguished Professor, Department of Physics and Astronomy

Dissertation Advisor: Dr. David Waldeck, Professor, Department of Chemistry

**Charge and Spin Electron Transport in Organic Systems:**
**From Molecules to Materials**

Caleb Clever, PhD

University of Pittsburgh, 2023

The nature of charge transport and the interplay between spin and chirality, manifested by the chiral induced spin selectivity (CISS) effect, are of prime importance to deepen our understanding of biochemical redox processes, as well as facilitate progress in fields such as spintronics and enantioseparation. In this dissertation, fundamental factors affecting charge and spin transport through biomolecules are investigated. The first study examines the pathways of charge transport through nucleic acids. It is determined that the electron transport occurs primarily through the base pair stack as opposed to the backbone. In the second study, we examine the transport of electrons through nucleic acids with a peptide backbone (PNA). The high conductivity of the basepair sequence $G_nC_n$ indicates a coherent transport mechanism, and differences in conductance between DNA and PNA are seen to arise from differences in cross-strand electronic coupling between the $G_nC_n$ segments. In the third study, an examination of the chiral induced spin selectivity (CISS) effect on small biomolecules are presented. A strong emphasis is also placed on establishing a robust terminology which can facilitate meaningful comparisons across experimental techniques. The fourth study presents preliminary data aimed at assessing the impact of spin control on different reaction mechanisms for the hydrogen evolution reaction, as determined by the choice of catalyst. The findings of these studies serve to advance the understanding of electron transport pathways and will aid in future studies of the interplay between charge, spin, and chirality.

## Table of Contents

## List of Tables

## List of Figures

## List of Equations

# 1.0 Introduction

## 1.1 Introduction to Molecular Electronics

The quest to continue the miniaturization of electronics is of interest to the development of smaller integrated circuits.[1] Almost sixty years ago, Aviram and Ratner theorized the use of single molecules as circuit components. The field of molecular electronics has progressed significantly since then.[2,3]

As the means of experimentally measuring the conductance properties of single molecules has improved, more emphasis has been directed towards delineating the mechanisms of charge transport and quantifying the factors which control charge transport across single molecules.

### 1.1.1 Studies in Single-Molecule Conductance: STM-Break Junction

The scanning tunneling microscope-based break junction technique (STM-BJ) has become widely favored for the study of the conductances of single molecules.[4-7] In this method, an STM tip is driven into a conductive substrate, on which a diffuse monolayer of molecules has been formed. Upon withdrawal of the tip, the metal-metal conductance between the tip and substrate breaks and as the tip retracts, the current decays exponentially from the saturation limit of metal-metal contact. If, however, a molecule from the surface adsorbs across the metal-metal contact to produce a molecular bridge (see Figure 1.1a), then electrical current will flow through the molecule and this allows the conductivity of the molecular junction to be

determined. The technique is demonstrated in Figure 1.1a. Figure 1.1b shows the current measured as the tip is withdrawn. Many thousands of measurements are collected and those which display molecular bridge conductance pathways are compiled to produce a conductance histogram (Figure 1.1c).[8] Commonly the tip and substrate are gold and the molecule of interest is dithiolated, exploiting the strong affinity for gold and sulfur to form a molecular junction.[9]

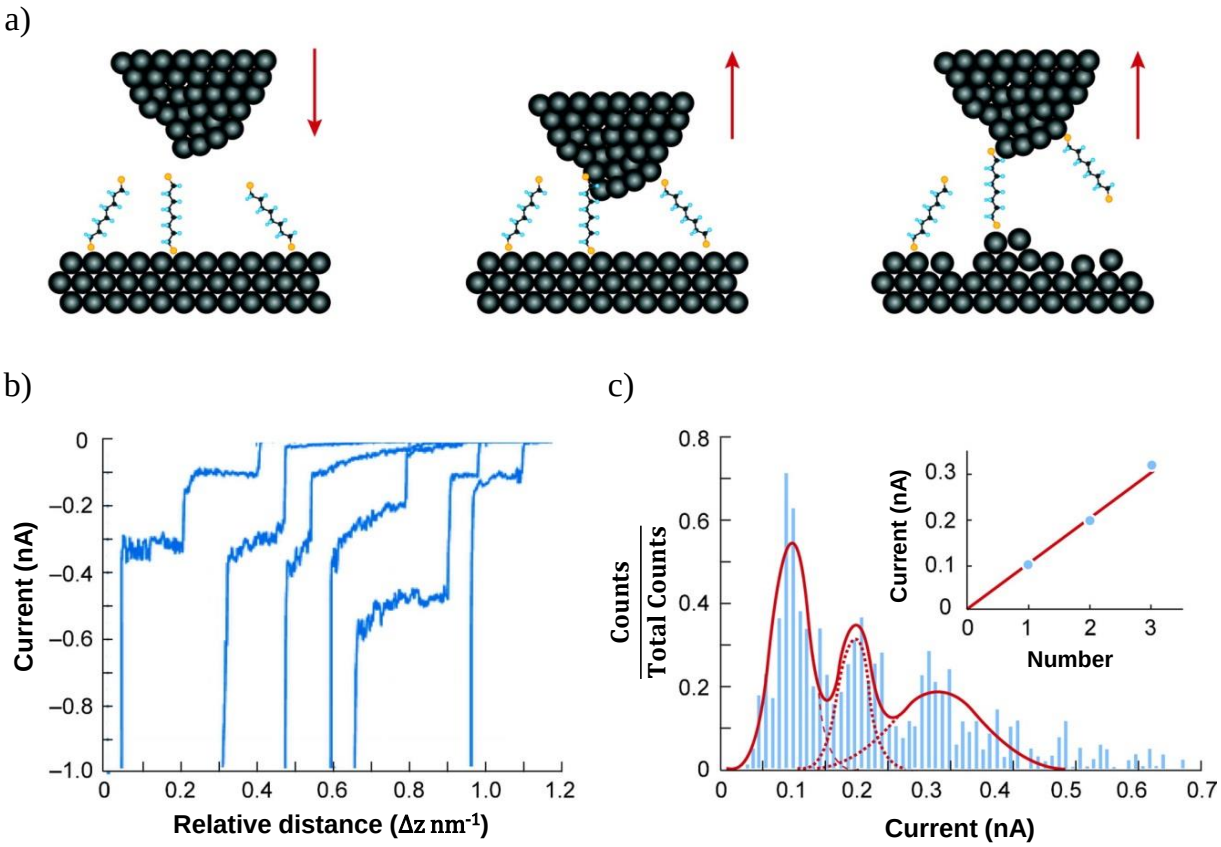


**Figure 1.1 A) The process of the STM-BJ technique is demonstrated. The black spheres represent Au atoms; the linkers on the termini of the molecules are shown as yellow spheres. Panel B shows the measured current during the withdrawal of the tip for six individual measurements, offset for clarity.. The plateaus correspond to a molecule trapped in the junction. The current responses are compiled into a conductance histogram (Panel C). Adapted from Reference 8.**

In an effort to garner more information and reduce noise, Beall *et al*. developed an STM-BJ technique using alternating current (AC).[7] Figure 1.2b shows an STM-BJ

measurement for 1,8-octanedithiol under a constant bias of 0.3 V. The plateaus in current response correspond to a molecule trapped in the junction. The same system measured using a triangle wave, AC bias of 0.3±0.3 V is presented in Figure 1.2c. Here the triangle peaks in the current response denote current flowing through a molecule trapped in the junction. The black traces and expanded plots show the current response where no molecule was in the junction, *i.e.* that of the mesitylene solvent.

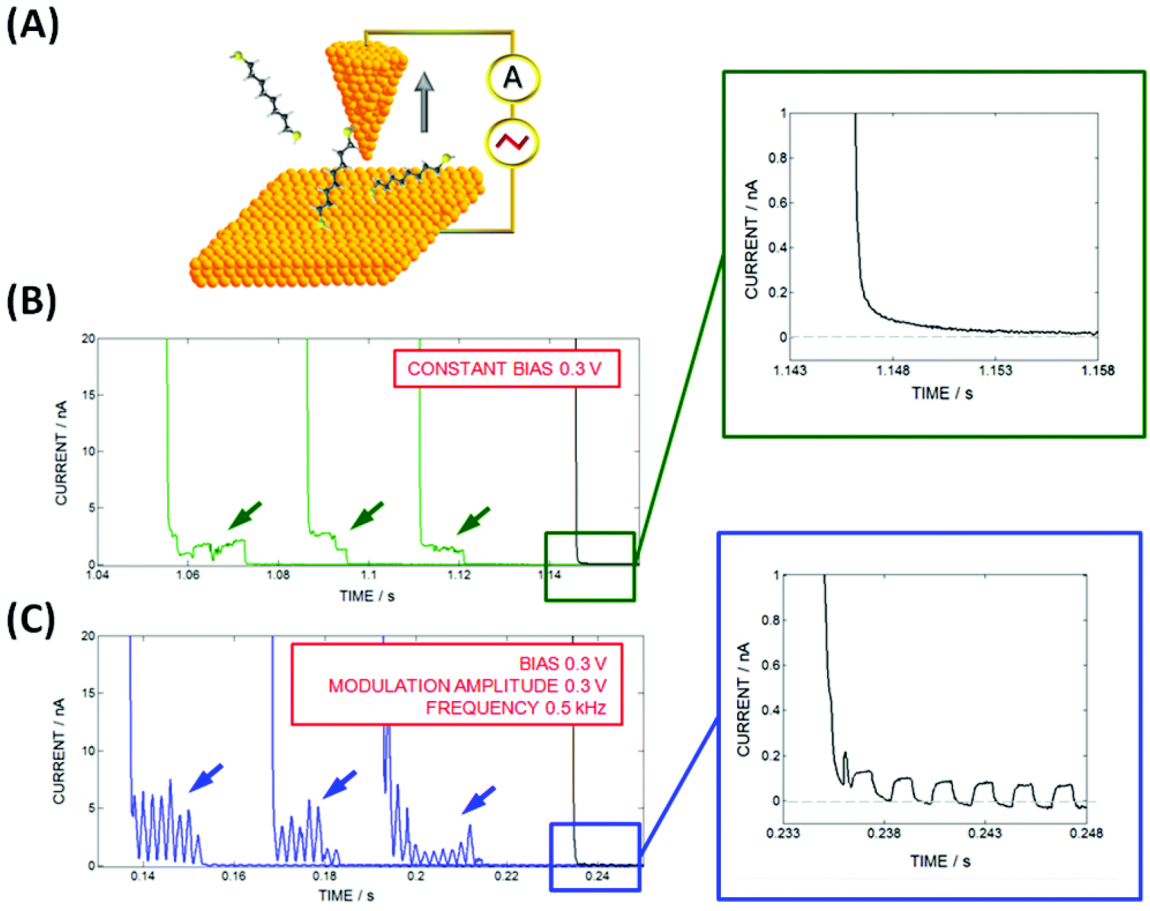


**Figure 1.2 A schematic of the AC STM-BJ measurement is shown in panel A. Panels B and C show sample current-time traces for the STM-BJ measurement with constant bias of 0.3V, and for an AC current of 0.3±0.3 V, respectively. Reprinted from Reference 7.**

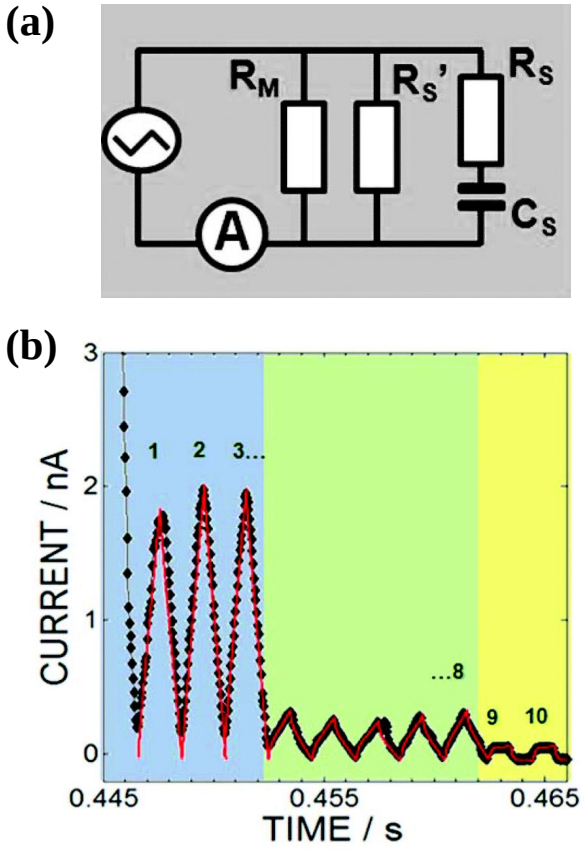


**Figure 1.3 Panel (a) shows the equivalent circuit used for fitting the conductance periods. $R_M$ denotes the resistance of the molecule in the junction and the solvent is modeled as a leaky capacitor with components $R_S$, $C_S$, and $R_S$'. The solvent parameters of the circuit were kept fixed ($R'_S = 1 \times 10^{11}$ Ω, $R_S = 9 \times 10^8$ Ω, $C_S = 8.25 \times 10^{-14}$ F). Panel (b) shows a conductance trace where the numbers delineate the conductance periods which were fit. Adapted from Reference 7.**

The resistance of the molecule in the junction is determined by fitting the conductance periods to an equivalent circuit, Figure 1.3a. The molecule is modeled as a simple resistor, in parallel with a 'leaky capacitor' to represent the solvent. This solvent conductance was measured in the absence of molecules and fit with a simulated current response to give the parameters listed in Figure 1.3. Figure 1.3b shows a sample current-time trace for the STM-BJ measurement. The blue region corresponds to the resistance of a molecule in the junction, $R_M$. As the tip withdraws, the binding geometry of the gold-thiol bond changes,[10] giving rise to

another, lower conductance mode. Typically the highest conductance mode is primarily reported. In the yellow region, the molecular junction has broken and the current response is solely due to the solvent, $R_S$', $R_S$, and $C_S$. The isolation of the current response due to the solvent allows for improved extraction of low-conductance data.

### 1.1.2 The Importance of Biomolecules

In the development of molecular electronics, biomolecules have been of interest due to their efficiency of charge transfer over large distances during biological processes.[11] While proteins account for a majority of nature's charge transfer[12], nucleic acids have been of interest for their tunability and ability to form well-defined architectures suitable for arrays of molecular circuit elements.[13,14] However the study of the mechanism of charge transfer in these systems continues to be a challenge.

In an effort to further develop the charge transport mechanisms of nucleic acid moieties, we studied a non-natural nucleic acid: peptide nucleic acid (PNA), in which the phosphate backbone of DNA is replaced with an amino ethyl glycine (aeg) chain (see Figure 1.4). While the phosphate backbone of DNA is negatively charged, the PNA backbone is uncharged. Consequently, the PNA backbone should be more flexible, facilitating an increased ability to align energy levels and promote coherent charge transport.[15] Indeed, PNA shows an order of magnitude greater conductance than DNA of the same basepair sequence, see Chapter 2. Additionally, while DNA shows strong oscillations in conductance with chain length, PNA shows significantly dampened oscillations. Theoretical analysis finds that this is the result of stronger electronic coupling across the nucleic acid strands in PNA, discussed in Chapter 3.

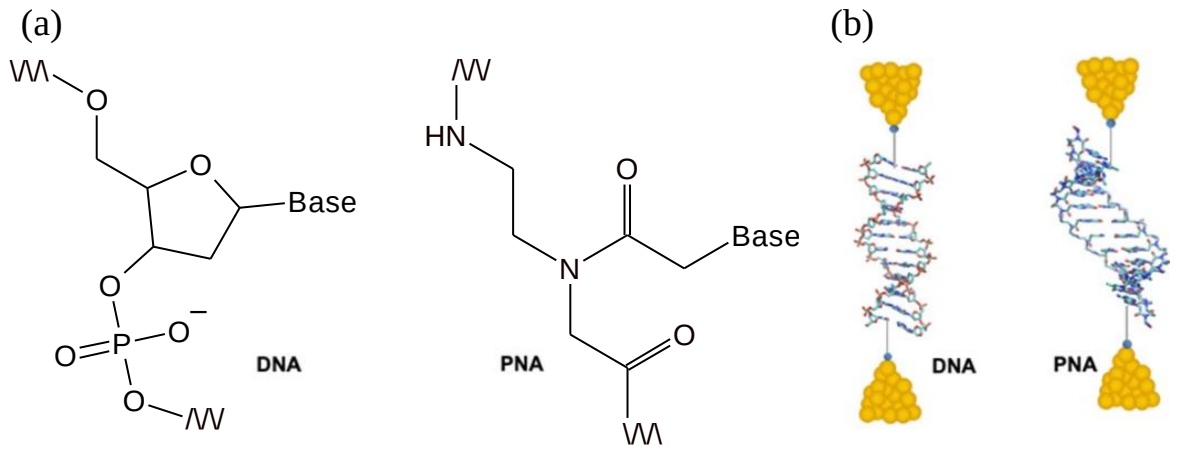


**Figure 1.4 Panel (a) shows the structures of the backbone of DNA (left) and PNA (right). Panel (b) shows the helical structure of DNA and PNA.**

Another important quality of biomolecules is their homochirality in nature, existing naturally as L-amino acids and D-sugars. The implications of this homochirality include the importance of spin transport in biomolecules, as dictated by the Chiral Induced Spin Selectivity (CISS) effect.

## 1.2 Spin Transport and the Chiral Induced Spin Selectivity (CISS) Effect

While much study has been done on electron charge transport, many of the models neglect the electron's intrinsic angular momentum, or spin.

In 1999 Waldeck *et al.* observed that electrons moving through a chiral molecule are selected preferentially based on their spin.[16] In this experiment spin-polarized photoelectrons were ejected using right-circularly, left-circularly, and linear polarized light (Figure 1.5, dashed, dotted, and solid lines, respectively) and the intensity of photoelectrons which passed through layers of L-stearoyl lysine were measured. It was observed that the intensity of photoelectrons

which passed through L-stearoyl lysine was higher for right-circularly polarized light. This correlation between spin-dependent electron transport and chirality is now called the Chiral Induced Spin Selectivity (CISS) effect.

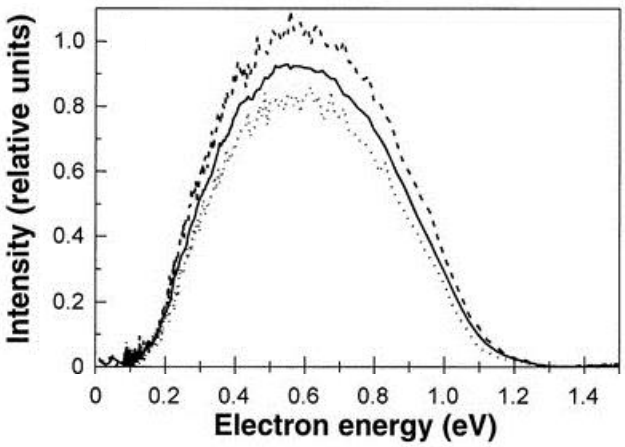


**Figure 1.5 Electron energy distribution for five layers of L-stearoyl lysine. The photoelectrons were ejected with linearly polarized light (solid line), right-handed circularly polarized light (dashed lines), and left-handed circularly polarized light (dotted lines). Adapted from Reference 16.**

The Chiral Induced Spin Selectivity (CISS) effect has been studied extensively, both from a mechanistic approach[17], as well as for applications such as enantioseparation[18,19], spintronics[20-23], and spin controlled chemical reactions.[24-26] In this chapter, the foundational concept of CISS and some important experiments and methods used to study it are discussed.

### 1.2.1 Some Principles of the CISS Effect

While the details of the situations which give rise to the CISS effect remain under debate, one leading model purports that a chiral molecule sets up a helical electric field within itself. Thus, when an electron moves through a chiral molecule, its movement produces a magnetic field in the electron's rest frame. This field splits the degeneracy of the electron's spin states; "spin up" and "spin down" electrons have different barriers to their motion. Therefore, when

electrons move through a chiral system, one spin state will be preferentially transmitted, its spin vector oriented either parallel or anti-parallel to its velocity. The strength of the magnetic field which the electron experiences is dependent on the Spin-Orbit Coupling (SOC) between the electron's momentum and its spin.[27-30] The Hamiltonian of SOC is given by Equation 1.1

$$H_{SOC} = \lambda\vec{\sigma} \cdot \left(\vec{p} \times \vec{E}_{chiral}\right) \quad \textbf{Equation 1.1}$$

where $\lambda=(e\hbar/(4m^2c^2)$, $\vec{p}$ is the momentum of the electron, $m$ is its mass, and $\vec{\sigma}$ is a vector composed of the Pauli matrices ($\sigma_x$, $\sigma_y$, $\sigma_z$). Indeed, qualitatively, theoretical efforts have confirmed that SOC affects the CISS response; however, quantitative calculations using SOC consistently underestimate the CISS response experimentally observed by several orders of magnitude.

Which spin state is preferred is dependent on the chirality of the system, i.e., opposite enantiomers show opposite preferred spin transmission. However, the precise mechanisms of the CISS effect and which structural features dictate which spin is preferred, and the strength of the spin filtering, remain under debate.[17,29-31]

### 1.2.2 Past Experiments Measuring CISS Response

In past studies of the CISS effect, an asymmetry term is used to compare measured signals, for L- and D- chirality, North and South magnetic field, or spin 'up and 'down' electrons

$$Asymmetry = \frac{A_1 - A_2}{A_1 + A_2} \quad \textbf{Equation 1.2}$$

where *A* denotes a measured signal.

Many experimental methods have been used over the years to study the CISS effect. While most are coupled with charge transport through a chiral system, such as magnetic

conductive probe atomic force microscopy (mc-AFM),[32] spin polarization can also be observed in situations with no current flow, such as the charge reorganization in a chiral system upon application of a polarizing voltage.[19]

### 1.2.3 Efforts to Normalize CISS Measurements

Much disparity exits in how CISS measurements are reported. For example, the common parlance of "spin up" and "spin down" is largely arbitrary. The reported preferred spin state is also heavily dependent on the experimental setup, making comparisons of different works unreliable. Additionally, different techniques to measure CISS can produce greatly different Asymmetry values (see Equation 1.2). The commonly used terms, such as 'spin up' versus 'spin down', do not provide values that are comparable across multiple measurement techniques and experiments. Therefore, in order to better quantify the CISS response, the percent spin polarization, *SP*, will be used here,

$$SP(\%) = \frac{A_{parallel} - A_{anti-parallel}}{A_{parallel} + A_{anti-parallel}} \qquad \textbf{Equation 1.3}$$

where $A_{parallel}$ ($A_{anti\text{-}parallel}$) denotes a measured signal where the electron's intrinsic angular momentum (spin) is oriented parallel (anti-parallel) to its velocity. Figure 1.6a shows an electron whose spin, σ, is aligned parallel to its velocity. It should be noted that the magnetic moment, μ, of the electron is always oriented opposite to its spin. Some of the methods that are frequently used to measure CISS are discussed below.

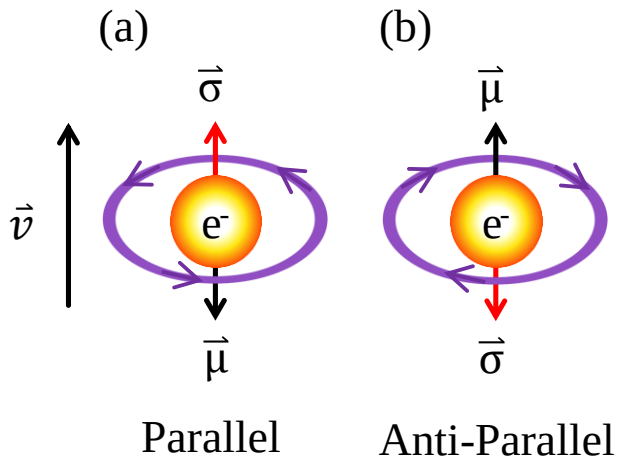


**Figure 1.6 Depiction of an improved nomenclature for CISS. The intrinsic angular momentum, σ, and corresponding magnetic moment, μ, are presented for electrons with their corresponding spins aligned parallel (left) and anti-parallel (right) to velocity.**

#### 1.2.3.1 Magnetic Conductive Probe-Atomic Force Microscopy

Magnetic conductive probe AFM (mc-AFM) is frequently used to study the spin polarization of electrons by a chiral molecule or film. Like conductive AFM, a potential difference is applied between the tip and substrate and the resulting current measured. However in mc-AFM, the tip (or the substrate) is magnetized such that one spin population is dominant. The resulting difference in current response when the magnetization direction or chirality is changed is used to measure the spin polarization.

#### 1.2.3.2 Hall Effect Devices

The Hall effect describes how moving charge in the presence of a magnetic field produces a voltage orthogonal to their velocity and the magnetic field.[33] Devices were designed so that a film of chiral material deposited on the surface, 20-30nm above a Ga/GaN two-dimensional electron gas (2DEG) conductive channel. An electrochemical cell of

polydimethylsiloxane is added to facilitate solution-phase measurements. A voltage is applied, insulated from current flow to produce a polarizable electrode and to charge polarize the film, which should also result in a magnetic field proportional to the spin polarization from the CISS effect. When current is driven through the 2DEG channel, this magnetization will manifest as a measurable Hall voltage perpendicular to the channel. Alternatively, electrochemical current is flowed through the chiral film while current is driven through the 2DEG channel and the spin filtering of electrons passing through the film will likewise result in a measurable Hall voltage.

#### 1.2.3.3 Photoemission

In 2011, Göhler *et al.* observed that photoelectrons ejected from a gold substrate which then pass through a double-stranded DNA (dsDNA) SAM, were spin polarized. They directly measured the spin of the electrons with a Mott polarimeter.[34] Figure 1.7 shows an experimental setup for a Mott polarimeter.[25] The technique is performed in ultrahigh vacuum, at $\approx 10^{-9}$ mbar. An ultraviolet (UV) laser pulse of a few hundred picoseconds, normal to the sample, ejects photoelectrons from the surface. The ejected electrons are guided by an electrostatic 90° bender and measured via Mott scattering from a gold foil. The asymmetry in the electron spin can then be calculated by Equation 1.2, with $A_1$ and $A_2$ representing the counts at the upper and lower detectors.

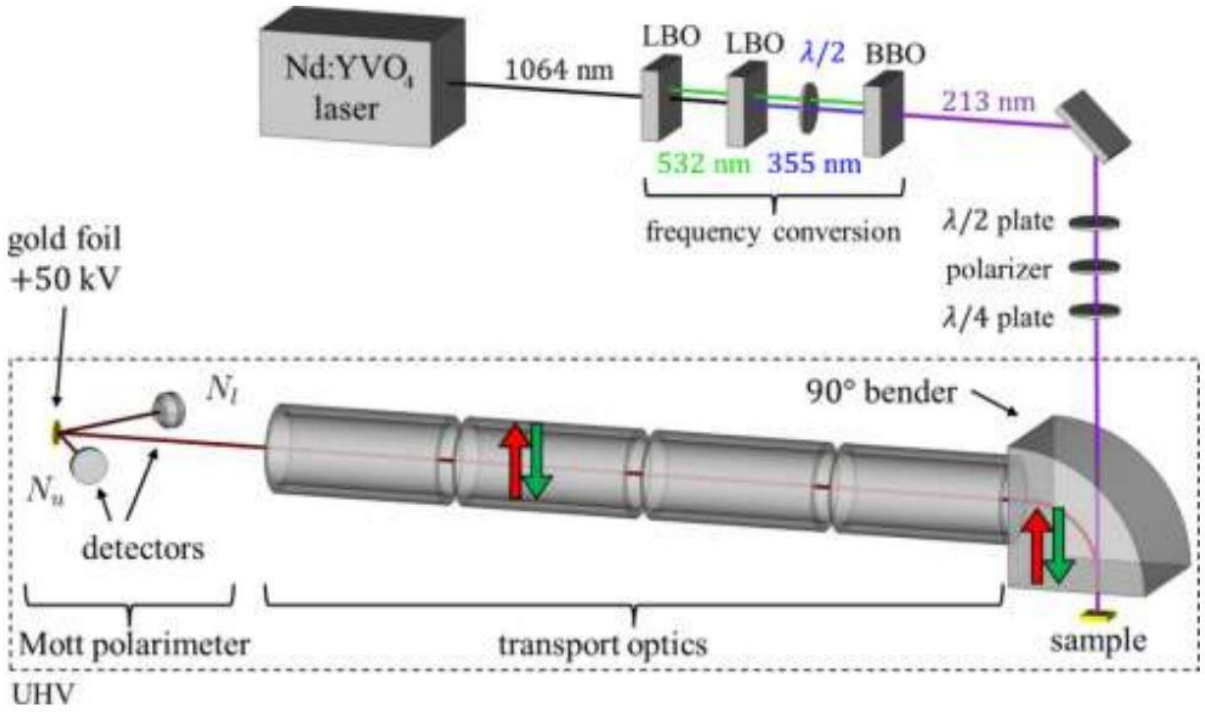


**Figure 1.7 An experimental setup for Mott polarimetry. Reprinted from Reference 25.**

### 1.2.3.4 Spin-Dependent Electrochemistry

The use of a ferromagnetic electrode in an electrochemical redox reaction can also facilitate the measurement of the spin polarization though a chiral SAM or film on the electrode surface. In this technique, the ferromagnetic electrode is used as the source of spin polarized electrons, and its magnetization is varied. As the spin polarized electrons pass through the chiral layer, one spin direction of the electron will be preferentially transmitted due to CISS. This selectivity results in an increase in redox current when the magnetization of the electrode and the chirality of the system interact constructively. The asymmetry in the electron spin can then be calculated by Equation 1.2, with $A_1$ and $A_2$ representing the redox current when the electrode is magnetized with a North or South magnetic field.

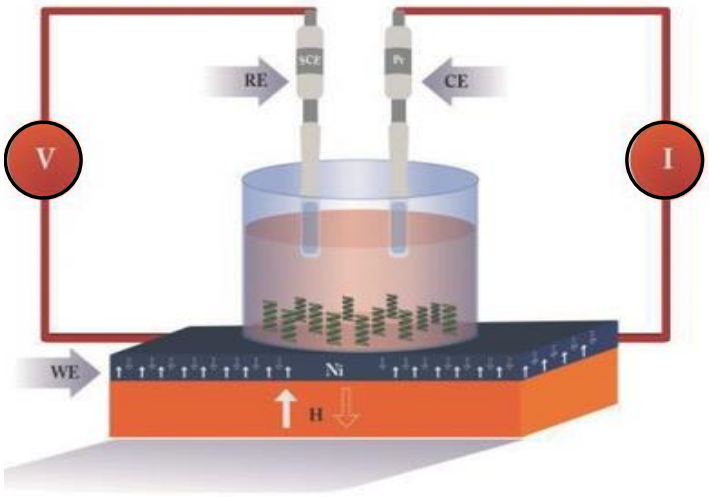


**Figure 1.8 An experimental setup for an electrochemical measurement of CISS. Figure is taken from Reference 35.**

### 1.2.3.4.1 Rotating Disk Electrode (RDE) Measurements

To better probe the changes in reaction mechanism, rotating disk electrode (RDE) measurements were conducted, where the working electrode is rotated and the laminar flow of the solution drives reactant to the electrode surface.[36] By altering the rotation rate, diffusion and kinetic current can be determined, as well as the rate constant, *k*, and the transfer coefficient, $\alpha$. Additionally, a ring around the working electrode can be used as a second electrode, held at an independent potential to probe the products which are formed, providing further information for the reaction pathway.

## 1.3 Importance of Spin Control in Reactions and its Applications

Interest in the effect of introducing spin-polarized electrons into a reaction has been growing stronger in recent years. Spin control has been shown to affect the reaction mechanism, rate-determining step, and formation of byproducts.[37]

The electrolysis of water is of great interest for applications related to energy production and storage. However, the high overpotential required hinders any applications. As the ground state of oxygen is a triplet, with aligned electron spins, introducing spin control results in a more favored reaction pathway, as no spin flip is needed to produce ground state oxygen. Spin control should improve parameters such as the reaction rate, overpotential, or Faradaic efficiency.[37]

Additionally, the hydrogen evolution half reaction is a competing reaction which hinders carbon dioxide or nitrogen reduction. Analogous to how oxygen's triplet ground state facilitates an easier evolution reaction upon the introduction of spin control, the ground state of hydrogen is a singlet and so should be hindered by aligned spins, allowing for decreased competition in the reduction of $CO_2$ or $N_2$. This is explored further in Chapter 5, where we control electron spin and measure reaction parameters for the hydrogen evolution reaction (HER) by means of magnetic rotating disk electrode (RDE) measurements.

## 1.4 Dissertation Outline

The CISS effect has already shown great promise in a variety of fields. Charge transport with controlled spin, without the need for a permanent magnet, has potential applications in molecular electronics, biological reactions, and photovoltaic cells, among others. However the

fundamental properties which give rise to it and what parameters can lead to a strong effect, remain uncertain. The work presented in this dissertation examines charge transport in biological molecules. Further, it seeks to elucidate some of the molecular properties upon which CISS depends. Finally it examines some important reactions and shows how CISS can improve their efficiency.

Chapter 2 reports on our work studying the conductivity of nucleic acid duplexes. In this study, a larger duplex is formed by the hybridization of two smaller strands, resulting in a nucleic acid strand with a 'nick' in the backbone. These nicked duplexes are shown to have similar conductance to the full duplexes, but with a higher variability in current response and lower stability.

Chapter 3 examines the mechanism of charge transport in nucleic acids by examining the dependence of the conductance of peptide nucleic acid (PNA) backbone compared to the same G-block ($G_nC_n$) basepair sequence on a DNA backbone. The PNA backbone displays a much higher conductance, up to ≈3% of the quantum of conductance, $G_0$, for 5 nm duplexes and shows a reduced even-odd effect of *n*-values on conductance.

Chapter 4 presents new CISS measurements on oligopeptides and amino acids, and compares them to a number of prior studies. We propose a means of robustly comparing *SP* across disparate measurement techniques and experiments. The dependence of the secondary structure, length, dipole moment, and the molecule/substrate interface on the magnitude and sign of the CISS response is critically analyzed in an effort to guide future studies.

Chapter 5 presents preliminary data on the effects of electron spin-control on water electrolysis, specifically for the hydrogen evolution reaction (HER). We use a rotating disk electrode to examine the rate and overpotential of HER on different metal catalysts, both

magnetized and non-magnetized. The introduction of magnetic field was seen to not alter the reaction mechanism.

## 1.5 References


1. Moore, G. E.; *Electronics* **1965**, *38*.
2. Aviram, A.; Ratner, M. A., *Chem. Phys. Lett.* **1974**, *29*, 277-283.
3. Baldea, I.; *Molecular Electronics: An Experimental and Theoretical Approach*; Pan Stanford, **2016**.
4. Reed, M. A.; Zhou, C.; *Science* **1997**, *278*, 252-254.
5. Cui, X. D.; Primak, A.; Zarate, X.; Tomfohr, J.; Sankey, O. F.; Moore, A. L.; Moore, T. A.; Gust, D.; Harris, G.; Lindsay, S. M.; *Science* **2001**, *294*, 571-574.
6. Xu, B.; Tao, N. J., *Science* **2003**, *301*, 1221-1223.
7. Beall, E.; Yin, X.; Waldeck, D. H.; Wierzbinski, E.; *Nanoscale*, **2015**, **7**, 14965-14973.
8. Chen, F.; Hihath, J.; Huang, Z.; Li, X.; Tao, N. J.; *Annu. Rev. Phys. Chem.* **2007**, *58*, 535-564.
9. Pensa, E.; Cortés, E.; Corthey, G.; Carro, P.; Vericat, C.; Fonticelli, M. H.; Benítez, G.; Rubert, A. A.; Salvarezza, R. C., *Acc. Chem. Res.*, **2012**, 45, 1183-1192.
10. Li, C.; Pobelov, I.; Wandlowski, T.; Bagrets, A.; Arnold, A.; Evers, F.; *J. Am. Chem. Soc.* **2008**, 130, 318−326.
11. Giese, B.; Graber, M.; Cordes, M.; *Curr. Opin. Chem. Biol*. **2008**, 12, 755-759.
12. Gray, H.; Winkler, J.; *Q. Rev. Biophys.* **2003**, 36, 341-372.
13. Pearson, A. C.; Liu, J.; Pound, E.; Uprety, B.; Woolley, A. T.; Davis, R. C.; Harb, J. N.; *J. Phys. Chem. B.* **2012**, 116, 10551–10560.
14. Hong, F.; Zhang, F.; Liu, Y.; Yan, H.; *Chem. Rev.* **2017**, 117, 12584–12640.
15. Wierzbinski, E.; de Leon, A.; Yin, X.; Balaeff, A.; Davis, K. L.; Reppireddy, S.; Venkatramani, R.; Keinan, S.; Ly, D. H.; Madrid, M.; *J. Am. Chem. Soc.*, **2012**, 134, 9335-9342.
16. Ray, K.; Ananthavel, S. P.; Waldeck, D. H.; Naaman, R.; *Science* **1999,** 283, 814.
17. Dalum, S.; Hedegård, P.; *Nano Lett.* **2019**, 19, 5253–5259.
18. Banerjee-Ghosh, K.; Dor, O. B.; Tassinari, F.; Capua, E.; Yochelis, S.;, Capua, A.; Yang, S-H.; Parkin, S. S. P.; Sarkar, S.; Kronik, L.; Baczewski, L. T.; Naaman, R.; Paltiel, Y.; *Science* **2018**, 360, 1331-1334.
19. Kumar, A.; Capua, E.; Kesharwani, M. K.; Martin, J. M. L.; Sitbon, E.; Waldeck, D. H.; Naaman, R.; *Proc. Natl. Acad. Sci. USA* **2017**, 114, 2474-2478.
20. Naaman, R.; Waldeck, D.H.; *Annu. Rev. Phys. Chem.* **2015**, 66, 263-281.
21. Dor, O. B.; Morali, N.; Yochelis, S.; Baczewski, L. T.; Paltiel, Y.; *Nano Lett.* **2014**, 14, 6042-6049.

22. Dor, O.; Yochelis, S.; Mathew, S.; Naaman, R.; Paltiel, Y.; A chiral-based magnetic memory device without a permanent magnet. *Nat Commun.*, **2013**, 4, 2256.

23. Koplovitz, G.; Primc, D.; Ben Dor, O.; Yochelis, S.; Rotem, D.; Porath, D.; Paltiel, Y.; *Adv. Mater.* **2017**, 29, 1606748.

24. Tassinari, F.; Steidel, J.; Paltiel, S.; Fontanesi, C.; Lahav, M.; Paltiel, Y.; Naaman, R.; *Chem. Sci.* **2019**, 10, 5246–5250.

25. Ghosh, K. B.; Zhang, W.; Tassinari, F.; Mastai, Y.; Lidor-Shalev, O.; Naaman, R.; Möllers, P.; Nürenberg, D.; Zacharias, H.; Wei, J.; Wierzbinski, E.; Waldeck, D. H.; *J. Phys. Chem. C* **2019**, 123, 3024–3031.

26. Mtangi, W.; Kiran, V.; Fontanesi, C.; Naaman, R.; *J. Phys. Chem. Lett.* **2015**, 6, 4916–4922.

27. Evers, F., Aharony, A., Bar-Gill, N., Entin-Wohlman, O., Hedegård, P., Hod, O., Jelinek, P., Kamieniarz, G., Lemeshko, M., Michaeli, K., Mujica, V., Naaman, R., Paltiel, Y., Refaely-Abramson, S., Tal, O., Thijssen, J., Thoss, M., van Ruitenbeek, J. M., Venkataraman, L., Waldeck, D. H., Yan, B., Kronik, L.; *Advanced Materials*, **2022**, 34, 2106629.

28. Dalum, S., Hedegård, P., *Nano Lett.*, **2019**, 19, 5253-5259.

29. Michaeli, K., Naaman, R., *J. Phys. Chem. C*, **2019**, 123, 17043-17048.

30. Naaman, R., Waldeck, D. H., *J. Phys. Chem. Lett.*, **2012**, 3, 2178-2187.

31. Yeganeh, S., Ratner, M. A., Medina, E., Mujica, V., *J. Chem. Phys.*, **2009**, 131, 014707.

32. Ghosh, S., Mishra, S., Avigad, E., Bloom, B.P., Baczewski, L.T., Yochelis, S., Paltiel, Y., Naaman, R. and Waldeck, D.H., *J. Phys. Chem. Lett.* **2020**, 11, 1550–1557.

33. Hall, E.H., *Am. J. Math.*, **1879**, 2, 287-292.

34. Göhler, B.; Hamelbeck, V.; Markus, T. Z.; Kettner, M.; Hanne, G. F.; Vager, Z.; Naaman, R.; Zacharias, H., *Science* **2011**, 331, 894-897.

35. Mondal, P. C., Kantor-Uriel, N., Mathew, S. P., Tassinari, F., Fontanesi, C., Naaman, R., *Adv. Mater.*, **2015**, 27, 1924-1927.

36. Xing, W., Yin, G., Zhang, J., *Rotating Electrode Methods and Oxygen Reduction Electrocatalysts*., Elsevier, **2014**.

37. Ghosh, S., Bloom, B. P., Lu, Y., Lamont, D., Waldeck, D. H., *J. Phys. Chem. C*, **2020**, 124, 22610-22618.

## 2.0 Molecular Conductance of Nicked Nucleic Acid Duplexes

This work was published as Beall, E., Sargun, A., Ulku, S., Bae, Y., Wierzbinski, E., Clever, C., Waldeck, D. H., Achim, C. *J. Phys. Chem. C* **2018**, *122*, 7533–7540. The author of the dissertation performed the conductance measurements, participated in the subsequent analyses, and participated in writing the manuscript. The supporting information for this chapter can be found in Appendix A.

This work investigates how the conductance of a nucleic acid duplex with a "nick" in its backbone compares with that of a duplex with a fully covalent backbone. Statistical analyses of the single-molecule conductance properties reveal that molecular junctions with a nicked duplex have an average conductance close to that found for non-nicked structures but exhibit greater variability in the molecular conductance. This effect is shown for both DNA homoduplexes and DNA/PNA heteroduplexes, with the heteroduplexes showing a greater average molecular conductance and a smaller degree of variability. The average molecular conductance of the heteroduplexes is also shown to be affected by their PNA content; the conductance of duplexes increases as the ratio of PNA to DNA increases. These observations suggest that the charge-transfer properties of nucleic acid-based assemblies can support complex functions.

### 2.1 Introduction

Since its inception,[1] molecular electronics has advanced to experimental realizations of molecules, which display a current−voltage behavior similar to that in an electronic device,

ranging from single-molecule diodes to the use of a protein as a transistor.[2,3] Driven by advancements in the fundamental understanding of charge transport through single molecules and larger biological systems,[4-7] efforts are being directed to the construction of increasingly intricate functional biomimetic structures.[8,9] Moreover, the promise of nucleic acid-based architectures to affect biochemical transformations and to function as logic and circuit elements is progressively bridging the gap between concept and device realization.[10,11] Schemes for assembling conductive nucleic acid platforms capable of providing long-range electrical communication are emerging and being explored. Studies of the mechanism of charge transfer in these systems continue to challenge our understanding and require new models to account for the important roles of molecular flexibility and molecule-bath coupling.[12-17] Self-assembly of DNA tiles and DNA origami into one-, two-, and three-dimensional structures rests on combining short and long oligonucleotides as building blocks.[18-20] Consequently, these structures contain nicks, that is, breaks in the backbone of the DNA at the junction between different oligonucleotides. The question arises whether and how these nicks affect charge transport through DNA in nanostructures. This question has been partially addressed by electron-transfer studies of DNA duplexes. In a study by Lewis et al., the photoinduced electron transfer from an electron donor to an electron acceptor via a nicked DNA duplex was measured and compared to that via a DNA duplex with an intact backbone.[21] This study showed that the rate constant for charge separation was not appreciably affected by the nick in the backbone of the duplex. In another study, Liu and Barton measured the electron transfer to a redox probe that was tethered to an electrode by a nicked DNA duplex and found that its efficiency was indistinguishable from electron transfer through a full DNA duplex (i.e., without a “nick” in the backbone of the same length).[22] This behavior was observed even for duplexes that contained

multiple nicks. To understand the relationship between the electron-transfer rate and the single-molecule conductance, researchers have compared the values of the electron-transfer rate and molecular conductance for systems with different compositions and molecular lengths.[23-26] They determined that a power law[25] correlates the electron-transfer rate and single-molecule conductance for molecular bridges. Given this correlation and the fact that the electron-transfer rate is not affected by the presence of a nick in the backbone of DNA duplexes, we anticipate that the molecular conductance of nucleic acid constructs should be independent of the presence of a nick. In this paper, we report the results of a project that aimed to test the hypothesis that a single nick does not affect the molecular conductance and to explore how the relative amounts of DNA and PNA in a duplex affect the conductance. We examined the effect of a nick on the single-molecule conductance of nucleic acid duplexes with different backbone compositions, namely, DNA homoduplexes and DNA/PNA heteroduplexes. PNA is a synthetic analogue of DNA that has a backbone based on N-(2-aminoethyl)glycine instead of the phosphodiester backbone of DNA.[27] The single-molecule conductances of the full and nicked nucleic acid duplexes were measured, and a statistical analysis was employed to assess the stability and variability of the molecular junctions between the scanning tunneling microscope (STM) tip and the substrate.

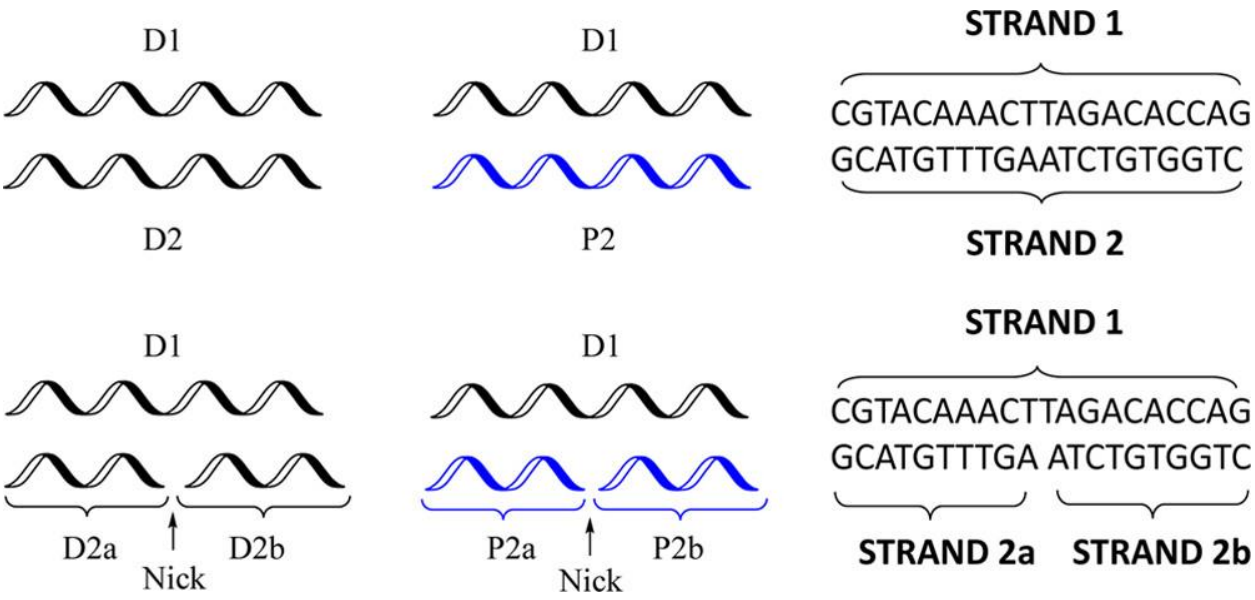


**Figure 2.1. The architectures of the full and nicked DNA homoduplexes and DNA/PNA heteroduplexes. The sequence of the top strand of each duplex is written in the 5'-to-3' direction for DNA and N-to-C direction for PNA. PNA strands (P) are shown in blue. DNA strands (D) are shown in black.**

Figure 2.1 shows the architecture of the full and nicked duplexes that were studied. The full duplexes are formed by the hybridization of two 20-base nucleic acid strands. The nicked duplexes have two 10-base strands that are hybridized to a 20-base template strand. In previous work, we showed that the molecular conductance of 10-base pair (bp) PNA duplexes is over 10 times larger than those of DNA homoduplexes and DNA/PNA heteroduplexes with the same sequence.[17] The duplex sequence used in that study was GCATGTTTGA (and its complement). The same 10-bp sequence is used as the "a" section of the 20-bp duplex sequence reported here (see Figure 2.1). We measure and compare the conductance for full and nicked versions of 20-bp DNA and PNA homoduplexes and 20-bp DNA/PNA heteroduplexes. In addition, these new data are compared with the earlier published data to ascertain how the conductance changes with the length of the duplexes.

## 2.2 Results

### 2.2.1 Characterization of the Nucleic Acids

The 10- and 20- bp homoduplexes of DNA and heteroduplexes of DNA/PNA were characterized by UV−vis absorbance, circular dichroism (CD), and fluorescence spectroscopies. These measurements provide information on the thermal stability and chirality of the full and nicked duplexes and allow us to conclude that both 10- base nucleic acid strands are present when templated with the 20-bp nucleic acid strand into a duplex.

#### 2.2.1.1 Melting Curves

The nick in the backbone significantly destabilizes the homo-DNA and hetero-DNA/PNA duplexes. Table 2.1 and Table A.3 contain the $T_m$ values for the full and nicked DNA and DNA/PNA duplexes, and Figure A.1 shows the typical UV melting data. The data show that the "nicked" DNA homoduplex (D1D2aD2b) and the nicked DNA/PNA heteroduplex (D1P2aP2b) are significantly less stable than their full versions (D1D2 and D1P2), with $\Delta T_m$ being more than 18°C. The melting temperatures indicate that the PNA homoduplexes are more stable than the DNA/PNA heteroduplexes, which in turn are more stable than the DNA homoduplexes. These differences are consistent with previous reports.[28] The melting temperature of the nicked 20-bp DNA/PNA duplexes is higher than that of 10-bp DNA/PNA duplexes, as one would expect given the lengths of these duplexes.[17]

**Table 2.1. Melting Temperatures ($T_m$) of Nucleic Acid Duplexes**

| | **Chemical Nature of Strands** | **$T_m$/°C** |
|---|---|---|
| Full Duplex | P1/P2 | >90 |
| | D1/D2 | 45 |
| | D1/P2 | 85 |
| Nicked Duplex | D1/D2a/D2b | 21 |
| | D1/P2a/P2b | 67 |
| | P1/P2a/D2b | 68 |

### 2.2.1.2 CD Spectra

Figure 2.2 shows the CD spectra for the full and nicked DNA homoduplexes and DNA/PNA heteroduplexes. The spectra of the DNA/PNA heteroduplexes show the biphasic exciton coupling pattern characteristic of a right-handed helix. The signal intensity for the nicked duplexes is similar to that of the full duplexes, which indicates that the nick does not affect the structure of the duplex.

### 2.2.1.3 Fluorescence Spectra for the DNA/PNA Heteroduplexes

The ratio of the intensity of the excimer emission (PL480) to the intensity of the pyrene monomer emission (PL400) was used to assess whether both 10-base PNA strands are bound to the template in the nicked 20-bp DNA/PNA heteroduplex. This method is based on the fact that when two pyrene moieties are in close proximity to each other, π-stacking can occur and excimer emission can be observed at $\lambda_{max}$ = 480 nm.[29] Figure 2.3a shows the location of the pyrene in the nicked PNA/DNA duplexes. Figure 2.3b shows the fluorescence spectra for the three schemes of the DNA/PNA heteroduplexes. On the basis of the number of pairs of adjacent pyrenes and of isolated pyrenes in the different motifs, the PL480/PL400 ratio should decrease in the order scheme 1 > scheme 2 ≈ scheme 3. Indeed, this trend is displayed by the fluorescence

spectra (see Figure 2.3b), which show PL480/PL400 ratios of 5.3, 1.6, and 2.4 for schemes 1, 2, and 3, respectively. This result substantiates the presence of the three strands D1, P2a, and P2b in the nicked DNA/PNA heteroduplexes.

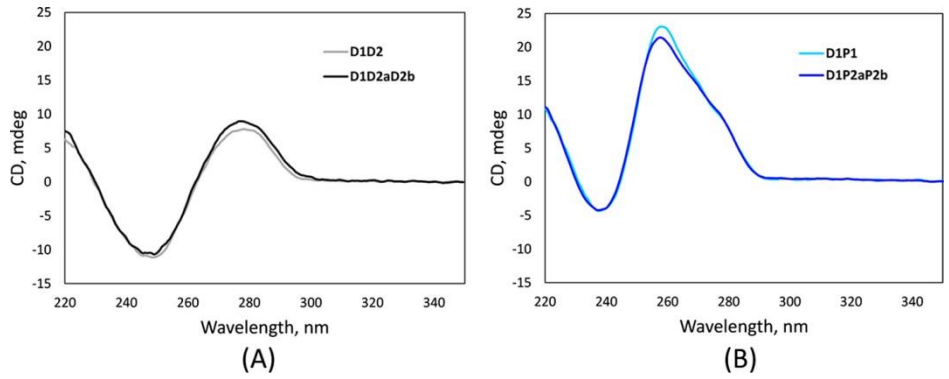


**Figure 2.2 CD spectra for the full and nicked DNA homoduplexes (A) and the full and nicked DNA/PNA heteroduplexes (B).**

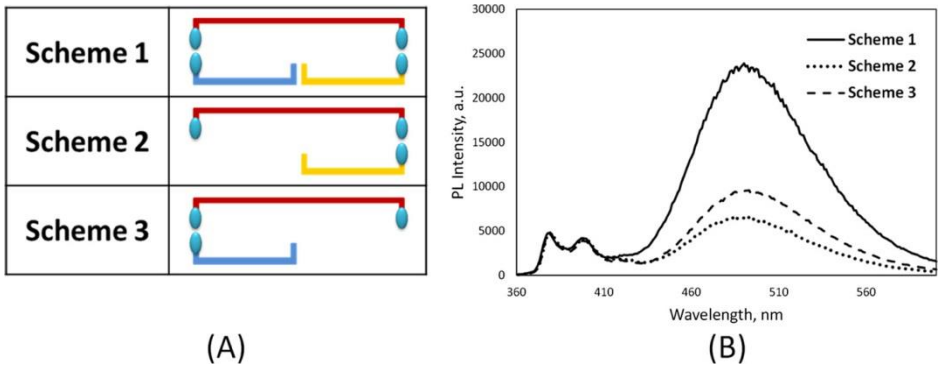


**Figure 2.3 (A) Three pyrene labeling schemes for the duplexes. The red lines represent the 20-base DNA template strand. The blue and yellow lines represent the 10-base PNA strands. The blue ellipses represent the pyrenes. (B) Fluorescence spectra for pyrene-labeled DNA/PNA heteroduplexes. The solid, dotted, and dashed lines correspond to schemes 1, 2, and 3, respectively. The data have been scaled to have an equivalent intensity at $\lambda = 400$ nm.**

### 2.2.2 Effect of the Nick on the Conductance of the Duplexes

Single-molecule conductance measurements were performed on 20-bp duplexes using the STM break junction (STM-BJ) method with a continuous bias modulation.[17,30,31] Propylthiol units were introduced at the two termini of the DNA and DNA/PNA duplexes to facilitate the formation of thiol linkages to the Au surfaces. In the conductance measurement, a gold STM tip is driven to the surface of a gold substrate, which is covered by a diffuse layer of the nucleic acid duplexes. Molecular junctions can form between the gold substrate and the STM tip via thiol linkers on opposing strands of a duplex. As the STM tip is retracted from the surface, a triangular waveform bias voltage is applied across the gap and the current between the substrate and the tip is measured. This process provides a time profile of the current, which is converted to a distance.

Thousands of current responses, or trajectories, are collected for each duplex type and filtered to remove trajectories that do not contain a molecular junction. The filtered set provides a distribution of current responses, which is analyzed and converted into conductance histograms. The discretized manner in which the bias is applied causes the current responses to be discretized. An example of the discretization of a current−time response for a DNA homoduplex is shown in Figure 2.4a. The trajectories are partitioned by the periods of the modulated current response, and each period is indexed. The periods in the current response are fitted, and every fitted period has an associated conductance value, G(n), where the index, n, identifies the period number.

Panels B and E of Figure 2.4 show conductance histograms for the full DNA homoduplex, the full DNA/PNA heteroduplex, the nicked DNA duplex, and the nicked DNA/PNA duplex. On the abscissa, the conductance is scaled by $G_0 = 2e^2/h = 77.5\ \mu S$, the

quantum of conductance.[32] Each duplex shows a peak corresponding to the most probable molecular conductance and a smaller second peak at a conductance of twice the value of the first peak. In each case, the histogram was fit by two Gaussian functions to extract the most probable conductance (Figure A.3). The peak at twice the conductance value was assigned to molecular junctions involving two molecules bound across the gap. Panels C through G of Figure 2.4 show conductance histograms as a function of the period number of the trajectory. The conductance for the full DNA duplex remains the same for more periods (Figure 2.4c), as compared to the nicked version (Figure 2.4d). The heteroduplexes show less of a difference in conductance and have a behavior more like that of the full DNA duplex (Figure 2.4f and Figure 2.4g), implying that their integrity is better preserved.

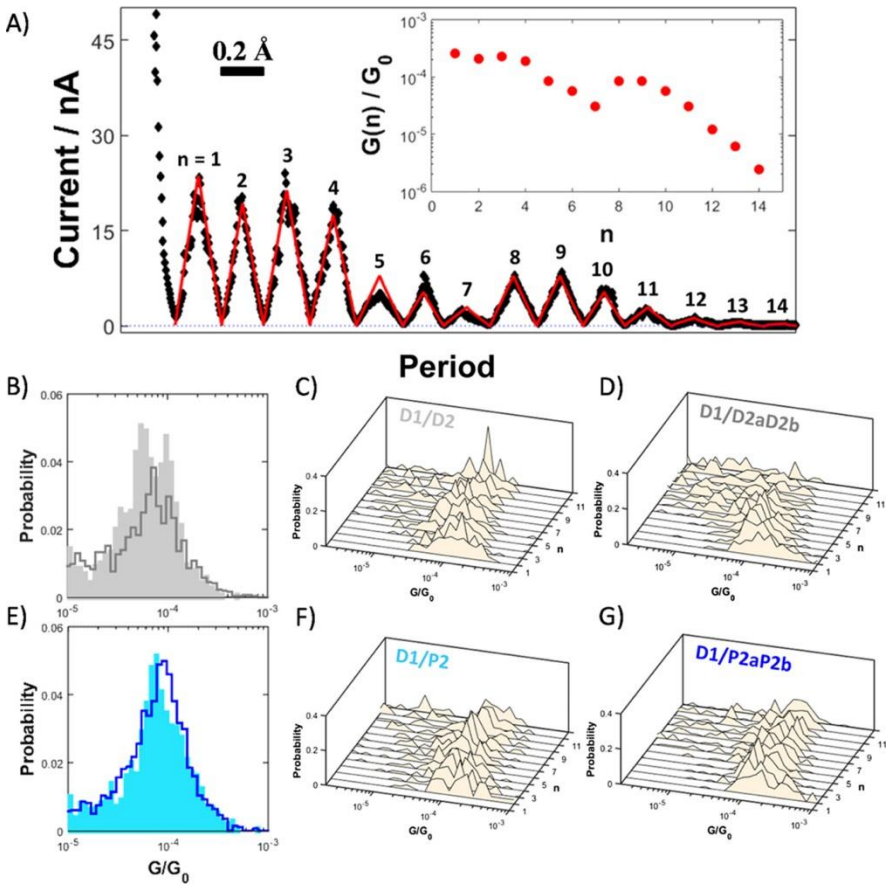


**Figure 2.4 (A) Example current−time I(t) trajectory of a full DNA molecular junction is shown (black) with the fitted current response overlaid (red). Each period is 2 ms in duration, the STM tip retracts 0.2 Å during each current response period, and the bar shown in panel A gives the length scale. The inset shows the fitted conductance, G(n), for each period in the current response. Conductance histograms are shown for the full DNA duplex (shaded cells) with the nicked analogue (unfilled cells) overlaid (B) and the full DNA/PNA duplex (shaded cells) with the nicked analogue (unfilled cells) overlaid (E). Three-dimensional plots of conductance histograms for specific periods of the current responses are shown for all four duplexes (C,D,F,G).**

The full 20-bp DNA homoduplex has a most probable conductance of $5.5 \times 10^{-5}G_0$, and the full DNA/PNA heteroduplex has a value of $7.4 \times 10^{-5}G_0$. The conductance of the 20-bp DNA/PNA duplex is roughly 5 times smaller than that found for 10-bp DNA/PNA heteroduplexes.[17] Both nicked duplexes have most probable conductance values that are

slightly larger than those for the full versions of each duplex. The nicked 20-bp DNA homoduplex has a most probable conductance value of $8.4 \times 10^{-5}G_0$; and the nicked DNA/PNA heteroduplex has a most probable value of $7.9 \times 10^{-5}G_0$. These increases, albeit small, over the full 20-bp duplexes (see Table 2.2) can be rationalized by a larger backbone flexibility of the nicked duplexes,[17] which may allow for improved couplings between π-orbitals in the base stack. This supposition is supported by the observation that the histograms for the nicked duplexes have a broader distribution, reflected by the larger standard deviations of the Gaussian functions used to fit the histograms, than the corresponding full duplexes. The standard deviations for both nicked duplexes are approximately twice those for the full DNA and DNA/PNA duplexes (Table 2.2). The increase in the flexibility can also be quantitatively evaluated through a statistical analysis of the individual trajectories (vide infra). The fact that the conductance of the 20-bp DNA/PNA full or nicked heteroduplex is slightly larger than that of the 20-bp DNA full or nicked duplex with the same sequence is similar to the relationship observed between the conductances of 10-bp DNA homoduplexes and DNA/PNA heteroduplexes.[17] This modest enhancement of the conductance was attributed to a greater flexibility for the DNA/PNA heteroduplex compared to the DNA homoduplex.

**Table 2.2 Summary of the single molecule conductance, *G*, and its standard deviation, $\sigma_G$, for the nucleic acid duplexes.**

| Duplex | $G$ ($\times 10^{-5}G_0$) | $\sigma_G$ ($\times 10^{-5}G_0$) |
|---|---|---|
| DNA | 5.5 | 1.9 |
| Nicked DNA | 8.4 | 3.6 |
| DNA/PNA | 7.4 | 1.4 |
| Nicked DNA/PNA | 7.9 | 4.1 |
| Nicked PNA/PNA:DNA | 20 | 12 |
| PNA/PNA | 57 | 41 |

In the spirit of recent correlation analyses,[33-36] a conductance correlation treatment was employed to evaluate the differences in the conductances of full and nicked duplexes for various periods. Figure 2.5 shows the two-dimensional correlation plots for the full DNA, full DNA/PNA, and their nicked versions. Within each trajectory, the fitted conductance value for a given period, *n*, was correlated with the fitted conductance value for another period, *k*. The correlation parameters between periods were averaged over the set of collected trajectories for each duplex. Similarity between conductance values results in a high degree of correlation and a greater correlation parameter, whereas variations between the conductance values of periods *n* and *k* result in a lower correlation parameter. Thus, fluctuations of the conductance within a trajectory lead to a loss in correlation. For example, Figure 2.5a shows a high degree of correlation between periods 2 and 3, suggesting that these periods will have a high degree of similarity in the fitted conductance value, on average. However, periods 2 and 10 have very little correlation, indicating that the fitted conductance values are significantly different between these periods, on average. The two-dimensional correlation plots are symmetric about the diagonal because the correlation between periods *n* and *k* is equivalent to the correlation between periods *k* and *n*. The correlation equals one along the diagonal when $n = k$.

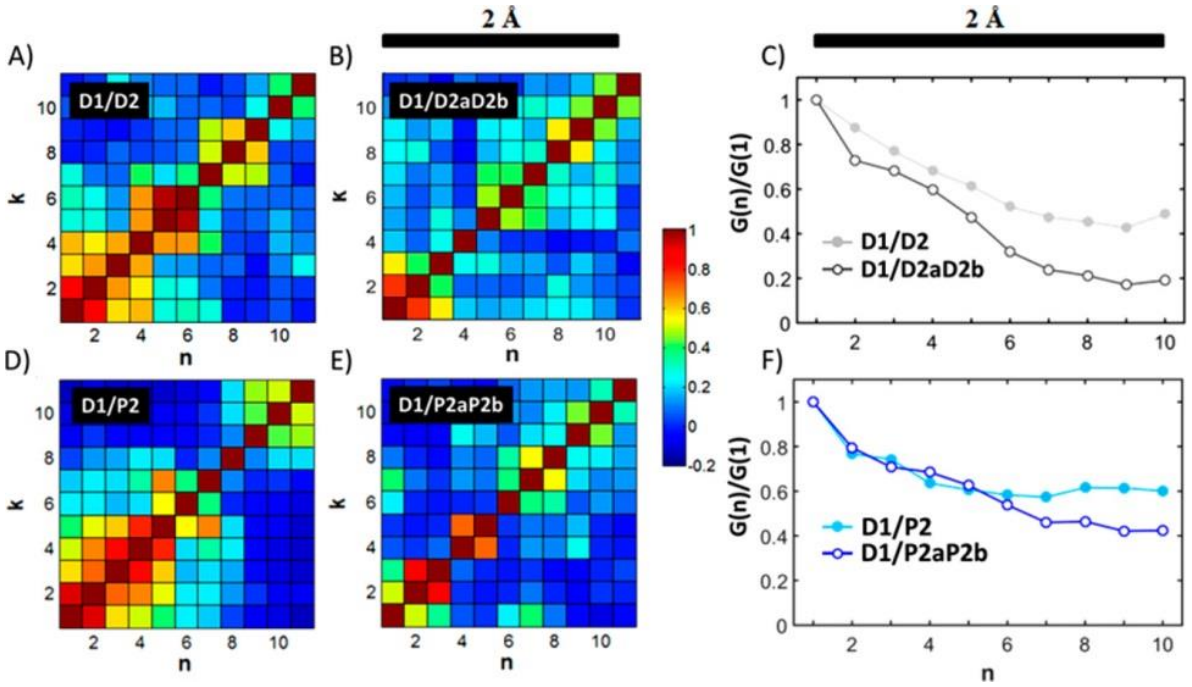


**Figure 2.5 Two-dimensional correlation plots for the full DNA (A), full DNA/PNA (D), and nicked duplexes (B) and (E). Each square represents the correlation between the conductance values for given periods n and k. By nature, the correlation has a value of one along the diagonal when n = k. Panels C and F show the average ratio of the fitted conductance for period n to the fitted conductance for period 1. The total displacement over ten current response periods is 2 Å.**

Figure 2.5a and Figure 2.5b show the two-dimensional correlation plots for the full and nicked DNA duplexes; whereas Figure 2.5d and Figure 2.5e show the plots for the full and nicked heteroduplexes. In both cases, the plots show noticeably less correlation for the nicked duplexes, indicating that the fitted conductance values vary more for the nicked duplexes. This lessened correlation is represented by the lower correlation parameters adjacent to the diagonal for the nicked duplexes, suggesting that the fitted conductance values are more variable between proximal current response periods. This analysis supports the supposition that the nicked duplexes are more flexible than their full counterparts.

The ratio of the conductance value for each period in the current response to the conductance value of the first period was calculated and averaged over the entire set of

trajectories. The results of this analysis are shown in Figure 2.5c and Figure 2.5f. The ratios show that the correlation for the full duplexes (D1/D2 and D1/ P2) extends to longer periods; that is, the full version of the nucleic acid duplex has a higher conductance value at later periods relative to the first current response period. As the molecular junctions transition to lower conductance modes in later periods of the trajectory,[37,38] the correlation in the conductance decreases to a greater extent for the nicked duplexes than for the full duplexes. Thus, the nicked duplexes form less stable molecular junctions than the full duplexes.

### 2.2.3 Effect of the PNA Content on Conductance

Figure 2.6 compares conductance histograms for the 20-bp DNA/PNA heteroduplex, a 20-bp PNA homoduplex (P1/P2), and a nicked PNA/PNA:DNA heteroduplex (P1/P2a/D2b). The latter two duplexes are different from the ones shown in Figure 2.4. The PNA homoduplex has 20 PNA/PNA bps; the nicked PNA/ PNA:DNA duplex has 10 PNA/PNA bp hybridization and 10 DNA/PNA bps; and the PNA/DNA heteroduplex has 20 DNA/PNA bps. In each case, the histograms are fit by Gaussian functions to best identify the most probable conductance. For the PNA/PNA:DNA heteroduplex shown in Figure 2.6, the thiol linkers are present on the PNA strands. However, the conductance of a duplex linked through a thiol on the 10- base DNA strand was measured; and the observed conductance histograms are similar to those observed for the duplexes with the thiol on the 10-base PNA strand (see Appendix A). Note that the fits for the PNA homoduplex and the nicked heteroduplex include multiple conductance modes, referred to as high and medium modes. Such modes have been attributed to different binding motifs for the thiol on the Au surface.[38] The most probable values for the high-conductance mode of the duplexes are reported in Table 2.2. The PNA homoduplex displays a most probable conductance

value that is approximately 10 times larger than those of the DNA homoduplex and the nicked DNA/PNA heteroduplex, but only 3 times larger than the most probable conductance for the nicked PNA/PNA:DNA heteroduplex. These increases are consistent with previous findings for 10-bp DNA and PNA homoduplexes and DNA/PNA heteroduplexes.[17,25,39] Note that the ratio between the values of the high-conductance mode and medium-conductance mode for the data shown in Figure 2.6 is similar to the previously reported ratio for thiol-terminated molecules, suggesting that the interaction between the duplex and electrode is exclusively through the thiol−Au linkage rather than directly through the duplex nucleobase stack.[37,38] The values of the molecular conductance of the duplexes shown in Table 2.2 show that the molecular conductance increases as the number of PNA nucleobase pairs in the duplex increases. This relationship could allow the conductance of a duplex of a given length to be tuned by its PNA content. In previous work, we have discussed how the duplex geometry and flexibility change between PNA and DNA.[12,17]

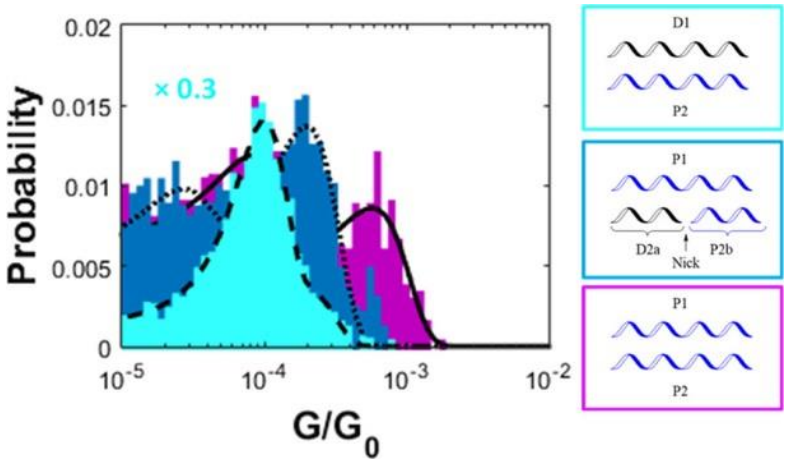


**Figure 2.6 Conductance histograms for the full DNA/PNA heteroduplex (turquoise), the full PNA homoduplex (magenta), and the nicked PNA/PNA:DNA heteroduplex (blue). The black curves in each case are fits by a sum of two Gaussian functions. For the purposes of comparison, the height of the histogram for the full DNA/PNA heteroduplex is scaled by a factor of 0.3.**

The fact that the conductance of the 20-bp PNA duplex is an order of magnitude greater than that of the DNA 20-bp duplex is consistent with the previous finding of a 12-fold increase in the conductance of a PNA 10-bp duplex over that of a DNA duplex with the same sequence.[17] The nicked versions of the DNA and DNA/PNA show slightly larger conductance than the full duplexes; however, the distribution of the conductance values for the nicked duplexes is broader than that of full duplexes. The nicked PNA/PNA:DNA heteroduplex shows a greater conductance than both the nicked and full DNA/PNA heteroduplexes. Multiple correlation analyses of the trajectories for the full DNA and DNA/PNA duplexes versus their nicked analogues show that the current responses vary more and the number of periods in a trajectory is smaller, on average, for the nicked duplexes, suggesting that the conductance through the nicked systems is less stable.

## 2.3 Discussion

An investigation of the effect of a backbone nick on the single-molecule conductance of DNA and PNA duplexes indicates that the conductance values of the nicked duplexes are similar to those of full duplexes despite the fact that both the thermal stability of the nicked duplexes and the stability of the molecular junctions for the nicked duplexes are lower. Conductance ratios for trajectory periods relative to the first period show that the nicked duplexes experience a drop in the conductance at earlier periods of the trajectory, implying a lower integrity (Figure 2.5). Further, the standard deviations of the fitted Gaussian functions of the conductance histograms for the nicked DNA homoduplex and DNA/PNA heteroduplex are greater than the standard deviations for their full analogues (see Table 2.2). These observations indicate that the presence

of a nick in the backbone of the molecular bridge reduces the stability of the molecular junction and increases the variability of its single-molecule conductance.

The influence of the PNA content on the conductance of the duplex was examined. The single-molecule conductance varies over a range of almost an order of magnitude depending on the relative amount of DNA and PNA strands comprising a duplex of a given length and with a specific linker. The conductance decreased from the duplex with the greatest PNA content to that of the nicked PNA/PNA:DNA heteroduplex to that of the duplex with the lowest PNA content.

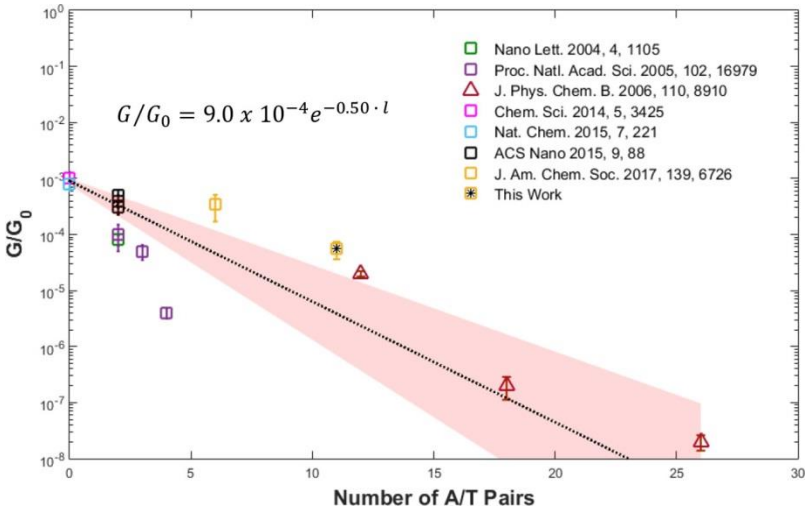


**Figure 2.7 Conductance values for DNA duplexes as a function of A/T content of the duplex measured by various methods. In the conductance measurements, the DNA was attached to the surface by three-carbon (C3) thiol linkers. The squares identify the conductance measured by the STM-BJ method. The triangles identify values measured by atomic force microscopy conductance utilizing a gold nanoparticle. The dashed line indicates the best fit function; and the shaded region shows a 95% confidence interval for the best fit.**

The measured conductance of the 20-bp duplexes is approximately 5 times smaller than that reported for shorter 10-bp DNA duplexes with a similar mixed nucleobase sequence.[17] This decrease in conductance with the length of the duplex is consistent with that expected by extrapolating the dependence on bridge length of the DNA molecular conductance determined in

earlier studies.[25,39] Figure 2.7 shows a plot of the logarithm of recently reported highest conductance values measured for 6- to 26-bp DNA duplexes versus the number of A/T bps in the duplexes. [17,39-44] This analysis assumes that the G/C bps do not contribute to the "effective" tunneling length and that the number of A/T pairs dictates the conductance. This assumption is based on the conclusion of recent studies indicating that G/C pairs are much less resistive than A/T pairs.[43,45] The data are reasonably fit by an exponential decay function $G/G_0 = 9.0 \times 10^{-4} \exp(-0.50 \cdot l)$, where $l$ is the number of A/T bps. The pre-exponential term indicates the conductance of a strand with an effective length of zero bps, which corresponds to two linker lengths or one hexanedithiol. This value lies between the high-conductance mode value of $1.3 \times 10^{-3} G_0$ and the medium-conductance mode value of $3.4 \times 10^{-4} G_0$ reported for hexanedithiol.[46] The shaded region in the plot of Figure 2.7 shows a 95% confidence interval for the best fit. Omission of the apparent outlier with four A/T bps results in an exponential fit with a similar decay constant and pre-exponential term, still falling within the aforementioned conductance values for hexanedithiol. Using a pitch of 0.33 Å per bp, one calculates a characteristic decay length parameter of 1.5 per Å for the A/T bps. A plot of these conductance data versus the total number of bps shows that the exponential dependence is lost when G/C bps are included in the length count; see Appendix A.

## 2.4 Conclusions

A comparison of the full and nicked versions of DNA homoduplexes and DNA/PNA heteroduplexes has shown that the presence of a nick in the backbone of the duplex results in a lowered thermal stability and a greater variability in the molecular conductance compared to

duplexes without the nick in the backbone. The melting temperature of the nicked nucleic acid duplex is considerably lower than that of its full analogue in both cases. Whereas the nicked duplexes exhibit an average molecular conductance, which matches that for the full version in each case, the conductance values of the nicked duplexes show increased variability over the lifetime of the molecular junction, suggesting that the nick affects the integrity of the duplex. One can therefore expect the conductance of supramolecular assemblies comprising smaller nicked components to maintain the conductance of structures composed of larger strands but suffer from increased variability in molecular conductance.

## 2.5 Methods

### 2.5.1 PNA Synthesis

All reagents were purchased from commercial suppliers and used as received. Boc/Z and Fmoc/Bhoc PNA monomers were purchased from PolyOrg Inc. and ASM Research Chemicals, respectively, and used without further purification. The synthesis of the pyrene PNA oligomers is outlined in Appendix A. HPLC was performed on a system that included a Waters 600 controller and a Waters 2996 photodiode array detector. Characterization of the oligomers was performed by matrix-assisted laser desorption ionization time-of-flight mass spectrometry on an Applied Biosystems Voyager Biospectrometry workstation with delayed extraction.

Melting temperature experiments were performed in 10 mm path length quartz cells on a Varian Cary 300 spectrophotometer equipped with a programmable temperature block. PNA stock solutions were prepared in deionized (DI) water and were stored at −25 °C. The PNA

solutions for UV and CD experiments were prepared in 10 mM pH 7.0 phosphate buffer. PNA concentrations were determined by UV−vis spectrophotometry assuming ε(260) = 8600, 6600, 13 700, and 11 700 $cm^{-1}$ $M^{-1}$ for each T, C, A, and G monomer, respectively.[47] The extinction coefficients for pyrene at 90 °C were measured: ε(260) = 12 711 and ε(345) = 28 319 $cm^{-1}$ $M^{-1}$. All CD data were recorded at room temperature; and the spectra represent an average of 10 scans, recorded from 350 to 220 nm at a rate of 50 nm/min. A 1 cm path length cuvette was used. Excitation and emission spectra were obtained using a Cary Eclipse fluorimeter. Emission spectra were recorded with a 0.2 ms delay time and a 5 ms gate time in the range 360−600 nm with selective irradiation at 345 nm ($\lambda_{ex}$ = 345 nm).

### 2.5.2 Conductance Measurements

#### 2.5.2.1 Substrate Fabrication

Template-stripped[48] Au substrates were created by evaporating 100 nm gold films onto freshly cleaved mica (AJA ATC-T Series Thermal Evaporation System). The gold films were transferred to Piranha-cleaned glass slips (10 mm × 25 mm) prior to each experiment. Duplex solutions (50 μL, 20 μM) were deposited, and the terminal thiols were allowed to bind to the gold substrates for less than 20 s. The substrates were washed with DI water and ethanol (200 proof) and dried under a stream of argon.

#### 2.5.2.2 Data Collection

All conductance measurements were performed using an Agilent 5500 scanning probe microscope system. An environmental chamber was housed in a homemade acoustically isolated Faraday cage seated on an antivibrational system (Table Stable). The gold STM tips (0.25 mm,

99.95% gold wire, Alfa Aesar) were freshly cut prior to each experiment. All experiments were performed under an argon atmosphere, and the gold substrates were immersed in mesitylene. A triangular 0.3 ± 0.3 V bias with a modulation frequency of 500 Hz was applied across the substrate/STM tip gap (Stanford Research Systems, DS345 Function Generator). All measurements were performed using a 10 nA/V preamplifier.

#### 2.5.2.3 Data Analysis

Data filtering and analysis were performed using a custom MATLAB code. The current−time trajectories were filtered to remove trajectories that did not display molecular junctions (i.e., "empty" trajectories). Each trajectory is partitioned into periods through a fit to the modulated applied bias. The employed correlation treatment was adopted from previous studies[26-29] but modified to correlate the fitted conductance value from each conductance period.

## 2.6 References


1. Aviram, A.; Ratner, M. A., *Chem. Phys. Lett.* **1974**, 29, 277-283.
2. Perrin, M. L.; Galan, E.; Eelkema, R.; Thijssen, J. M.; Grozema, F.; van der Zant, H. S. J., *Nanoscale*, **2016**, 8, 8919-8923.
3. Chen, Y.-S.; Hong, M.-Y.; Huang, G. S., *Nat. Nanotechnol.* **2012**, 7, 197-203.
4. McCreery, R. L.; Yan, H.; Bergren, A. J., *Phys. Chem. Chem. Phys.* **2013**, 15, 1065-1081.
5. Amdursky, N.; Marchak, D.; Sepunaru, L.; Pecht, I.; Sheves, M.; Cahen, D., *Adv. Mater.* **2014**, 26, 7142-7161.
6. Guldi, D. M.; Nishihara, H.; Venkataraman, L., *Chem. Soc. Rev.* **2015**, 44, 842-1027.
7. Alessandrini, A.; Facci, P., *Eur. Polym. J.* **2016**, 83, 450-466.
8. Facci, P., *Biomolecular Electronics: Bioelectronics and the Electrical Control of Biological Systems and Reactions*; Elsevier: Waltham, MA, **2014**.
9. Baldea, I., Ed.; *Molecular Electronics: An Experimental and Theoretical Approach;* Pan Stanford: Singapore, **2016**.
10. Pearson, A. C.; Liu, J.; Pound, E.; Uprety, B.; Woolley, A. T.; Davis, R. C.; Harb, J. N., *J. Phys. Chem. B*, **2012**, 116, 10551-10560.
11. Hong, F.; Zhang, F.; Liu, Y.; Yan, H., *Chem. Rev.*, **2017**, 117, 12584-12640.
12. Lu, Q.; Liu, K.; Zhang, H.; Du, Z.; Wang, X.; Wang, F., *ACS Nano*, **2009**, 3, 3861-3868.
13. Venkatramani, R.; Keinan, S.; Balaeff, A.; Beratan, D. N., *Coord. Chem. Rev.*, **2011**, 255, 635-648.
14. Wierzbinski, E., de Leon, A., Yin, X., Balaeff, A., Davis, K.L., Reppireddy, S., Venkatramani, R., Keinan, S., Ly, D.H., Madrid, M. and Beratan, D.N., *J. Am. Chem. Soc.* **2012**, 134, 9335-9342.
15. Zhang, Y.; Liu, C.; Balaeff, A.; Skourtis, S. S.; Beratan, D. N., *Proc. Natl. Acad. Sci. U.S.A.* **2014**, 111, 10049-10054.
16. Li, G.; Govind, N.; Ratner, M. A.; Cramer, C. J.; Gagliardi, L., *J. Phys. Chem. Lett.* **2015**, 6, 4889-4897.
17. Beall, E.; Ulku, S.; Liu, C.; Wierzbinski, E.; Zhang, Y.; Bae, Y.; Zhang, P.; Achim, C.; Beratan, D. N.; Waldeck, D. H., *J. Am. Chem. Soc.*, **2017**, 139, 6726-6735.
18. Strano, M. S., *Science*, **2012**, 338, 890-891.
19. Pinheiro, A. V.; Han, D.; Shih, W. M.; Yan, H., *Nat. Nanotechnol.*, **2011**, 6, 763-772.
20. Seeman, N. C., *Structural DNA Nanotechnology*; Cambridge University Press: Cambridge, U.K., 2016.
21. Lewis, F. D.; Wu, Y.; Zhang, L.; Zuo, X.; Hayes, R. T.; Wasielewski, M. R., *J. Am. Chem. Soc.*, **2004**, 126, 8206-8215.

22. Liu, T.; Barton, J. K., *J. Am. Chem. Soc.*, **2005**, 127, 10160-10161.

23. Traub, M. C.; Brunschwig, B. S.; Lewis, N. S., *J. Phys. Chem. B*, **2007**, 111, 6676-6683.

24. Zhou, X.-S.; Liu, L.; Fortgang, P.; Lefevre, A.-S.; Serra-Muns, A.; Raouafi, N.; Amatore, C.; Mao, B.-W.; Maisonhaute, E.; Schöllhorn, B., *J. Am. Chem. Soc.*, **2011**, 133, 7509-7516.

25. Wierzbinski, E.; Venkatramani, R.; Davis, K. L.; Bezer, S.; Kong, J.; Xing, Y.; Borguet, E.; Achim, C.; Beratan, D. N.; Waldeck, D. H., *ACS Nano*, **2013**, 7, 5391-5401.

26. Nitzan, A., *Isr. J. Chem.*, **2002**, 42, 163-166.

27. Egholm, M.; Buchardt, O.; Nielsen, P. E.; Berg, R. H., *J. Am. Chem. Soc.*, **1992**, 114, 1895-1897.

28. Ratilainen, T.; Holmén, A.; Tuite, E.; Haaima, G.; Christensen, L.; Nielsen, P. E.; Nordén, B., *Biochemistry*, **1998**, 37, 12331-12342.

29. Birks, J. B., *Photophysics of Aromatic Molecules*; Wiley: London, 1970.

30. Beall, E.; Yin, X.; Waldeck, D. H.; Wierzbinski, E., *Nanoscale*, **2015**, 7, 14965-14973.

31. Xu, B.; Tao, N. J., *Science*, **2003**, 301, 1221-1223.

32. van Wees, B. J.; van Houten, H.; Beenakker, C. W.; Williamson, J. G.; Kouwenhoven, L. P.; van der Marel, D.; Foxon, C. T., *Phys. Rev. Lett.*, **1988**, 60, 848-850.

33. Halbritter, A.; Makk, P.; Mackowiak, S.; Csonka, S.; Wawrzyniak, M.; Martinek, J., *Phys. Rev. Lett.*, **2010**, 105, 266805.

34. Makk, P.; Tomaszewski, D.; Martinek, J.; Balogh, Z.; Csonka, S.; Wawrzyniak, M.; Frei, M.; Venkataraman, L.; Halbritter, A., *ACS Nano*, **2012**, 6, 3411-3423.

35. Aradhya, S. V.; Frei, M.; Halbritter, A.; Venkataraman, L., *ACS Nano*, **2013**, 7, 3706-3712.

36. Wang, K.; Hamill, J. M.; Zhou, J.; Xu, B., *J. Am. Chem. Soc.*, **2014**, 136, 17406-17409.

37. Haiss, W.; Martín, S.; Leary, E.; Zalinge, H. v.; Higgins, S. J.; Bouffier, L.; Nichols, R. J., *J. Phys. Chem. C*, **2009**, 113, 5823-5833.

38. Li, C.; Pobelov, I.; Wandlowski, T.; Bagrets, A.; Arnold, A.; Evers, F., *J. Am. Chem. Soc.*, **2008**, 130, 318-326.

39. Xu, B. Q.; Zhang, P. M.; Li, X. L.; Tao, N. J., *Nano Lett.*, **2004**, 4, 1105-1108.

40. Hihath, J.; Xu, B.; Zhang, P.; Tao, N., *Proc. Natl. Acad. Sci. U.S.A.*, **2005**, 102, 16979-16983.

41. Nogues, C.; Cohen, S. R.; Daube, S.; Apter, N.; Naaman, R., *J. Phys. Chem. B*, **2006**, 110, 8910-8913.

42. Wang, K.; Hamill, J. M.; Wang, B.; Guo, C. L.; Jiang, S. B.; Huang, Z.; Xu, B. Q., *Chem. Sci.*, **2014**, 5, 3425-3431.

43. Xiang, L.; Palma, J. L.; Bruot, C.; Mujica, V.; Ratner, M. A.; Tao, N., *Nat. Chem.*, **2015**, 7, 221-226.

44. Bruot, C.; Xiang, L.; Palma, J. L.; Tao, N., *ACS Nano*, **2015**, 9, 88-94.

45. Di Felice, R.; Calzolari, A.; Molinari, E.; Garbesi, A., *Phys. Rev. B*, **2001**, 65, 045104.

46. Nishikawa, A.; Tobita, J.; Kato, Y.; Fujii, S.; Suzuki, M.; Fujihira, M., *Nanotechnology* **2007**, 18, 424005.

47. Nielsen, P. E., Ed.; Peptide Nucleic Acids: Protocols and Applications; Horizon Bioscience: Wymondham, U.K., **2004**.

48. Hegner, M.; Wagner, P.; Semenza, G., *Surf. Sci.*, **1993**, 291, 39-46.

## 3.0 Delocalization-Assisted Transport through Nucleic Acids in Molecular Junctions

This work was published as Clever, C., Valdiviezo, J., Beall, E., Pearse, A., Bae, Y., Zhang, P., Achim, C., Beratan, D. N., Waldeck, D. H. *Biochemistry* **2021**, *60*, 1368-1378. The author of the dissertation performed the conductance measurements and the subsequent analyses, and wrote the experimental portion of the manuscript. The supporting information for this chapter can be found in Appendix B.

The flow of charge through molecules is central to the function of supramolecular machines, and charge transport in nucleic acids is implicated in molecular signaling and DNA repair. We examine the transport of electrons through nucleic acids to understand the interplay of resonant and nonresonant charge carrier transport mechanisms. This study reports STM break junction measurements of peptide nucleic acids (PNAs) with a G-block structure and contrasts the findings with previous results for DNA duplexes. The conductance of G-block PNA duplexes is much higher than that of the corresponding DNA duplexes of the same sequence; however, they do not display the strong even−odd dependence conductance oscillations found in G-block DNA. Theoretical analysis finds that the conductance oscillation magnitude in PNA is suppressed because of the increased level of electronic coupling interaction between G-blocks in PNA and the stronger PNA−electrode interaction compared to that in DNA duplexes. The strong interactions in the G-block PNA duplexes produce molecular conductances as high as 3% $G_0$, where $G_0$ is the quantum of conductance, for 5 nm duplexes.

## 3.1 Introduction

The transport of charge through nucleic acids[1-12] can proceed by tunneling, resonant, near-resonant, or incoherent pathways that are sensitive to the macromolecular structure and its environment.[13-16] Until recently, the transport of charge through nucleic acids was believed to proceed by coherent tunneling at shorter distances and incoherent (multistep) hopping at longer distances.[11,17-19] However, recent studies found that neither the coherent nor the incoherent pictures are adequate to describe the transport at short to intermediate distances.[20-22] For example, the single-molecule conductances measured for deoxyribonucleic acid (DNA) duplexes with alternating cytosine (C) and guanine (G) bases, namely -$(GC)_n$- with *n* ranging from 3 to 8, were compared to those for duplexes of the same length with the G and C bases separated into blocks, i.e., -$G_nC_n$-.[21] The conductance of the -$(GC)_n$- duplex decreases linearly with *n*, while the conductance of the -$G_nC_n$- (G-block) duplex oscillates with *n*. The linear decrease in the conductance of $(GC)_n$ is consistent with an incoherent charge transport mechanism. The G-block conductance oscillations suggest extended carrier delocalization (coherence) over adjacent G-blocks.[23]

The strong sequence dependent conductance found for DNA[7] charge transfer[24-28] indicate sequence-dependent delocalization characteristics. Indeed, the more rapid exponential decrease in electrical conductance in AT duplexes compared to that in GC duplexes is well documented.[29] Less well understood is the influence of cross-strand couplings on the strength and mechanism of nucleic acid charge transfer and transport.[30] For example, positioning the molecule−electrode linker groups and the G-blocks on the 3′ termini of the DNA duplexes causes an order of magnitude increase in the single-molecule conductance compared to that of duplexes with the electrode-molecule linkers and G-blocks on the 5′ termini. This conductance

enhancement of the 3′-anchored G-block duplexes was explained by the stronger cross-strand G-to-G coupling between G-blocks accessed in the middle of the 3′−3′ structure, compared to the corresponding cross-strand coupling in the 5′−5′ chains.[30] Because the G-blocks mediate charge flow,[24] the cross-strand block-to-block coupling is critical.31 Indeed, the G-to-G cross-strand coupling is estimated to be 2−3 times larger in the 3′-anchored duplexes than in the 5′-anchored species.[32] The smaller cross-strand coupling in the 5′-anchored duplexes was suggested to be responsible for the enhanced even-odd conductance oscillations that were observed experimentally.[30]

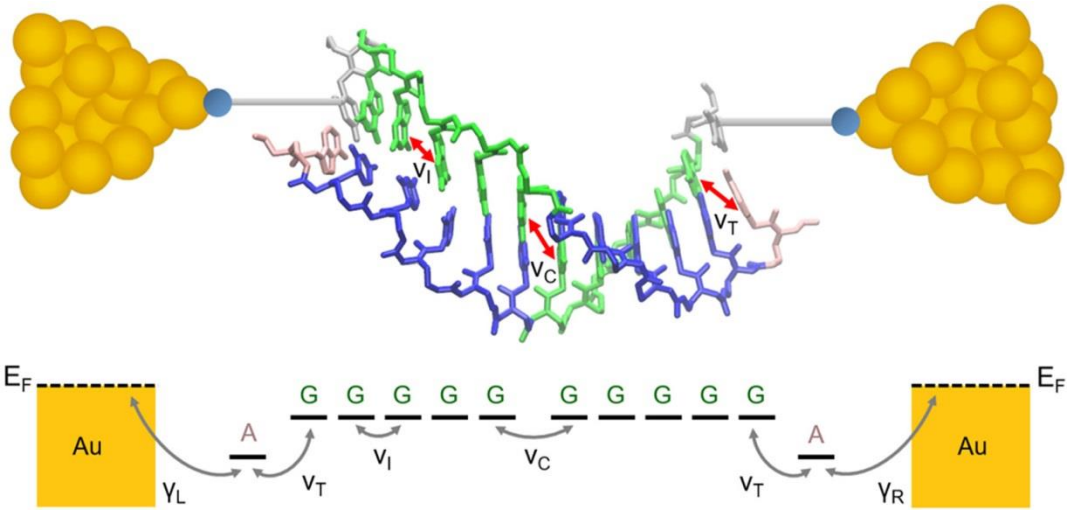


**Figure 3.1 Orientations of opposing termini (top) for the N-linked PNA for *n* = 5. The sequence shown is $TG_5C_5A$, and each color represents a different nucleotide. The duplexes are anchored to gold electrodes via amine modifications on the terminal thymine nucleobase. The arrows indicate the nucleobases considered for the GC-GC intrastrand ($V_I$), GC-GC cross-strand ($V_C$), and terminal AT-GC ($V_T$) electronic coupling calculations. One-dimensional model used in this work (bottom). $E_F$ is the Fermi level of the gold electrode. $\gamma_L$ and $\gamma_R$ are the molecule-lead electronic couplings. $V_I$, $V_C$, and $V_T$ are the nucleobase electronic couplings described above.**

Comparing the molecular conductance through aminoethylglycine peptide nucleic acid (PNA) and DNA duplexes with the same base sequences can help to reveal the structural origins

of the molecular conductances.[33-36] PNA and DNA duplexes that have the same number of bases and the same sequence, but a different backbone structure, can display conductances that differ by 10−20-fold.[36] These conductance differences were explained as arising from differences in the occurrence of strongly coupled nucleobases, as well as by differences of energy level broadenings. Indeed, energy level broadening can produce mechanisms that are neither purely coherent nor incoherent. The "flickering resonance" mechanism[37] relies on accessing conformations through molecular fluctuations that can support coherent transport during the persistence time of the quasi-degenerate energy configurations. The studies reported here describe the single-molecule conductance of G-block PNA duplexes for five different lengths ($n$ = 3−7) and compare the conductances to those measured in G-block DNA duplexes reported previously.[30] This study explores how changes in backbone chemistry influence the conductance values and the relative contributions of coherent and incoherent transport mechanisms.

The structure of N-linked PNA is shown in Figure 3.1. An amine-modified thymine nucleobase is positioned at the N-terminus of the self-complementary G-block PNA oligomer; Watson−Crick hybridization of the PNA oligomer leads to a PNA duplex that has a palindromic sequence with amine-modified thymines on both ends of the duplex. Electronic coupling occurs between the electrode and the amine-modified thymine at the N-terminus of one strand of the duplex; the modified thymine at the N-terminus of the complementary strand interacts with the STM break junction tip (N-to-N transport). The N-terminus of PNA is analogous to the 5′ terminus of DNA.[38] The conductance measured for the G-block PNA duplexes is as much as 20 times larger than that measured for the analogous G-block DNA duplexes, and the even−odd conductance oscillations are found to be less pronounced in PNA.

The enhanced conductance of PNA duplexes, found in earlier comparisons between DNA and PNA homoduplexes, was attributed to the greater backbone structural flexibility in PNA.[36] The study presented here shows that the conductance of G-block PNA is larger than in G-block DNA; however, the G-block duplexes of DNA and PNA appear to have similar structural flexibility (*vide infra*). Nevertheless, the theoretical analysis suggests that the structural changes associated with the different nucleic acid backbones affect the electronic couplings through the π-stack and the nucleic acid−electrode interactions, producing stronger electrode−molecule coupling for PNA than for DNA. That is, the electronic coupling interactions near the chain ends ($\gamma_L$, $\gamma_R$, and $V_T$, indicated in the lower panel of Figure 3.1) are much larger for PNA duplexes than for DNA duplexes. The measured conductance value trends for the three duplex types and the magnitude of the even−odd conductance oscillations are rationalized using an orbital model to describe the mediating states (*vide infra*).

## 3.2 Experimental and Computational Methods

### 3.2.1 Conductance Measurements

Single-molecule conductances were measured for PNA duplexes of different lengths tethered at the N-chain ends. A diffuse duplex monolayer was formed on a gold substrate by spontaneous adsorption from a Tris-EDTA buffer solution of a nucleic acid with amine linkers attached to the terminal thymine nucleobases. The electrical conductance of nucleic acid duplexes trapped in a junction between the STM tip and the gold substrate was measured using an AC-modulated scanning tunneling microscope break junction (STM-BJ) method.[39,40] This

experiment drives the STM tip to the surface of the gold substrate and then withdraws it, allowing molecular junctions to form between the substrate and tip. During each tip withdrawal, a triangular voltage waveform is applied between the STM tip and the substrate and a set of current−time profiles are collected. Figure 3.2 shows an example of a single time trajectory for an STM−PNA−substrate junction, in which the PNA is a sequence of 12 nucleobase pairs. In this experiment, the STM tip is retracted at a rate of 0.1 nm/ms as the bias voltage is modulated with a 2 ms period. The retraction rate was chosen to balance the stability and duration of the molecular junctions. The total length of the trajectory in Figure 3.2 is ≈4 nm. Note the sharp change in the current levels near the 640 ms time point. This change is indicative of two distinct junction geometries, and they are described extensively in previous reports.[29,36,40] Conductance measurements on duplex DNA were performed in mesitylene, and values were compared to earlier measurements in buffer solutions.[30] Good agreement among the measurements was found, suggesting no significant changes in the conformations of the nucleic acids. For this reason, and for reasons of experimental convenience, conductances were measured in a mesitylene solution. Fitting these current−time profiles using a circuit model allows molecular conductance, *G*, to be extracted from the data, and these values are used to build conductance histograms (see Appendix B).[41] Note that background conductance histograms were also measured in experiments without PNA molecules present. It has been reported that molecular junctions of mesitylene produce conductance values of approximately 0.03 and 0.1 $G/G_0$.[42,43] However, the length of these junctions is very short, ~0.2 nm, which corresponds to a single voltage modulation period in our measurement (see Figure 3.2), and it is rejected by our criterion that the molecular junction must persist for at least four voltage modulation periods at a consistent current level to indicate a nucleic acid molecular junction. Therefore, any mesitylene

conductances that are recorded would be significantly less prevalent than the nucleic acid junctions, as is shown by the control experiments (see Appendix B for more details).

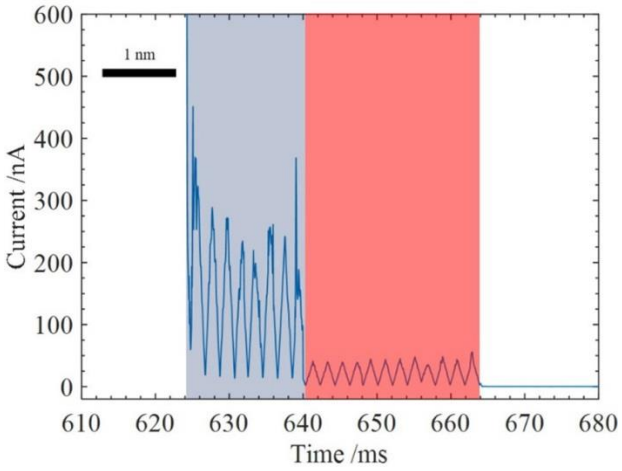


**Figure 3.2 Example current−time *I(t)* trajectory of a PNA 12-mer Gblock molecular junction. Each triangular period is 2 ms in duration; the STM tip retracts by 0.2 nm during each current response period, and the bar shown at the top left gives the length scale. The initial region (blue) corresponds to the high-conductance mode, while the later region (red) is the lower mode. Note that the junction persists for ~4 nm, which corresponds to the full length of the PNA molecule.**

### 3.2.2 Molecular Dynamics Simulations

Nucleic acid conformations were sampled using classical molecular dynamics (MD) simulations, and the structures provide a starting point for computing the energies of specific base orbitals and their electronic coupling interactions. Initial B-DNA structures were obtained using the Avogadro DNA builder tool,[44] and PNA duplexes were generated with the Schrödinger Maestro molecular modeling software,[45] starting from a right-handed PNA crystal structure with a heterogeneous sequence (Protein Data Bank entry 3MBS).[46] The CHARMM36 force field DNA parameters,[47] and the recently developed PNA parameters,[48] were used (the new PNA force field produces structural ensembles that are consistent with those found using

other force fields in earlier studies).[36] The structures were solvated in a TIP3P water box[49] that extended at least 15.0 Å from each atom. A distance constraint was added between the terminal base pairs to prevent fraying.[50] NAMD version 2.11[51] was used to run the MD simulations. After energy minimization and equilibration, the solvated structures were subjected to 100 ns of MD simulation at 300 K and 1 atm pressure. Snapshots for each system were saved every 33 ps (3000 coordinate snapshots in all). A detailed description of the procedure is found in Appendix B.

### 3.2.3 Electronic Coupling and Site Energy Analysis

For each MD snapshot, the nucleobase HOMO energies and nearest-neighbor cross-strand ($V_C$), intrastrand ($V_I$), and terminal AT-GC ($V_T$) couplings (Figure 3.1) were computed from the Fock matrix using the block diagonalization method;[52] the Fock matrix was obtained at the INDO/S level[53] from the CNDO program.[54] The INDO/S method gives a good description of charge transfer parameters in organic $\pi$-stacks at a reasonable computational cost.[55] Electronic couplings were computed in the two-state approximation. Only the nucleobases were included in the computation of orbital energies and electronic couplings, denoted as *in vacuo* (solvent and backbone atoms were removed, and dangling bonds were capped with hydrogens). The explicit treatment of backbone and solvent as classical point charges (QM/MM scheme) has been reported to have a small influence on the HOMO energy mean values,[56] and in sequences with longer bridges, as in this study, the rate constants for hole transfer calculated using a QM/MM formalism and *in vacuo* approaches are similar.[57] It has also been shown that electronic couplings calculated using the QM/MM formalism are similar to the *in vacuo* results,[56,57] so we used the *in vacuo* results in the analysis described here. The

methods used here were shown to provide reliable estimates of the electronic couplings in DNA.[32,33]

A cross-strand coupling via the superexchange guanine-cytosine-guanine pathway was also calculated for snapshots taken every 5 ns, using only the four nucleobases in the cross-strand region. A density functional theory approach was selected to describe the hydrogen bonding interactions between nucleobases,[58] which are relevant for the superexchange pathway. The Kohn−Sham matrix obtained with the M11 functional[59] and the ma-def2-TZVPP basis set[60] as implemented in Gaussian 16[61] was used to compute the associated electronic couplings.

## 3.3 Results and Discussion

### 3.3.1 PNA Duplex Conductance

Conductance histograms for the N-to-N linked PNA duplexes with the $TG_nC_nA$ sequence (n = 3−7) are shown in Figure 3.3, and the most probable conductance for each mode is reported in Table 3.1. All conductance histograms have two peaks, similar to the histograms reported for other PNA duplexes.[36] The multiple peaks in the molecular conductance histograms were assigned to distinct "conductance modes" that can arise from different binding modes of the linkers and the gold atoms of the surface, specifically the number of gold atoms bonded to the linker, or from different conformations of the molecular junctions.[62,63] The contribution of higher-conductance modes increases with duplex length. This correlation is consistent with the experimental observation that shorter duplexes, which have lower thermal stability, have shorter average residence times in the junction.[29] Thus, the increased statistical weighting of the

high-conductance mode likely indicates an increased fraction of more stable π-stacked duplexes in the junction, arising from the presence of stronger π-overlap between the GC pairs that make the structure more rigid. A more detailed discussion of the different "conductance modes", as well as transitions between them (see Figure 3.2) and how they are distinguished by the length of time a molecule remains in the junction, is provided in references 29 and 40.

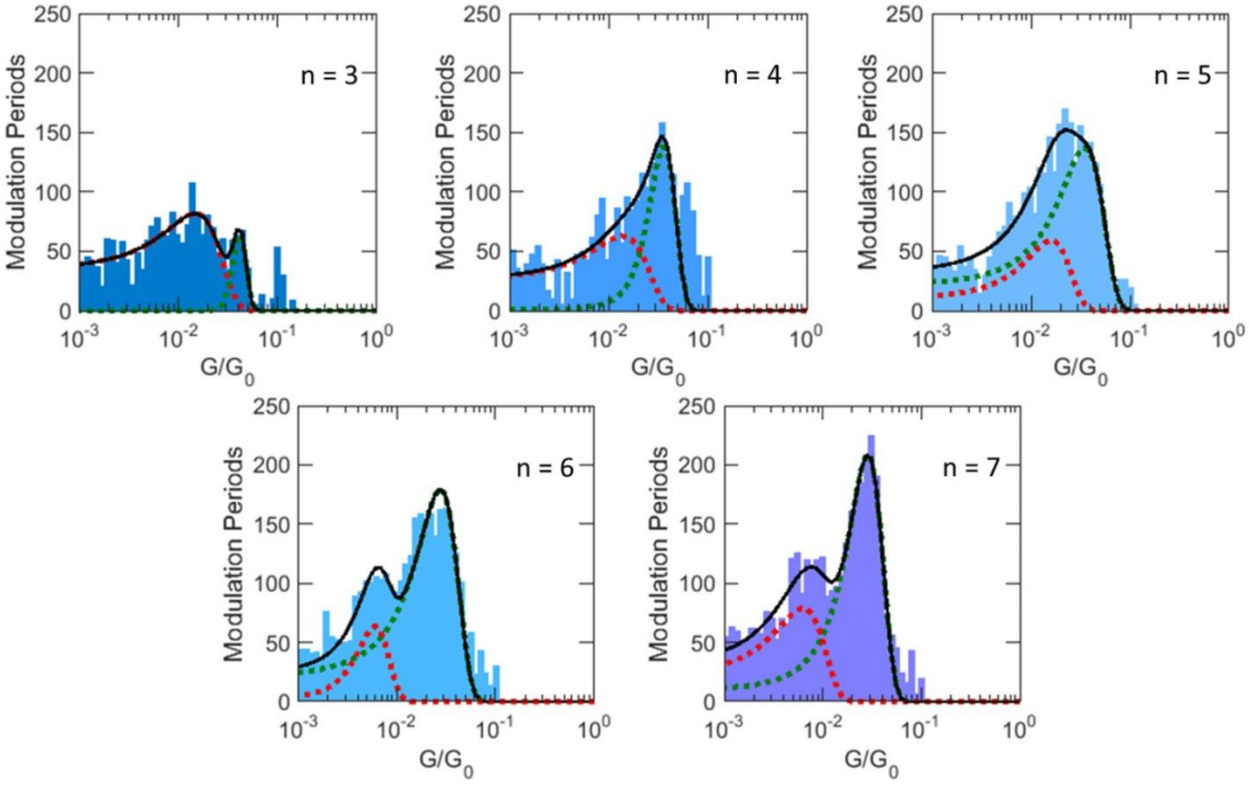


**Figure 3.3 Conductance histograms for the N-to-N linked PNA for n = 3−7. The black curve is a sum of two Gaussian functions. The dotted red and green curves are the individual Gaussians for the low and high-conductance modes, respectively. The y-axis shows the number of modulation periods measured.**

Although both modes are shown in Figure 3.3, the analysis and discussion focus on the highest-conductance mode to draw comparisons with the earlier G-block DNA studies that focused on the highest-conductance modes. In some instances, most notably for n = 4, a shoulder or second peak appears at twice the conductance value of the most probable peak for a given conductance mode. This feature was analyzed previously, as well, and is attributed to two

or more molecules forming in a molecular junction.[29,40] In contrast to earlier STM break junction studies of PNA in which the conductance was well below $10^{-3}$ $G_0$, the G-block duplexes studied here have conductances that are a few percent of $G_0$. Measurements at these higher conductances created the need to distinguish molecular signals from background signals arising from (sub)oxide formation on the substrate that appear at ~0.1 $G_0$. The measurement protocols and control experiments used to distinguish the two signals are described in the Supporting Information. The conductance shoulders of the histograms in Figure 3 and the (sub)oxide signal were excluded from the Gaussian fitting.

**Table 3.1 Average Conductance Values of the Highest Observable Mode, G, and the Standard Deviation, $\sigma_G$, from the Gaussian Fits for the N-Linker PNA Duplexes for Lengths n = 3−7.**

| *n* | $G/G_0$ ($x10^{-2}$) | $\sigma_G/G_0$ ($x10^{-2}$) |
|---|---|---|
| 3 | 4.2 | 0.6 |
| 4 | 3.6 | 1.0 |
| 5 | 3.5 | 1.8 |
| 6 | 2.8 | 1.4 |
| 7 | 2.9 | 1.2 |

The average single-molecule conductance for the high-conductance mode shows a modest decrease as the duplex length increases (see Table 3.1). The influence of the background signal on the measurements is negligible for the n = 4−7 duplexes but may contribute to the n = 3 measurement, because fewer molecular junctions were sampled in this case (given the decreased residence time of the duplex in the junction). To account for these signal-to-noise constraints, more extensive background measurements were performed, and the peak at ~0.1 $G_0$ was excluded from the analysis (see Appendix B). Note that Table B.1 provides a listing of the conductances and standard deviations for the lower-conductance mode.

The conductances of the -($G_nC_n$)- PNA duplexes show a nearly monotonic, albeit weak, decrease as n increases. Figure 3.4 plots these PNA data and the conductance data for 3′ DNA

G-blocks and 5′ DNA G-blocks. We measured molecular conductances for n = 3−5 G-blocks of 3′ and 5′ DNA duplexes (see Appendix B) and found good agreement with the values reported earlier by Tao and coworkers.[21,30] Both of these data sets, the sets reported here and those reported by Tao, are plotted in Figure 3.4. These data highlight the significant difference in the average conductance for the three duplex types, as well as the decreasing prominence of the conductance variations with even and odd G-block lengths in the three duplexes (see Appendix B for plots showing the lower-conductance modes).

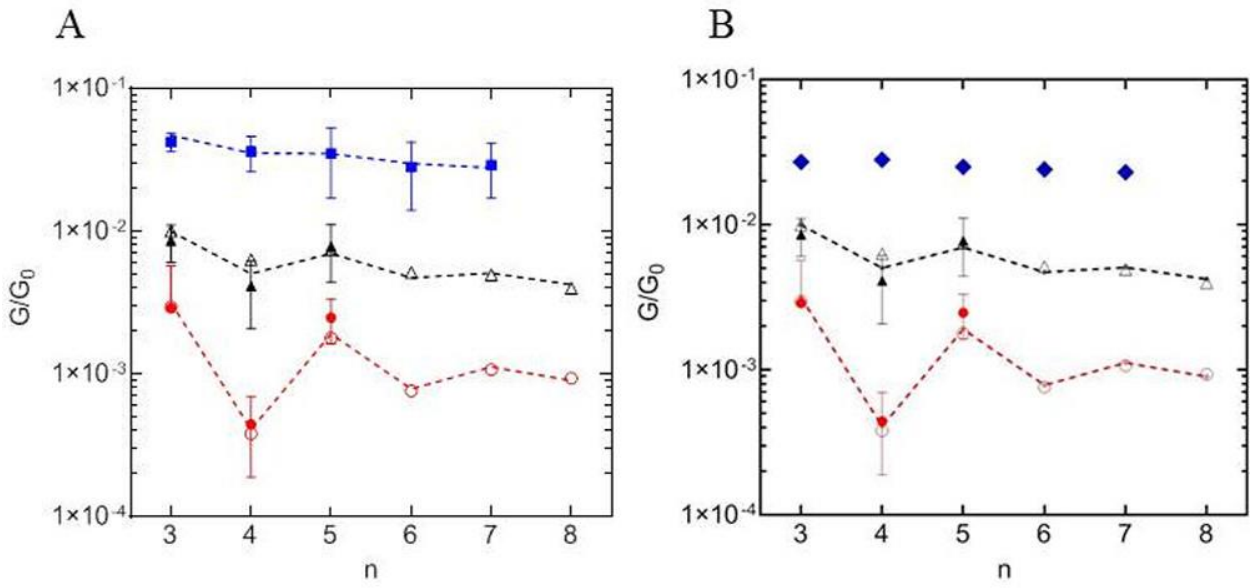


**Figure 3.4 (A) Average conductance for the N-linker PNA (blue squares) with data for 3′-linker DNA (black triangles) and 5′-linker DNA (red circles). The empty symbols are from a previous study[30] and the filled symbols are from this study. Error bars are shown for the duplexes studied here representing a single standard deviation of the fitted Gaussian function for the highest observable mode. The negative component of the error for the 5′-linker DNA n = 3 data point has been excluded for the sake of clarity. The lines in the plot connect the best fit conductances found using the Büttiker double barrier model (see Appendix B). (B) Alternate analysis in which the PNA conductance values were assigned to the mean conductance value of the histogram, to show the increased PNA conduction in a model-independent manner.**

### 3.3.2 Theoretical Analysis of DNA and PNA Structures and Electronic Properties

Molecular dynamics simulations of PNA and DNA duplexes -($G_5C_5$)- were run for 100 ns. This time range allows sampling of the internucleobase fluctuations and a subset of duplex conformational changes.[33] Analysis of these structural data indicates that the root-mean-square deviations (RMSDs) for the structural fluctuations of PNA duplexes are comparable to those of the DNA duplexes. The duplex RMSD value from its average structure calculated with VMD[64] is 1.3 ± 0.3 Å for N-linked PNA, 1.4 ± 0.4 Å for 3′-linked DNA, and 1.5 ± 0.4 Å for 5′-linked DNA. The small difference in RMSD values suggests that the PNA duplexes are slightly more rigid than the corresponding DNA structures (see Figure B.5 and Figure B.6). This result is the opposite of results that were found earlier for PNA and DNA duplexes with a mixed nucleobase sequence. (For mixed sequences, the PNA duplexes were found to be more flexible than the DNA duplexes.[33]) This finding indicates that the relative structural flexibility of the nucleic acids is sequence-dependent. The larger overlap between nucleobases in the PNA G-blocks leads to stronger $\pi-\pi$ interactions and decreased flexibility as compared to those of mixed sequence PNA duplexes.[65]

MD snapshots were used to calculate HOMO energy fluctuations for each base pair in the duplexes (at the INDO/S level). The HOMO energy fluctuations and standard deviations of each base pair are listed in Table 3.2 for the n = 5 length, which is illustrated in Figure 3.1, for the case of PNA. The similar HOMO energies and their standard deviations suggest that the energy fluctuations are similar for PNA and DNA duplexes. These HOMO energies, calculated *in vacuo*, are 1.5−2 eV below the Au work function. However, the influence of a metal electrode on the electronic state energies of adsorbed species can be substantial (∼1 eV[66]), and we expect

the energy offset between the Fermi level and the effective HOMO orbital energies to be significantly less than 1.5−2 eV.

**Table 3.2 HOMO Energies (eV) and Their Standard Deviations for the GC Base Pairs Examined in the Cross-Strand, Intrastrand, and Terminal Electronic Coupling Calculations. These values are calculated for n = 5 chains.**

| | 5' DNA | | 3' DNA | | PNA N-end | |
|---|---|---|---|---|---|---|
| | $E_{HOMO}$ | $\sigma$ | $E_{HOMO}$ | $\sigma$ | $E_{HOMO}$ | $\sigma$ |
| **cross** | -6.51 | 0.22 | -6.55 | 0.21 | -6.97 | 0.19 |
| **intra** | -6.41 | 0.22 | -6.37 | 0.21 | -6.47 | 0.19 |
| **term** | -6.68 | 0.21 | -6.71 | 0.22 | -6.56 | 0.18 |

We calculated the nearest-neighbor root-mean-square electronic couplings ($V_{RMS}$) between base pairs (INDO/S, block diagonalization method, capped bases),[32] where $V_{RMS} = \sqrt{\langle V^2 \rangle} = (1/n)\sqrt{\sum_{i=1}^{n} V_i^2}$, where $V_{RMS}^2 = \langle V \rangle^2 + \sigma^2$, $\sigma$ is the standard deviation of *V*, and *n* is the number of MD snapshots used for averaging. Table 3.3 shows the calculated $V_{RMS}$ values. Table 3.3 reports the calculated electronic couplings of the terminal AT base pairs with their nearest GC pair ($V_T$) for each of the three duplex types. These calculations indicate a nearly 3-fold increase in $V_T$ for N-terminal PNA compared to the corresponding couplings in the DNA duplexes. Table 3.3 also shows that the N-linker PNA duplex intrastrand couplings ($V_I$) are larger than the values found for the DNA counterpart. The increases in the couplings, $V_I$ and $V_T$, for PNA versus DNA are consistent with the larger molecular conductances that are observed experimentally. The cross-strand coupling ($V_C$) also affects the conductance, and earlier work[30] showed that it affects the even−odd oscillations which are discussed next. A description of how these computed electronic coupling values are linked to the conductance measurements follows this subsection.

**Table 3.3 $V_{RMS}$ Values of GC-GC Cross-Strand ($V_C$), GC-GC Intrastrand ($V_I$), and Terminal AT-GC Coupling ($V_T$) in Electronvolts. The cross-strand GC-GC couplings for the superexchange pathway ($V_C^{SE}$) are also shown.**

| | 5' DNA | 3' DNA | PNA N-end |
|---|---|---|---|
| $\mathbf{V_T}$ | 0.011 | 0.017 | 0.047 |
| $\mathbf{V_I}$ | 0.087 | 0.071 | 0.120 |
| $\mathbf{V_C}$ | 0.006 | 0.012 | 0.002 |
| $\mathbf{V_C^{SE}}$ | 0.001 | 0.005 | 0.017 |

The direct cross-strand couplings, $V_C$, of the N-linked PNA and 5′-linked DNA are both small compared to the other couplings, presumably because of the small overlaps between the G bases on the two strands (Figure B.7). Thus, we examined how these values compared with coupling obtained from a superexchange pathway involving three nucleobases, $V_C^{SE}$ (Table 3.3). MD simulations show that the geometrical parameters of PNA produce larger G-C π-overlaps in the cross-strand region and, as a consequence, stronger π-couplings compared to the case in DNA (see Figure B.8). The strong π-interaction between the stacked GC nucleobases in PNA provides a superexchange pathway for charge transfer. The cross-strand coupling, $V_C^{SE}$, for the guanine-cytosine-guanine superexchange pathway was calculated for selected snapshots taken every 5 ns with density functional theory to describe hydrogen bonding interactions (M11/ma-def2-TZVPP, block diagonalization, capped bases).[58,67] $V_C^{SE} = \frac{V_{G5\text{-}C6} V_{G6\text{-}C6}}{\Delta E}$, where the subscripts indicate the nucleobase and the position in the n = 5 duplex (see Figure B.10) and ΔE is the difference in energy between guanine and cytosine localized states, which is close to 0.7 eV.[68,69] $V_C^{SE}$ values, which are the RMS couplings, are included in Table 3.3. $V_C^{SE}$ is larger than the RMS $V_C$ values for only PNA, suggesting that the superexchange contribution to the cross-strand coupling is more relevant to the transport mechanism in PNA than in DNA, and we will address the implications for charge transport below.

In addition to differences in coupling pathways for PNA and DNA, the MD simulations reveal structural differences among the duplexes that can affect the electrode−molecule electronic couplings ($\gamma_L$ and $\gamma_R$). Recall that $V_T$ and $\gamma_L$ and $\gamma_R$ determine the electronic coupling interactions near the chain ends. The orientation of the terminal AT base pair, which contains the amine groups that bind to the Au electrodes, with respect to the first GC base pair of the G-block (see Figure 3.1) appears to be different in the PNA junctions and in the DNA duplexes. In particular, the DNA terminal base pairs exhibit larger structural fluctuations than in PNA, which leads to "fraying" of the duplex in the absence of the distance constraint described above. In addition, the increased rigidity of the PNA nucleobases, which correlates with enhanced π−π stacking interactions, likely contributes to establishing strong contacts with the leads and increasing the conductance.

### 3.3.3 PNA versus DNA Conductance

The average experimentally measured single-molecule length-dependent conductance for the high-conductance mode of each duplex is shown in Figure 3.4. For the N-to-N linked PNA, the average conductance of the highest-conductance mode is $\sim 3 \times 10^{-2}$ $G/G_0$ (where $G_0$ is the quantum of conductance). The average conductances for the PNA duplexes are an order of magnitude larger (or more) than for DNA duplexes of the same length. Figure 3.4b shows the mean conductance value obtained from the PNA conductance histograms, which are 3−5 times larger than the literature conductance values reported for 3′ DNA. In addition to the PNA conductances, the conductances for the first few (n = 3, 4, and 5) 3′- and 5′-linked G-block DNA duplexes were measured in this study and are plotted as filled symbols in Figure 3.4. The measurements performed here are in good agreement with those reported by Tao and co-workers

(empty symbols) and also display the even−odd oscillation.[30] Note that the increased conductance in PNA compared to DNA is consistent with earlier findings for mixed PNA sequences,[29,36] although the details of the mechanism for the large PNA conductance may be different.

The G-block PNA molecules show a significantly higher conductance (2−4% of $G_0$) than is typically found for molecules of a comparable length, ~3−5 nm.[70] For example, molecules that display conductances on the order of a few percent of $G_0$ are typically the size of a single aromatic ring, e.g., benzenedithiol and benzenediamine. Two key factors influencing the molecular conductance in a junction are the electrode−molecule linker group and the molecule's electronic structure. The linker group can have order(s) of magnitude effects on the measured conductance.[70,71] The amine linkers for the PNA and DNA duplexes used in this study couple the aromatic stack of the duplex more strongly to the electrode than do the backbone-based thiol linkers used in earlier studies.[72] The electronic structure of the mediating molecule, e.g., saturated versus unsaturated, is known to have a strong influence on the molecular conductance, as well.[68] However, molecules with highly conjugated electronic structures, such as oligo(phenylene-vinylenes) and oligophenylethynylenes, show conductances in the range of $\leq 10^{-3}$ $G_0$ if they are a few nanometers in length.[70,73] The length dependence of the molecular conductance through a homologous series of molecules is often characterized using an exponential decay as a function of length $L$, i.e., $\exp(-\beta L)$.[74] Conjugated molecules show a much weaker decay with distance (smaller $\beta$ value) than do saturated systems. Both the shallow dependence of the PNA conductances on length and the high conductance values are consistent with transport mediated by extended $\pi$-systems.

The observation that the molecular conductances of G-block PNA duplexes are 10−20 times higher than those of the corresponding 5′ DNA duplexes with the $\pi$-stacked linkers is consistent with previous observations. Bruot *et al*.[72] compared the molecular conductance through 5′A$(CG)_n$T3′ ($n$ = 2−12) DNA duplexes consisting of thiol linker groups connecting to the nucleic acid backbone with duplexes of the identical nucleobase sequence that have amine linkers bonded directly to the base stack. They found that the conductance was 10−20 times higher for the $\pi$-stack linker than for the backbone linker for otherwise identical DNA duplexes. In earlier studies, we compared the molecular conductance of PNA duplexes to that of DNA duplexes with thiol linker groups on the nucleic acid backbone. In those cases, the PNA displayed a molecular conductance that was ∼20 times higher than that of the DNA.[29,36] The high conductances measured for the PNA duplexes in this study are consistent with these earlier findings. The combined effects of the amine/thymine-based linker group and the high electronic coupling through the G-block stack are responsible for the high conductances reported here (*vide infra*).

### 3.3.4 Molecular Orbital Interpretation of Conductance Oscillations

The N-to-N linked PNA duplexes show a 1-2 order of magnitude increase in the molecular conductance compared to the values for the corresponding 5′-linked DNAs. This increase in conductance is consistent with the findings for mixed sequence DNA and PNA duplexes reported previously.[29,36] Conductance oscillations observed previously in the 5′-linked and 3′-linked DNA systems are barely evident for the PNA duplexes. The decreased amplitude of the even-odd oscillations with G-block length is explained by the larger cross-strand coupling

and electrode-molecule couplings in PNA. We first discuss the cross-strand coupling effect and then examine the influence of electrode-molecule coupling on the conductance oscillations.

In earlier studies, conductance oscillations as a function of length in G-block DNA duplexes (see Figure 3.4) were explained by an electronic energy effect that arises in finite length periodic structures.[30,75,76] Odd length G-blocks possess a "midband" localized orbital with an energy near the Fermi level of the gold electrode, approximately equal to the energy of a G monomer.[30] This length-independent near degeneracy was proposed to strengthen coherent charge transport for odd length chains by providing a flickering resonance coupling pathway across the entire duplex.[30] In contrast, the orbital energies for even length G-blocks are offset from the "midband" position (Figure 3.5) and are unlikely to form flickering resonance coupling pathways across the structures. This picture accounts for the oscillations of conductance with length, as shown in Figure 3.4.

Figure 3.4 shows that the amplitude of the conductance oscillations decreases through the three duplex types as the overall conductance of the duplex increases. For example, the oscillations in conductance are substantially less pronounced when the molecular linkers are positioned at the 3′ termini of DNA, as compared to the 5′ termini, and the corresponding molecular conductance of the 3′ species is observed to be larger. The decrease in the amplitude of the oscillations of conductance, and the overall increase in conductance in DNA, was attributed to geometric differences of the base pairs at the cross-stand position in the two cases (Figure B.7 and Figure B.8), which causes a change in the cross-strand coupling.[30] Intriguingly, a large cross-strand GC-GC coupling at the molecule's center reduces the likelihood of forming a fully delocalized (resonant) state across the G-blocks and the electrodes (*vide infra*).[77]

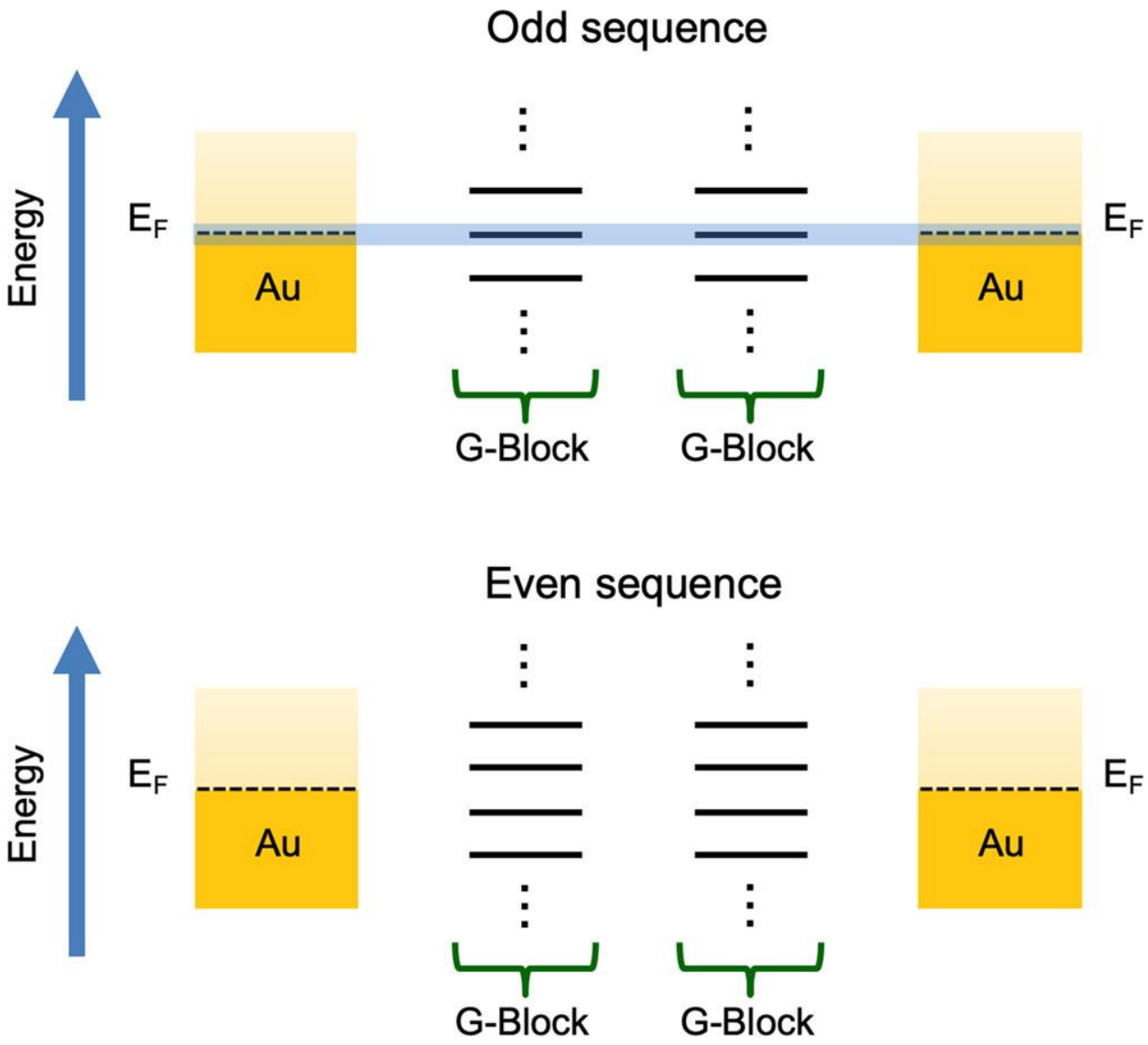


**Figure 3.5 Molecular orbital energy picture of nucleic acid duplexes with a weak cross-strand coupling. Flickering resonance energy level alignment for odd length sequences (top). Each G-block possesses a midband orbital in resonance with the Fermi level of the electrodes. Energy level alignment for even sequences (bottom). A midband state in resonance with the Fermi level of the electrodes is absent.**

As a rule of thumb, the number of G bases over which the hole can delocalize at room temperature can reach five.[30,78] When the cross-strand coupling is weak, as in 5′ DNA, the dominant position for the delocalized hole is across the *n* guanines that form each of the separate G-blocks, forming two domains. Thermal fluctuations can bring these two domains into

resonance, i.e., flickering resonance, and form a fully delocalized state across the entire duplex[37] (Figure 3.6). Because the odd length G-blocks have resonant states near the Fermi level, and the even length G-blocks do not, a strong modulation of the conductance with the G-block length is predicted to manifest. As the cross-strand coupling increases, delocalization can occur among G nucleobases of the two blocks, and this leads to a lower statistical weight for configurations that have the hole delocalized over each of the G-blocks. The growth in the number of configurations with delocalized domains leads to a higher overall conductance. The decreased statistical importance of the configuration with the extended G-block delocalization manifests as a decrease in the amplitude of the even-odd length conductance oscillations. Overall, the conductance is limited by the squared coupling between these domains and by the molecule-lead interaction strengths. The observation that the conductance increases from 5′ DNA to 3′ DNA, and increases further as the backbone is switched to PNA, is consistent with growth in the number and size of the cross-strand delocalization domains and their importance for charge transport (switching from 5′ to 3′ increases the cross-strand coupling 3−4-fold, and switching to PNA increases the coupling by almost another 2-fold).

Figure 3.6 illustrates this mechanistic explanation for the change in conductance and in the even−odd effect for 5′ DNA and PNA. The bottom panel illustrates the mechanistic picture described in our prior analysis of the even and odd effects on the 5′-linked DNA conductance.[30] In this structure, the weaker cross-strand coupling in the 5′ structure (compared to that in the 3′ structure) leads to delocalization of orbitals on each of the two separated G blocks. Formation of a transient structure with extended delocalization only requires bringing these two blocks into resonance with each other and with the electrodes. This was illustrated in Figure 3.5 for the case of odd length (n = 3) and even length (n = 4) chains to underscore how the energies of the

G-block states are offset from the Fermi level of the electrodes. The dependence of the energy mismatch on whether *n* is even or n is odd, and the promotion of delocalization across each G-block by the weak cross-strand coupling, leads to a strong even-odd conductance effect.

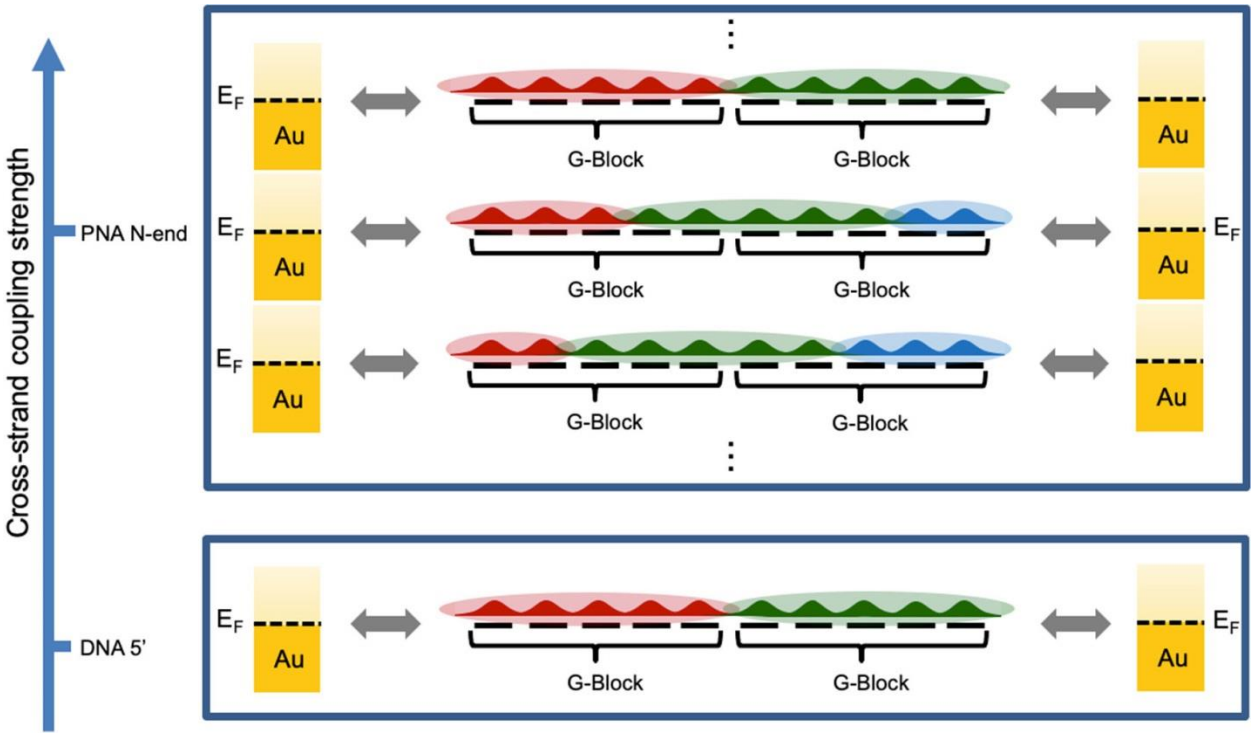


**Figure 3.6. Model describing the delocalized islands across two G-blocks, each with n = 5. The maximum number of G residues over which the hole can delocalize can reach five (each color represents a delocalized block of orbitals).[30,78] Regime with a strong cross-strand coupling (top). The strong cross-strand coupling allows the five-base pair delocalization to occur anywhere across the entire ten-base sequence of the G-blocks (e.g., the green block can be delocalized across the two strands). Therefore, the carrier position in PNA is less constrained than in DNA. For the sake of illustration, three possible configurations that support delocalization are shown (many others are possible). Regime in which the coherent channel with the hole delocalized over each G-block contributes significantly to the conductance (bottom). This coherent channel is absent in even length sequences (see Figure 3.5).[30,75] The weak cross-strand coupling pins the carrier delocalization on one of the G-blocks. The odd length G-block sequences are near resonant with the Fermi level of the leads and create a delocalized state for coherent transport.**

The top panel in Figure 3.6 explains the mechanistic picture for the case in which the cross-strand coupling is large (comparable to intrastrand GC-GC couplings). In this case, many possible delocalized islands of approximately five or fewer Gs may form in the structure. Indeed, in this regime, the likelihood of forming a delocalized state spread over the entire length of each G-block is diminished because of the increase in the overall number of other possible configurations that support delocalization, as illustrated by the two additional configurations shown in the top panel of Figure 3.6. Although this effect creates delocalized islands with more than one energy mismatch (so that multiple level matchings are required to delocalize over the entire molecule), many more configurations that display these delocalized islands manifest and provide many more flickering resonance conductance pathways in PNA, which leads to an overall increase in its conductance.

Our theoretical analysis (Table 3.3 and discussion) suggests that the electrode−molecule couplings for the PNA duplexes are stronger than in the 3′-linked and 5′-linked DNA. This feature is not included in the diagrams of Figure 3.6 for the sake of simplicity. A stronger electrode−molecule coupling is expected to produce a stronger mixing between the gold and the G-blocks of PNA compared to DNA. The stronger molecule−lead coupling is expected to further enhance the conductance of PNA. This prediction is consistent with the observed higher conductance in PNA and softer even−odd effect compared to that in DNA. We note that strong molecule−lead interactions can perturb the “band structure” for each G-block and will shift the energy of the midband state that appears for odd length chains. The effect of the strong molecule−lead coupling can break the degeneracy between delocalized hole states in each G-block and dampen the conductance oscillations in PNA compared to the case in 5′ DNA. This

scenario was explored in detail by Segal et al., who showed that strong molecule−lead hybridization can indeed cause the even−odd effects to vanish.[75]

## 3.4 Conclusions

The transport of charge through nucleic acids can access coherent, incoherent, and flickering resonance mechanisms. The experimental and theoretical studies reported here find that structural differences in the duplex backbone with the same base sequences can produce order of magnitude changes in molecular conductances and can strongly influence how coherence manifests for single-molecule PNA and DNA junctions. For PNA duplexes, a conductance value of 0.03 $G_0$ was found with 14 base pairs (∼50 Å). PNA also has a high-mode conductance that is ≤30 times larger than that of DNA, and the conductance decreases monotonically with duplex length. The corresponding DNA structures show a striking conductance oscillation. The nearly monotonic and weak (<2-fold for distances from ∼2 to 5 nm) change in conductance with duplex length that is found in PNA indicates an extremely low molecular resistance, in strong contrast with that for the 5′-linked DNA duplexes. The overall conductance in 5′ DNA changes by only 2-fold between the $n$ = 3 and $n$ = 8 G-block pairs. The even−odd conductance oscillations in 5′ DNA with G-block length can be up to 4-fold, and the average conductance in 5′ DNA is 1−2 orders of magnitude lower than in PNA. Despite these dramatic differences in the experimental conductances and their length dependences, the flickering resonance transport mechanism provides a consistent explanation for the observed behavior.

Theoretical analysis shows that the PNA and DNA G-block structures studied here have similar structural flexibility, base energy fluctuations, and base−base electronic interactions. The main differences between the PNA and DNA duplexes appear to be rooted in (1) differences in the molecule−electrode interaction strength and (2) differences in the base−base interactions in the cross-strand region, which arise from differences in geometry between duplex PNA and DNA. The stronger cross-strand and molecule−lead couplings in PNA lead to higher conductance than in DNA. As such, the characteristics of cross-strand, intrastrand, and molecule−lead couplings collectively influence the contribution of competing coupling pathways to the conductance. The mechanistic origin of the even−odd conductance effect found in the DNA is consistent with that reported previously,[30] which showed that cross-strand interactions in the center of the duplex tip the balance among mechanisms. In contrast to earlier studies, the findings reported here indicate that the conductance mechanism is also influenced by the strength of the nucleic acid−electrode interactions. Growing the electrode molecule or the block-to-block couplings is expected to reduce the statistical importance of delocalized states spread across just one G-block, leads to a decrease in the even−odd length conductance oscillations with length, and produces an overall increase in the molecular conductance. Future work should explore the effects of the molecule−lead coupling strength on conductance; for example, one can vary the aliphatic chain length of the amine linkers or modify the electrode's Fermi level to realize this goal. Detailed theoretical studies to assess the molecule−lead interactions[79] would also be incisive.

## 3.5 References


1. Genereux, J. C.; Barton, J. K., *Chem. Rev.* **2010,** 110, 1642-1662.
2. Lewis, F. D.; Young, R. M.; Wasielewski, M. R., *Acc. Chem. Res.* **2018,** 51, 1746-1754.
3. Lewis, F. D.; Wu, T.; Zhang, Y.; Letsinger, R. L.; Greenfield, S. R.; Wasielewski, M. R., *Science*, **1997**, 277, 673-676.
4. Fink, H.-W.; Schönenberger, C., *Nature* **1999,** 398, 407-410.
5. Kelley, S. O.; Jackson, N. M.; Hill, M. G.; Barton, J. K., *Angew. Chem., Int. Ed.* **1999,** 38, 941-945.
6. Giese, B.; Amaudrut, J.; Köhler, A.-K.; Spormann, M.; Wessely, S., *Nature*, **2001,** 412, 318-320.
7. Xu, B.; Zhang, P.; Li, X.; Tao, N., *Nano Lett.* **2004,** 4, 1105-1108.
8. Risser, S. M.; Beratan, D. N.; Meade, T. J., *J. Am. Chem. Soc.*, **1993,** 115, 2508-2510.
9. Jortner, J.; Bixon, M.; Langenbacher, T.; Michel-Beyerle, M. E., *Proc. Natl. Acad. Sci. U.S.A.*, **1997**, 95, 12759-12765.
10. Renaud, N.; Berlin, Y. A.; Lewis, F. D.; Ratner, M. A., *J. Am. Chem. Soc.*, **2013,** 135, 3953-3963.
11. Beratan, D. N., *Annu. Rev. Phys. Chem.* **2019**, 70, 71-97.
12. Beratan, D. N.; Liu, C.; Migliore, A.; Polizzi, N. F.; Skourtis, S. S.; Zhang, P.; Zhang, Y., *Acc. Chem. Res.*, **2015,** 48, 474-481.
13. Korol, R.; Segal, D., *J. Phys. Chem. C*, **2018**, 122, 4206-4216.
14. Beratan, D. N.; Priyadarshy, S.; Risser, S. M., *Chem. Biol.* **1997**, 4, 3-8.
15. Priyadarshy, S.; Risser, S.; Beratan, D., *J. Phys. Chem.* **1996,** 100, 17678-17682.
16. Teo, R. D.; Rousseau, B. J.; Smithwick, E. R.; Di Felice, R.; Beratan, D. N.; Migliore, A., *Chem* **2019,** 5, 122-137.
17. Kilgour, M.; Segal, D., *J. Chem. Phys.* **2015**, 143, 024111.
18. Berlin, Y. A.; Burin, A. L.; Ratner, M. A., *J. Am. Chem. Soc.*, **2001**, 123, 260-268.
19. Berlin, Y. A.; Kurnikov, I. V.; Beratan, D.; Ratner, M. A.; Burin, A. L., DNA electron transfer processes: Some theoretical notions. In *Long-Range Charge Transfer in DNA II*, Schuster, G. B., Ed. Springer: Berlin, **2004**; pp 1-36.
20. Venkatramani, R.; Davis, K. L.; Wierzbinski, E.; Bezer, S.; Balaeff, A.; Keinan, S.; Paul, A.; Kocsis, L.; Beratan, D. N.; Achim, C., *J. Am. Chem. Soc.*, **2011**, 133, 62-72.
21. Xiang, L.; Palma, J. L.; Bruot, C.; Mujica, V.; Ratner, M. A.; Tao, N., *Nat. Chem.*, **2015**, 7, 221.
22. Michaeli, K.; Beratan, D. N.; Waldeck, D. H.; Naaman, R., *Proc. Natl. Acad. Sci.*, **2019**, 116, 5931-5936.

23. Buttiker, M., *IBM J. Res. Dev.* **1988,** 32, 63-75.

24. Di Felice, R.; Calzolari, A.; Molinari, E.; Garbesi, A., *Phys. Rev. B*, **2001**, 65, 045104.

25. Livshits, G. I.; Stern, A.; Rotem, D.; Borovok, N.; Eidelshtein, G.; Migliore, A.; Penzo, E.; Wind, S. J.; Di Felice, R.; Skourtis, S. S., *Nat. Nanotechnol.*, **2014**, 9, 1040.

26. Wierzbinski, E.; Venkatramani, R.; Davis, K. L.; Bezer, S.; Kong, J.; Xing, Y.; Borguet, E.; Achim, C.; Beratan, D. N.; Waldeck, D. H., *ACS Nano*, **2013,** 7, 5391-5401.

27. Wolak, M. u. A.; Balaeff, A.; Gutmann, S.; Helmrich, H. J.; Vosloo, R.; Beerbom, M. M.; Wierzbinski, E.; Waldeck, D. H.; Bezer, S.; Achim, C., *J. Phys. Chem. C* **2011,** 115, 17123-17135.

28. Paul, A.; Bezer, S.; Venkatramani, R.; Kocsis, L.; Wierzbinski, E.; Balaeff, A.; Keinan, S.; Beratan, D. N.; Achim, C.; Waldeck, D. H., *J. Am. Chem. Soc.* **2009,** 131, 6498-6507.

29. Beall, E.; Sargun, A.; Ulku, S.; Bae, Y.; Wierzbinski, E.; Clever, C.; Waldeck, D. H.; Achim, C., *J. Phys. Chem. C* **2018,** *122* (13), 7533-7540.

30. Liu, C.; Xiang, L.; Zhang, Y.; Zhang, P.; Beratan, D. N.; Li, Y.; Tao, N., *Nat. Chem.* **2016**, 8, 941-945.

31. Šponer, J.; Leszczyński, J.; Hobza, P., *J. Phys. Chem.* **1996,** 100, 5590-5596.

32. Voityuk, A. A., *J. Chem. Phys.* **2008**, 128, 03B608.

33. Hatcher, E.; Balaeff, A.; Keinan, S.; Venkatramani, R.; Beratan, D. N., *J. Am. Chem. Soc.* **2008**, 130, 11752-11761.

34. Venkatramani, R.; Keinan, S.; Balaeff, A.; Beratan, D. N., *Coord. Chem. Rev.* **2011**, 255, 635-648.

35. Wierzbinski, E.; de Leon, A.; Yin, X.; Balaeff, A.; Davis, K. L.; Reppireddy, S.; Venkatramani, R.; Keinan, S.; Ly, D. H.; Madrid, M., *J. Am. Chem. Soc.* **2012,** 134, 9335-9342.

36. Beall, E.; Ulku, S.; Liu, C.; Wierzbinski, E.; Zhang, Y.; Bae, Y.; Zhang, P.; Achim, C.; Beratan, D. N.; Waldeck, D. H., *J. Am. Chem. Soc.* **2017**, 139, 6726-6735.

37. Zhang, Y.; Liu, C.; Balaeff, A.; Skourtis, S. S.; Beratan, D. N., *Proc. Natl. Acad. Sci.* **2014**, 111, 10049-10054.

38. Egholm, M.; Buchardt, O.; Christensen, L.; Behrens, C.; Freier, S. M.; Driver, D. A.; Berg, R. H.; Kim, S. K.; Norden, B.; Nielsen, P. E., *Nature*, **1993**, 365, 566-568.

39. Xu, B.; Tao, N. J., *Science*, **2003**, 301, 1221-1223.

40. Beall, E.; Yin, X.; Waldeck, D. H.; Wierzbinski, E., *Nanoscale*, **2015**, 7, 14965-14973.

41. Van Wees, B.; Van Houten, H.; Beenakker, C.; Williamson, J. G.; Kouwenhoven, L.; Van der Marel, D.; Foxon, C., *Phys. Rev. Lett.*, **1988**, 60, 848.

42. Afsari, S.; Li, Z.; Borguet, E., *Angew. Chem., Int. Ed.* **2014,** 53, 9771-9774.

43. Komoto, Y.; Fujii, S.; Nishino, T.; Kiguchi, M., *Beilstein J. Nanotechnol.* **2015,** 6, 2431-2437.

44. Hanwell, M. D.; Curtis, D. E.; Lonie, D. C.; Vandermeersch, T.; Zurek, E.; Hutchison, G. R., *J. Cheminf.* **2012**, 4, 17.

45. Schrödinger Release 2019-4: Maestro, *Schrödinger, LLC, New York, NY, 2019.*

46. Yeh, J. I.; Pohl, E.; Truan, D.; He, W.; Sheldrick, G. M.; Du, S.; Achim, C., *Chem. Eur. J.* **2010**, 16, 11867-11875.

47. Hart, K.; Foloppe, N.; Baker, C. M.; Denning, E. J.; Nilsson, L.; MacKerell Jr, A. D., *J. Chem. Theory Comput.* **2012**, 8, 348-362.

48. Jasiński, M.; Feig, M.; Trylska, J., *J. Chem. Theory Comput.* **2018**, 14, 3603-3620.

49. Jorgensen, W. L.; Chandrasekhar, J.; Madura, J. D.; Impey, R. W.; Klein, M. L., *J. Chem. Phys.*, **1983**, 79, 926-935.

50. Zgarbová, M.; Otyepka, M.; Sponer, J.; Lankas, F.; Jurečka, P., *J. Chem. Theory Comput.* **2014**, 10, 3177-3189.

51. Phillips, J. C.; Braun, R.; Wang, W.; Gumbart, J.; Tajkhorshid, E.; Villa, E.; Chipot, C.; Skeel, R. D.; Kale, L.; Schulten, K., *J. Comput. Chem.* **2005**, 26, 1781-1802.

52. Pacher, T.; Cederbaum, L.; Köppel, H., *J. Chem. Phys.*, **1988**, 89, 7367-7381.

53. Ridley, J.; Zerner, M., *Theor. Chim. Acta*, **1973**, 32, 111-134.

54. Zeng, J.; Hush, N.; Reimers, J., *J. Am. Chem. Soc.*, **1996**, 118, 2059-2068.

55. Voityuk, A. A., *Chem. Phys. Lett.*, **2006**, 427, 177-180.

56. Kubař, T.; Elstner, M., *J. Phys. Chem. B*, **2008**, 112, 8788-8798.

57. Kubař, T.; Kleinekathöfer, U.; Elstner, M., *J. Phys. Chem. B*, **2009**, 113, 13107-13117.

58. Boese, A. D., *ChemPhysChem*, **2015**, 16, 978-985.

59. Peverati, R.; Truhlar, D. G., *J. Phys. Chem. Lett.* **2011,** 2, 2810-2817.

60. Zheng, J.; Xu, X.; Truhlar, D. G., *Theor. Chem. Acc.*, **2011,** 128, 295-305.

61. Frisch, M. J. T., G. W.; Schlegel, H. B.; Scuseria, G. E.; Robb, M. A.; Cheeseman, J. R.; Scalmani, G.; Barone, V.; Petersson, G. A.; Nakatsuji, H.; Li, X.; Caricato, M.; Marenich, A. V.; Bloino, J.; Janesko, B. G.; Gomperts, R.; Mennucci, B.; Hratchian, H. P.; Ortiz, J. V.; Izmaylov, A. F.; Sonnenberg, J. L.; Williams-Young, D.; Ding, F.; Lipparini, F.; Egidi, F.; Goings, J.; Peng, B.; Petrone, A.; Henderson, T.; Ranasinghe, D.; Zakrzewski, V. G.; Gao, J.; Rega, N.; Zheng, G.; Liang, W.; Hada, M.; Ehara, M.; Toyota, K.; Fukuda, R.; Hasegawa, J.; Ishida, M.; Nakajima, T.; Honda, Y.; Kitao, O.; Nakai, H.; Vreven, T.; Throssell, K.; Montgomery, J. A., Jr.; Peralta, J. E.; Ogliaro, F.; Bearpark, M. J.; Heyd, J. J.; Brothers, E. N.; Kudin, K. N.; Staroverov, V. N.; Keith, T. A.; Kobayashi, R.; Normand, J.; Raghavachari, K.; Rendell, A. P.; Burant, J. C.; Iyengar, S. S.; Tomasi, J.; Cossi, M.; Millam, J. M.; Klene, M.; Adamo, C.; Cammi, R.; Ochterski, J. W.; Martin, R. L.; Morokuma, K.; Farkas, O.; Foresman, J. B.; Fox, D. J., *Gaussian 16, Revision B. 01, Gaussian Inc., Wallingford CT, 2016*.

62. Li, C.; Pobelov, I.; Wandlowski, T.; Bagrets, A.; Arnold, A.; Evers, F., *J. Am. Chem. Soc.*, **2008,** 130, 318-326.

63. Haiss, W.; Martín, S.; Leary, E.; Zalinge, H. v.; Higgins, S. J.; Bouffier, L.; Nichols, R. J., *J. Phys. Chem. C*, **2009,** 113, 5823-5833.

64. Humphrey, W.; Dalke, A.; Schulten, K., *J. Mol. Graphics*, **1996,** 14, 33-38.

65. Tan, B.; Hodak, M.; Lu, W.; Bernholc, J., *Phys. Rev. B*, **2015,** 92, 075429.

66. Neaton, J. B.; Hybertsen, M. S.; Louie, S. G., *Phys. Rev. Lett.*, **2006,** 97, 216405.

67. Teo, R. D.; Terai, K.; Migliore, A.; Beratan, D. N., *Phys. Chem. Chem. Phys.*, **2018,** 20, 26063-26067.

68. Roca-Sanjuán, D.; Rubio, M.; Merchán, M.; Serrano-Andrés, L., *J. Chem. Phys.*, **2006,** 125, 084302.

69. Kawai, K.; Majima, T., *Acc. Chem. Res.*, **2013,** 46, 2616-2625.

70. Evers, F.; Korytár, R.; Tewari, S.; van Ruitenbeek, J. M., *Rev. Mod. Phys.*, **2020,** 92, 035001.

71. Tivanski, A. V.; He, Y.; Borguet, E.; Liu, H.; Walker, G. C.; Waldeck, D. H., *J. Phys. Chem. B*, **2005,** 109, 5398-5402.

72. Bruot, C.; Xiang, L.; Palma, J. L.; Tao, N., *ACS Nano*, **2015,** 9, 88-94.

73. Frisenda, R.; Stefani, D.; van der Zant, H. S., *Acc. Chem. Res.*, **2018,** 51, 1359-1367.

74. Valdiviezo, J.; Rocha, P.; Polakovsky, A.; Palma, J. L., *ACS Sens.*, **2021,** 6, 477-484.

75. Kim, H.; Kilgour, M.; Segal, D., *J. Phys. Chem. C*, **2016,** 120, 23951-23962.

76. Karasch, P.; Ryndyk, D. A.; Frauenheim, T., *Phys. Rev. B*, **2018,** 97, 195401.

77. Carey, R.; Chen, L.; Gu, B.; Franco, I., *J. Chem. Phys.*, **2017,** 146, 174101.

78. Jin, Y.; Ru, X.; Su, N. Q.; Mei, Y.; Beratan, D. N.; Zhang, P.; Yang, W., *J. Phys. Chem. B*, **2020,** 124, 3428-3435.

79. Bag, S.; Biswas, T.; Jain, M.; Maiti, P. K., *J. Phys. Chem. C*, **2020,** 124, 16763-16772.

## 4.0 Benchmarking Chiral Induced Spin Selectivity Measurements - Towards Meaningful Comparisons of Chiral Biomolecule Spin Polarizations

This work was published as Clever, C., Wierzbinski, E., Bloom, B. P., Lu, Y., Grimm, H. M., Rao, S. R., Horne, S. W., Waldeck, D. H. *Isr. J. Chem.*, **2022**, *62*, e202200045. The author of the dissertation performed the measurements for Phosphoserine and N-acetyl cysteine methyl ester and subsequent analyses, compiled literature data to develop a consistent reference terminology, and wrote the manuscript.

This work presents new results and summarizes literature results on the chiral induced spin selectivity (CISS) effect observed for amino acids, peptides, and DNA. To facilitate robust comparisons between measurements of different types and by different groups, we propose a convention for describing the spin-dependent properties of chiral materials and apply it in the discussion. Different phenomena known to affect the sign and magnitude of the spin polarization are described and critically analyzed, including: the molecule's orientation, the molecule's dipole moment direction with respect to the electron propagation direction, the molecular length, the molecule/substrate interface, and the role of the molecule's secondary structure. Lastly, we identify open key questions about spin-filtering by biomolecules at interfaces.

## 4.1 Introduction

Since its discovery in 1999,[1] the Chiral Induced Spin Selectivity (CISS) effect has shown remarkable potential for applications in enantioseparations,[2-7] photovoltaics,[8] spintronics,[9-15] and catalysis,[16,23] among others.[24,25] The phenomenon of electron spin filtering through chiral molecules, assemblies, and materials has been shown for both organic[26-33] and inorganic substances.[34-41] Although considerable effort has been expended toward understanding the mechanistic underpinnings of CISS, the factors that determine the preferred electron spin direction and the magnitude of the CISS response remain under debate.[42-43] This work combines new results on the CISS response of amino acids and peptides with previous results from the literature to define the current status and to identify open questions for identifying structure-function properties for CISS in biomolecules.

Many different experimental techniques have been developed and are currently being employed for measuring the CISS response. These methods include, but are not limited to, i) photoemission spectroscopy - where the electron spin direction is measured directly by a Mott polarimeter or indirectly by changes in a magnetized substrate's work function, ii) atomic force microscopy (AFM) measurements - in contact mode using a conductive probe to measure current-voltage (i-V) characteristics or in non-contact mode using Kelvin probe, iii) electrochemical methods - to monitor the variation in redox potential or current with a magnetized ferromagnetic electrode, or iv) Hall bar measurements - where a polarizing voltage (gate) is applied across a chiral film or current is driven through a chiral film by electrochemical oxidation or reduction. As the measured quantity in each of the experiments differ, it is useful to understand how the information can be compared among experimental methods. To this end, we

(and others) define the spin polarization as a normalized difference in the experimental signal magnitude under opposite magnetizations; see Equation 4.1.

Measurements of spin selectivity often use a magnetized ferromagnetic substrate, electrode, or AFM tip as an analyzer for sensing the preferred spin orientation within an experiment. While the interpretation of the findings within an experiment is often robust, the sign of the reported spin polarization depends on the experimental geometry and the convention used to define the magnetization. The lack of a uniform convention for reporting measurements can make comparisons between experiments and their interpretation confusing. For example, consider the case of a magnetic conductive atomic force microscopy (mc-AFM) experiment. Here i-V measurements are typically reported in reference to the ferromagnetic material, magnetized north (south) or with spin-down (spin-up) electrons.

Figure 4.1 shows how differences in the experimental setup can affect the sign of the reported CISS response in an mc-AFM experiment. For instance, a magnetic tip magnetized with the North pole of a magnet applied to the back of the tip will exhibit an opposite spin polarization to that found if instead the substrate is ferromagnetic and magnetized with a North pole applied to the underside of the substrate (Figure 4.1a). Likewise, the magnetization state of a ferromagnetic tip is opposite, with respect to the transport trajectory, if the tip is magnetized from the top face or the bottom face (see Figure 4.1b). These differences are further compounded by the instrumental set-up; the transport trajectory, from tip to substrate or from substrate to tip, under positive bias is defined by the instrumental ground (see Figure 4.1c) and is not always reported by workers. Because the electron trajectory affects the preferred spin state for an electron moving through a chiral molecule, apparent inconsistencies among measurements can arise if the choice of ground is different and not reported.

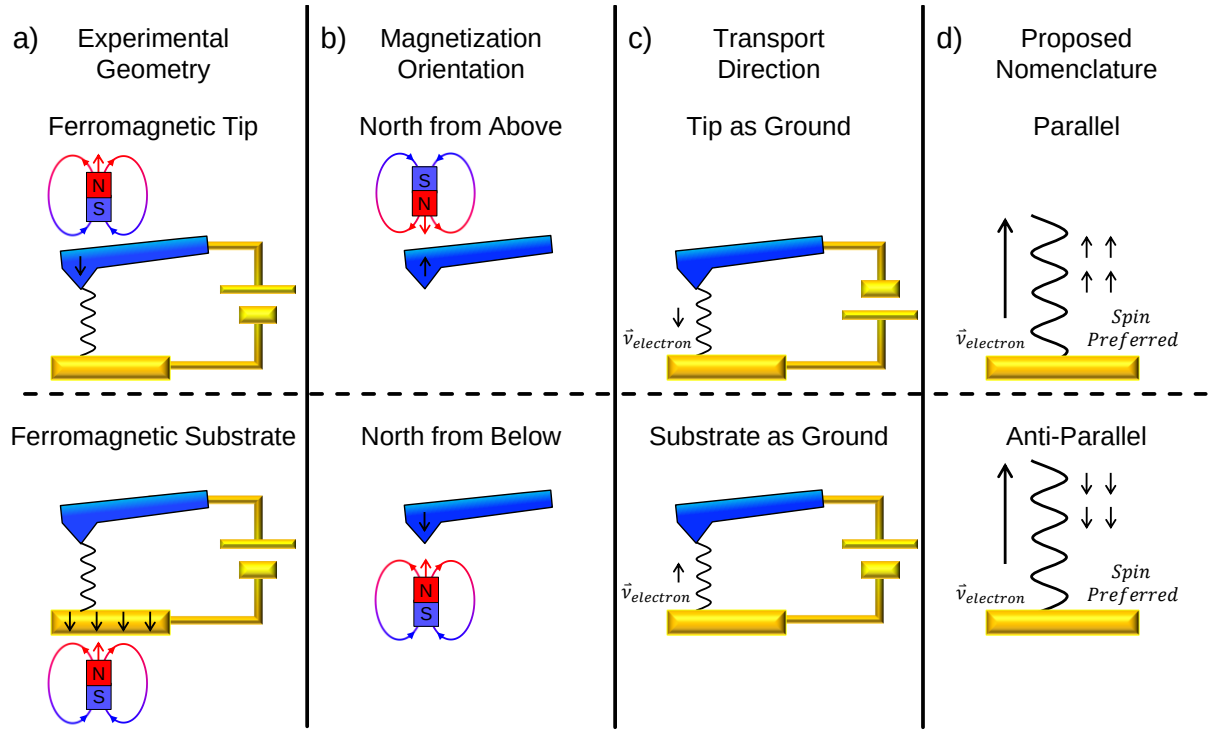


**Figure 4.1 Different experimental arrangements for mc-AFM based on tip versus substrate magnetization (a), magnetization orientation for a magnetized tip (b), electron transport direction based on instrumental ground (c). Panel (d) shows a convention for describing the CISS effect which is robust across different experiments.**

To circumvent issues arising from the use of different conventions and to promote meaningful comparisons among the studies of different workers, we propose a uniform definition of spin polarization arising from the CISS effect with respect to the electron's reference frame. More specifically we advocate that the orientation of the electron spin be specified with respect to the electron's velocity direction; i. e., either as oriented parallel or anti-parallel to the electron velocity, as illustrated in Figure 4.1d. In accordance with this nomenclature, we define the spin polarization, *SP*, as

$$SP(\%) = \frac{A_{parallel} - A_{anti-parallel}}{A_{parallel} + A_{anti-parallel}} * 100 \qquad \textbf{Equation 4.1}$$

where *A* is the experimentally measured quantity and the subscript, parallel or anti-parallel, specifies the spin direction of the electrons relative to their velocity vector.

In this study we describe some of the known limitations associated with CISS measurements and report on recent findings by our group, as well as summarizing other studies, on the molecular properties known to correlate with the CISS response in biomolecules. We begin by describing the CISS response of simple chiral molecules, such as amino acids, and proceed to more complex molecules to identify the key molecular properties that correlate with the magnitude and sign of the CISS response; e. g., the dependence of *SP* on length of the chiral molecule, dipole direction, electron propagation dependence, and structural helicity.

## 4.2 Results and Discussion

### 4.2.1 Amino Acids

CISS manifests for simple systems that possess only a single stereocenter. Because of its natural affinity for metals, the amino acid cysteine and its assemblies have been used to probe spin-selective transport. One such study constructed a spin valve device with the architecture Au-cysteine SAM-alumina-Ni and reported magnetoresistance values of ≈10%.[44]

While most efforts have used cysteine, the generation of spin selectivity in molecules with a single stereocenter does not require the presence of a thiol. Figure 4.2 shows Hall Effect data for self-assembled monolayer films of the amino acid phosphoserine on GaN. The measured Hall voltage is plotted as a function of an applied voltage (or 'Gate') on the film; see Figure 4.2b. The data show that monolayers comprising L-phosphoserine (red) have a positive

response (increasing Hall voltage with increasing gate voltage), corresponding to an anti-parallel spin polarization with the molecules' electron displacements, whereas monolayers comprising D-phosphoserine (blue) display an opposite Hall voltage response, corresponding to a parallel spin preference. Figure 4.2c plots the Hall voltage data versus the gate voltage for a series of measurements on L- (red) and D- (blue) phosphoserine films. Figure 4.2e shows circular dichroism (CD) spectra of L- (red) and D-phosphoserine (blue), which have an opposite response for the two enantiomers, as in the Hall data. These results indicate that the spin polarization depends on the molecule's enantiomeric form and is consistent with other findings for the CISS effect.[45]

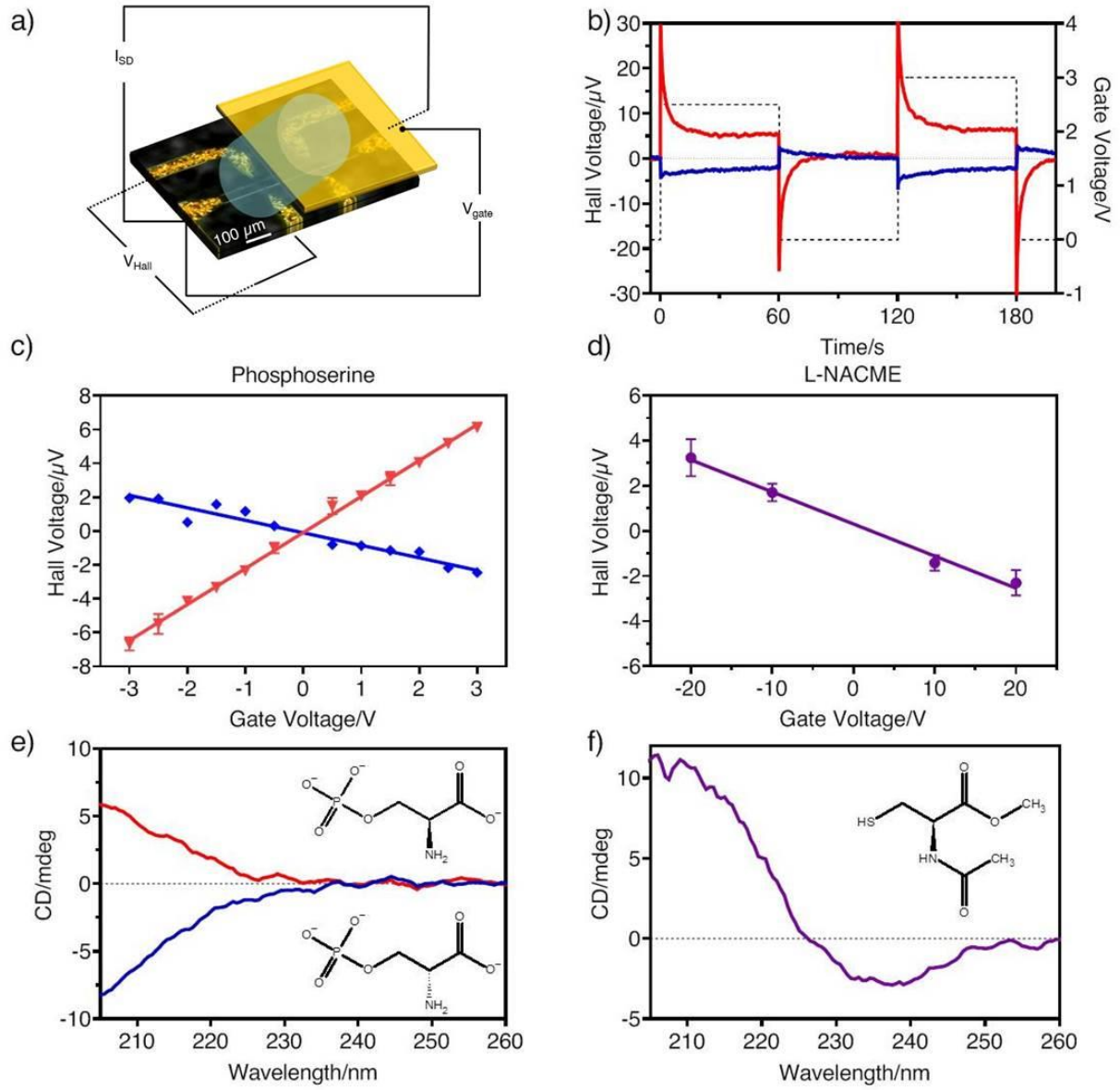


**Figure 4.2 Panels (a) and (b) show the experimental setup for the Hall effect polarization and a sample polarization measurement for L-phosphoserine (red) and D-phosphoserine (blue) at a gate voltage of 3 V. Panel (c) shows Hall voltage responses as a function of gate voltage for L-phosphoserine and D-phosphoserine monolayers. Panel (d) shows the same response for L-NACME (violet). CD spectra are shown for 0.4 mM L- and D-phosphoserine in pH 8 phosphate buffer (e) and 0.25 mM L-NACME in ethanol (f).**

Some literature reports have sought to use the chiroptical response, strength of circular dichroism (CD) signal, as a predictor for the CISS–mediated spin polarization.[28,46] Predicting

the sign of the SP is nontrivial, however; and comparisons must be drawn with care, despite the initial correlations reported between *SP* and the CD signal.[46] For example, if a spin-polarized current is measured for SAMs of an oligopeptide, which is linked to the surface via the N-end, and compared to that for the same oligopeptide, which is linked to the surface via the C-end, they display a different sign for the *SP*, *vide infra*.

To examine the connection of CD response to SP further, the Hall voltage response (Figure 4.2d) and CD spectrum (Figure 4.2f) for assemblies of N-acetyl-L-cysteine methyl ester (L-NACME) were measured. The different ranges of gate voltage applied between the phosphoserine and the L-NACME arises from differences in the substrate and the linker group. The CD spectrum of L-NACME has the same rotation direction for plane-polarized light as L-phosphoserine for its lowest energy feature (220 nm to 250 nm), and it has a negative slope for the Hall data. Note however, that the higher energy CD transition (200-220 nm) is positive, like that of D-phosphoserine. This CD peak is believed to correlate to a combination of the $\pi \rightarrow \pi^*$ and $n \rightarrow \pi^*$ transitions of the carbonyl chromophore in amino acids and peptides.[45] These Hall data corroborate earlier findings about the correlation of the lowest energy CD transition with the CISS response, which were found for electron transfer rates and for tunneling currents.

Studies involving the enantiospecific crystallization of racemic solutions of amino acids on magnetized ferromagnetic substrates show that the CD response is not always a "good predictor" for the sign of the CISS response.[3,6] Bhowmick *et al.*[3] showed that a North magnetized substrate gives rise to enantiospecific crystallization of L-glutamic acid, L-threonine, and D-asparagine, even though the L-glutamic acid and L-threonine display Cotton effects that are opposite to that of the D-asparagine. This unexpected enantiopreference was attributed to differences in the binding orientation for asparagine on the substrate as compared to the glutamic

acid and threonine, and this inference was corroborated by DFT calculations.[6] These studies illustrate that the molecule's binding orientation to the surface impacts the CISS response.

The enantiospecific adsorption of cysteine (and its derivatives) on ferromagnetic surfaces has also been explored using electrochemical quartz crystal microbalance (EQCM) methods. Lu *et al.* showed that the enantiopreference of cysteine for a magnetized surface is a kinetically controlled process, rather than the result of a thermodynamic stabilization.[47] Their measurements with a magnetized Ni/Au electrode showed a difference between the adsorption kinetics of L- and D-cysteine to the substrate that changed with whether the surface was magnetized North or South. Interestingly, they found that the preferred kinetics for adsorption depends on the pH of the solution; at pH 8 the adsorption rate was faster for a North magnetized substrate whereas at pH 9 the kinetics were faster for a South magnetized substrate. The change in enantiopreference with pH was rationalized by the ionization state of the cysteine and its pH dependent adsorption geometry on the electrode surface.[47] Thus this study further supports the claims of Tassinari *et al.*[6] that the binding geometry on a substrate can play an important role in dictating the CISS response.

#### 4.2.1.1 Spin polarization in chemical reactions

CISS also manifests for chemical reactions with amino acids. Mondal *et al.* reported an enantiospecific spin preference for electron transfer with assemblies of a toluidine blue O dye that was covalently bound to an Au/Ni electrode through a cysteine linker group.[68] Here, a change in Faradaic current during oxidation (reduction) of 5-10% was observed and found to depend on the magnetization state (North vs South) of the underlying nickel.[68] The effect was attributed to a change in the electron transport through the chiral cysteine which depends on

whether the majority spin of the electrons from the ferromagnetic electrode match the preferred spin of the cysteine or not.

Spin polarized electrons have also been shown to affect the propensity of chiral molecules to decompose enantioselectively. Rosenberg and coworkers coated magnetic substrates with the chiral amino acids histidine and cysteine,[48,49] and studied their decomposition under photoelectron fluences. Their studies showed that the decomposition depends on the spin polarization of the photoelectrons and the enantiomeric form of the amino acids. For L-histidine, an *SP* of ~19% was reported for photoelectrons ejected by X-rays incident on a magnetized Co substrate. An enantiomeric excess (ee) of 17% was estimated, with a fluence of $\sim 10^{17}$ $e^{-}/cm^2$ and with approximately 40% of the original molecular population remaining.

Collectively, these studies demonstrate that even a single stereocenter can produce a significant spin polarization. In different experiments, the CISS response correlates with the chiroptical properties of the molecule, e. g., L-cysteine consistently shows a positive *SP*, and the CD spectrum of the chiral molecule in solution correlates with the *SP* for most of the different amino acids (and their derivatives) which have been studied. The correlation is not universal however. For example, Lu *et al.*[47] showed that the spin polarization associated with the adsorption rate of cysteine on Au changes with pH, and these changes correlate with known changes in the molecule's adsorption geometry and ionization state with pH. Studies of chiral imprinting on semiconductor nanoparticles[50,51] corroborate the inference that the molecular binding geometry on a surface and the charge exchange at the substrate/molecule interface can have on chiroptical response.

### 4.2.2 Dipole and Propagation Direction Dependence

The direction of electron propagation through a chiral molecule's dipolar field has also been shown to affect the spin polarization. The first reports of this dependence originate from the work by Naaman and coworkers.[52,53] Using photoemission experiments, they compared the spin polarization produced by polyalanine peptide SAMs in which the cysteine linker group was on the C-terminus to those in which the cysteine linker was attached to the N-terminus.[53] The photoelectron yield was ~10% higher for right-circularly polarized light than for left-circularly polarized light when D-polyalanine was bound to the gold through the C-terminus, however D-polyalanine bound to gold through the N-terminus gave the opposite dependence. These experiments demonstrate that the preferred electron spin for transport through a chiral molecule correlates with the direction of the molecule's dipole moment.

To further demonstrate the relationship between the electron propagation direction through the molecule and the spin filtering, we performed mc-AFM measurements for a pair of water-soluble helical peptides, $HSCH_2CH_2CO–\{AUAKAUKAKAUY\}–NH_2$ (peptide 1 N in Figure 4.3a) and $CH_3CO–\{AUAKAUKAKAUY\}–NHCH_2CH_2SH$ (peptide 1 C in Figure 4.3a) where A, U, K, and Y represent alanine, aminoisobutyric acid, lysine, and tyrosine respectively. A CoCr tip was magnetized and the current versus voltage curves were measured through SAMs comprising the oligopeptides. For oligopeptides with a thiol linker on the N-terminus (Figure 4.3b), a higher current was observed when the tip was magnetized such that the electron spins were oriented parallel to their velocity (solid lines) than when the electron spins were oriented anti-parallel (dashed lines). The dependence on magnetization indicates that the electron is preferentially transmitted through peptide 1 N when the electron's spin is aligned parallel to its propagation direction. For the same measurement on peptide 1 C (linker attached to the

C-terminus), the anti-parallel orientation was found to display a higher current than the parallel orientation (Figure 4.3c). An *SP* can be calculated from the asymmetry in *i-V* characteristics with magnetic field as defined by Equation 4.1 and is shown for peptide 1 N (black, 44%) and peptide 1 C (blue, 32%) in Figure 4.3d.

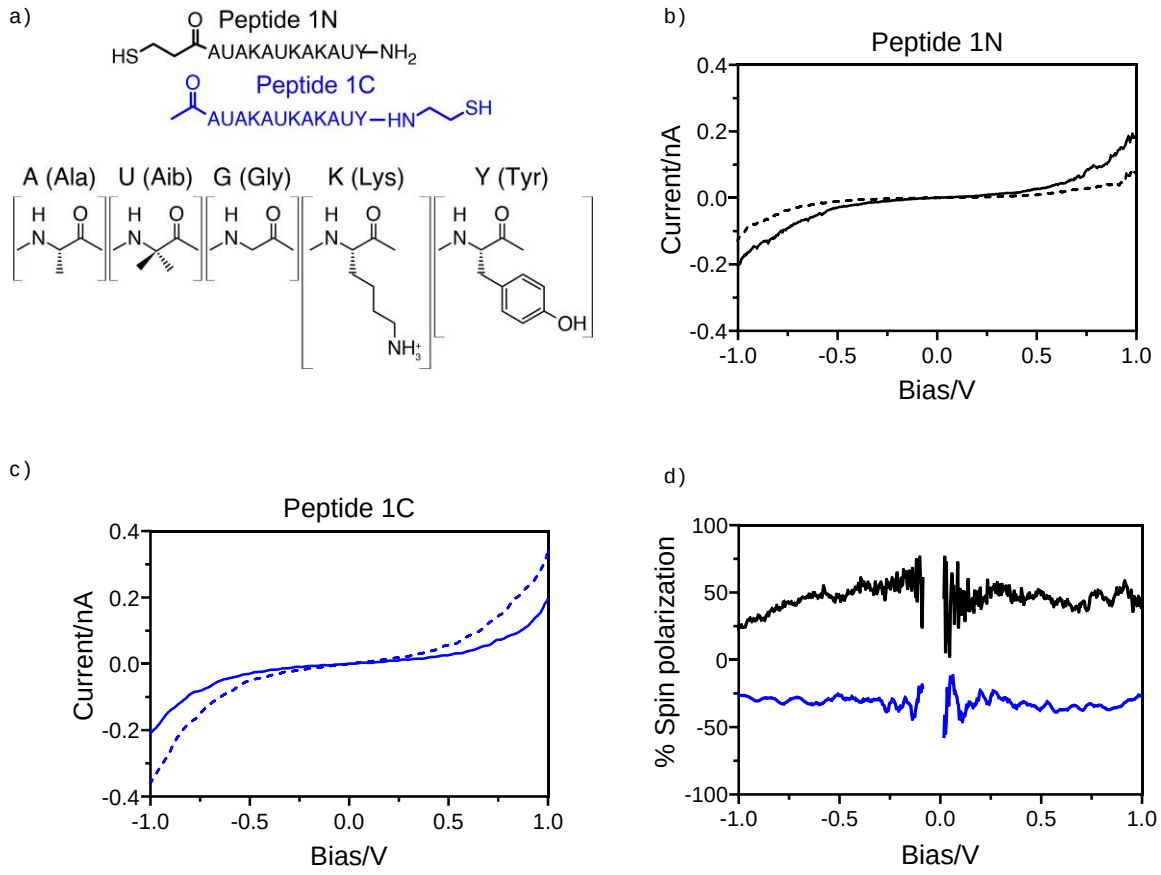


**Figure 4.3. Panel (a) shows the molecular structures of peptides 1 N and 1 C. Panels (b) and (c) show magnetic conductive probe AFM currentvoltage curves for peptide 1 N with the linker on the N-terminus (panel (b), black) and peptide 1 C with linker on the C-terminus (panel (c), blue) with the electron spin polarization oriented parallel (solid line) or anti-parallel (dashed line). The percent spin polarization, which was calculated by Equation 4.1 for each binding geometry, is shown in panel (d).**

Theoretical modeling by Dalum *et al.*[54] indicates that the *SP*, resulting from the CISS effect, depends on the coupling to the leads and the incoming energy of the electrons passing

through a molecule. In addition, they found that when two leads are joined by a chiral molecule, and one lead is magnetic, a spin-polarized current generates an equilibrium state with both leads becoming magnetically polarized. An analogous phenomenon has been demonstrated experimentally by Ghosh *et al.* in which the magnetization state of a ferromagnetic substrate was shown to affect the surface charge of a chiral monolayer.[55]

### 4.2.3 Length Dependence

One of the most well studied CISS phenomena is the dependence of the spin polarization magnitude on the length of the chiral molecules through which the electrons travel. Several studies have examined the length dependent *SP* generated by electron transport through oligopeptides of the structure HS-$CH_2$-$CH_2$-CO-{Ala-Aib}$_n$-COOH, where Aib indicates aminoisobutyric acid and *n* is the number of Ala-Aib units.[56-58,63] Using mc-AFM, Mishra *et al.* found a roughly linear increase in *SP* with peptide length for self-assembled monolayers (SAMs) of these oligopeptides. As the length increased from $n = 3$ to $n = 7$, the magnitude of the polarization increased from -31% to -46%.[56] Corroborating these studies, Kumar *et al.* showed that the Hall voltage generated by charge polarization of SAMs comprising the same peptides exhibit a systematic increase with increasing oligopeptide length (see Figure 4.2b for an example of a Hall measurement).[57,58] Measurements have also been made by Kettner *et al.*, on {Ala-Leu}$_n$ oligopeptides, where Leu represents leucine, using electrochemical reduction (oxidation) and by Mott polarimetry. All of these measurements show a trend of increasing spin polarization magnitude with increasing peptide length.[59]

Literature data for the length dependence of *SP* for oligopeptides is compiled in Table 4.1 and Table 4.2. Note that the {Ala-Aib}$_n$ SAMs were formed by a thiol linker attached to the

N-terminus of the peptide and are denoted as {Ala-Aib}$_n$N, whereas for the {Ala-Leu}$_n$ oligopeptides the thiol linker was attached to the C-terminus and are denoted as {Ala-Leu}$_n$C. As discussed above the change in the terminus of the thiol linker results in an opposite spin preference relative to the electron propagation velocity and can account for the differences in the sign of the *SP* between {Ala-Aib}$_n$ and {Ala-Leu}$_n$ oligopeptides in Table 4.1. Additionally, when only the C-terminus thiol linker of the {Ala-Leu}$_n$ oligopeptide is bound to nickel (electrochemistry measurements) or gold (photoemission measurements), an anti-parallel *SP* is observed. However, when the N-terminus is deprotected and its thiol linker is bound to a gold nanoparticle also (mc-AFM measurement), a parallel *SP* is seen. Another caveat to note is that the change in sign need not apply for comparisons among oligopeptides attached to a substrate through different linker groups. For example, the *SP* measured for an {Ala-Aib}$_n$ SAM on an Au surface by a thiol group attached on the N-terminus shows that a parallel spin polarization alignment is preferred, whereas a SAM of the same oligopeptide attached to a GaN surface through a carboxyl group on the C-terminus of the oligopeptide also shows a parallel spin polarization, see Table 4.2.[57] These data indicate that the observed difference in the sign of the *SP* that is found for phosphoserine and NACME, *vide supra*, could be a product of the different linker group and binding geometry. These studies clearly illustrate the importance of the chemical details of the linker group and the substrate in determining the *SP* of a molecular assembly. Although the exact nature of this phenomenon has not yet been elucidated, theoretical work indicates that the *SP* depends on the charge interchange between the substrate and the linker group.[54] Additional theoretical studies[60-62] suggest that the substrate can contribute to the experimentally observed *SP*s through spin-orbit and electronic coupling with the molecule at the interface.

**Table 4.1 Summary of spin polarizations for oligopeptides. Unless noted, the peptides are attached to a gold surface via thiol linkers.**

| Molecule | Spin Polarization (%) | Spin Polarization Alignment | Method | Reference |
|---|---|---|---|---|
| $\{Ala\text{-}Aib\}_3N$ | 31±3 | Parallel | mc-AFM, 3nN, ±2V | 56 |
| $\{Ala\text{-}Aib\}_4N$ | 37±4 | Parallel | mc-AFM, 3nN, ±2V | 56 |
| $\{Ala\text{-}Aib\}_5N$ | 40±3 | Parallel | mc-AFM, 3nN, ±2V | 56 |
| $\{Ala\text{-}Aib\}_6N$ | 43±4 | Parallel | mc-AFM, 3nN, ±2V | 56 |
| $\{Ala\text{-}Aib\}_7N$ | 46±3 | Parallel | mc-AFM, 3nN, ±2V | 56 |
| $\{Ala\text{-}Aib\}_5N$ | 18[a] | Parallel | mc-AFM, 5nN, ±1V | 63 |
| $\{Ala\text{-}Aib\}_7N$ | 25[a] | Parallel | mc-AFM, 5nN, ±1.5V | 63 |
| $\{Ala\text{-}Aib\}_5N$ | 5 to 40 | Parallel | mc-AFM, 4nN to 7nN, 0-1V | 64 |
| $\{Ala\text{-}Aib\}_7N$ | 11 to 47 | Parallel | mc-AFM, 3nN to 8nN, 0-1V | 64 |
| $\{Ala\text{-}Leu\}_5C$ | -11±3 | Anti-Parallel | Photoemission | 59 |
| $\{Ala\text{-}Leu\}_5C$ | -7±3[b] | Anti-Parallel | Electrochemistry | 59 |
| $\{Ala\text{-}Leu\}_6C$ | -14±1 | Anti-Parallel | Photoemission | 59 |
| $\{Ala\text{-}Leu\}_6C$ | -13±3[b] | Anti-Parallel | Electrochemistry | 59 |
| $\{Ala\text{-}Leu\}_7C$ | -17±1 | Anti-Parallel | Photoemission | 59 |
| $\{Ala\text{-}Leu\}_7C$ | -16±3[b] | Anti-Parallel | Electrochemistry | 59 |
| $\{Ala\text{-}Leu\}_7C$ | 43[c] | Parallel | mc-AFM, 10nN, ±1.5V | 59 |
| Peptide 1C | -32±3 | Anti-Parallel | mc-AFM, 5nN, ±1V | This work |
| Peptide 1N | 44±7 | Parallel | mc-AFM, 5nN, ±1V | This work |
| Peptide 2N | 29±9 | Parallel | mc-AFM, 5nN, ±1V | This work |
| Peptide 3N | 6±14 | Parallel | mc-AFM, 5nN, ±1V | This work |

a) In reference 63 the peptide is bound by the C-terminus carboxyl group to a nickel surface.
b) In reference 59 the peptide is bound by the C-terminus thiol group to a nickel surface for the electrochemical measurements.
c) In reference 59 the peptide is bound by the C-terminus thiol group to a nickel surface and by an N-terminus thiol linker an Au nanoparticle for the mc-AFM measurement.

Table 4.2 reports studies of the same peptides, as reported in Table 4.1, measuring the Hall effect voltage generated by the CISS response. Because of differences in the experimental approach among the data in Table 4.1 and that in Table 4.2, Equation 4.1 does not easily apply. However, within each study, the trend of increasing CISS response with length persists. Note however, the Hall data display different magnitudes for the two cases; the experiments labelled polarization have a much weaker response than those labeled transmission. In the polarization experiments, no current is passed through the chiral SAM. Instead, a voltage is applied across an

ideally polarizable electrode in order to charge-polarize the SAM. In the transmission experiments, current is allowed to flow through the SAM in a reduction or oxidation reaction with the underlying electrode surface.

While the differences in Hall voltage magnitude are not currently understood, below we provide some possible explanations. For the charge polarized SAMs, the electron delocalization, which is responsible for generating the spin polarization, is not uniform throughout the molecules upon application of a polarizing voltage; thus limiting the Hall voltage compared to electrochemical experiments where the electrons transit entirely through the SAM. Moreover, the magnetic dipoles generated in a charge polarized SAM could possess components which cancel, either through interactions among adjacent molecules or even different regions of the same molecule, and effectively reduce the observed Hall response. It is also possible that the interfacial tunneling barrier (metal electrode/chiral molecule interface) dominates the CISS response of a chiral SAM or that spin-torque transfer generates a local magnetization on the substrate for the case with net current flow. Such differences in the SAM: substrate interface at 'steady state' between the two measurement methods could alter the Hall voltage magnitude.

**Table 4.2 Summary of spin polarizations measured by the Hall Effect for oligopeptides. Unless noted, the peptides are attached to a gold surface via thiol linkers.**

| Molecule | Hall Response ($V_H/V_G$) (μV/V) | Spin Polarization Alignment | Method | Reference |
|---|---|---|---|---|
| {Ala-Aib}$_4$N | -0.18 | Parallel | Hall Effect: Polarization | 56 |
| {Ala-Aib}$_5$N | -0.21 | Parallel | Hall Effect: Polarization | 56 |
| {Ala-Aib}$_6$N | -0.25 | Parallel | Hall Effect: Polarization | 56 |
| {Ala-Aib}$_7$N | -0.28 | Parallel | Hall Effect: Polarization | 56 |
| {Ala-Aib}$_5$N | -0.095[a] | Parallel | Hall Effect: Polarization | 57 |
| {Ala-Aib}$_7$N | -0.13[a] | Parallel | Hall Effect: Polarization | 57 |
| **Molecule** | **Hall Response ($V_H^{red}$-$V_H^{ox}$) (μV)** | **Spin Polarization Alignment** | **Method** | **Reference** |
| {Ala-Aib}$_5$N | -14[b] | Parallel | Hall Effect: Transmission | 58 |
| {Ala-Aib}$_7$N | -55[b] | Parallel | Hall Effect: Transmission | 58 |
| {Ala-Aib}$_9$N | -63[b] | Parallel | Hall Effect: Transmission | 58 |
| **Molecule** | **Hall Response ($\mu V_H$ at 1V vs Ag/AgCl)** | **Spin Polarization Alignment** | **Method** | **Reference** |
| {Ala-Aib}$_4$N | -4.9 | Parallel | Hall Effect: Transmission | 56 |
| {Ala-Aib}$_5$N | -7.9 | Parallel | Hall Effect: Transmission | 56 |
| {Ala-Aib}$_6$N | -11.9 | Parallel | Hall Effect: Transmission | 56 |
| {Ala-Aib}$_7$N | -15.4 | Parallel | Hall Effect: Transmission | 56 |

a) In Reference 57 the peptide is bound by a C-terminus carboxyl group to a GaN surface.
b) In Reference 58 the peptide is bound by a C-terminus carboxyl group to a GaN surface and by an N-terminus thiol group to a silver nanoparticle and this may account for its different magnitude.

While the effect of chiral molecule length on the *SP* is robust, the magnitude of the *SP* measured by different techniques, mc-AFM, Mott polarimetry, and Hall-devices, is often not consistent. Much of this inconsistency may arise from differences in the SAM films (e.g., packing density, tilt angle) and differences in the chiral molecule/substrate interactions. More subtle differences could also be at play. For example, the charge polarization of a macromolecule (e. g., a protein) need not be uniform throughout the molecule; and the subsequent displacement current, which gives rise to the Hall response, need not have the same direction in the molecular frame as that resulting from electron transport through a molecule.

These differences can lead to differences in the magnitude of the CISS response measured by charge polarization induced spin polarization (e.g., Hall-bar measurements) versus those based on electron transmission (e.g., mc-AFM, photoemission).

The effect of the chiral system's length on the magnitude of the CISS response has also been studied for DNA sequences with different numbers of base pairs.[56,65-67,70] Table 4.3 and Table 4.4 summarize the mc-AFM, Mott polarimetry, and Hall effect measurements on DNA. Xie, *et al.*, measured *SP*s of 65–82% for DNA duplexes bound between a Ni substrate and an Au nanoparticle,[66] whereas Mott polarimetry studies by Göhler et al. showed that the same DNA sequences assembled on a gold substrate have an *SP* on the order of 10–30%.[67] A chiral molecule/ferromagnetic interface is more likely to give rise to a stronger spin filtering than an Au interface. Mondal *et al.*[68] showed that the Au overlayer depolarizes the electron spins from the ferromagnetic film and differences in the thickness of the Au overlayer directly impact the measured *SP*. Many experiments use an Au overlayer to inhibit the corrosion of Ni (or Co) magnetic substrates, and these details of the sample composition can affect the observed *SP*. The coverage, packing density, angle relative to the substrate surface,[69] and linker group to the substrate of the molecules can all alter the measured SPs.[68]

**Table 4.3 Summary of spin polarizations for DNA. All systems are attached to a gold surface by thiol linkers on the 3' end of the DNA. In Reference 66 the DNA duplex is bound between a Ni substrate and an Au nanoparticle.**

| Number of Basepairs, 3' | Spin Polarization (%) | Spin Polarization Alignment | Method | Reference |
|---|---|---|---|---|
| 20 | -37.5±4 | Anti-Parallel | mc-AFM, 3nN, ±2V | 56 |
| 30 | -44±4 | Anti-Parallel | mc-AFM, 3nN, ±2V | 56 |
| 40 | -55±5 | Anti-Parallel | mc-AFM, 3nN, ±2V | 56 |
| 50 | -62±4 | Anti-Parallel | mc-AFM, 3nN, ±2V | 56 |
| 26 | -10 | Anti-Parallel | Photoemission | 67 |
| 40 | -33 | Anti-Parallel | Photoemission | 67 |
| 50 | -31 | Anti-Parallel | Photoemission | 67 |
| 78 | -57 | Anti-Parallel | Photoemission | 67 |
| 26 | -65 | Anti-Parallel | mc-AFM, ±2V | 66 |
| 40 | -82 | Anti-Parallel | mc-AFM, ±2V | 66 |
| 50 | -82 | Anti-Parallel | mc-AFM, ±2V | 66 |

The work of Mishra *et al.* shows clearly that the even for the same experimental setup the polarization-based measurements reported in Table 4.4 are very distinct from those where the electron is transmitted through the chiral molecule, as discussed above.[56]

**Table 4.4 Summary of spin polarizations measured by the Hall Effect for DNA. All are attached to a gold surface by thiol linkers on the 3' end of the DNA.**

| Number of Basepairs, 3' | Hall Response ($V_H/V_G$) (μV/V) | Spin Polarization Alignment | Method | Reference |
|---|---|---|---|---|
| 20 | 0.11 | Anti-Parallel | Hall Effect: Polarization | 56 |
| 30 | 0.27 | Anti-Parallel | Hall Effect: Polarization | 56 |
| 40 | 0.37 | Anti-Parallel | Hall Effect: Polarization | 56 |
| 50 | 0.67 | Anti-Parallel | Hall Effect: Polarization | 56 |
| **Number of Basepairs, 3'** | **Hall Response ($\mu V_H$ at 1V vs Ag/AgCl)** | **Spin Polarization Alignment** | **Method** | **Reference** |
| 20 | 8.5 | Anti-Parallel | Hall Effect: Transmission | 56 |
| 30 | 16.6 | Anti-Parallel | Hall Effect: Transmission | 56 |
| 40 | 27.4 | Anti-Parallel | Hall Effect: Transmission | 56 |
| 50 | 34.9 | Anti-Parallel | Hall Effect: Transmission | 56 |

The increase in the magnitude of a chiral molecule's CISS response with the increase in the length of its chiral helix (for a given repeating unit) is made evident by the data in Table 4.1 through Table 4.4. Indeed, even across disparate methods of measurement, the spin-selectivity of electron transmission shows a similar length dependence. Figure 4.4a shows data for oligopeptides by mc-AFM, photoemission, electrochemistry, and Hall effect voltage measurements during the redox reaction of $Fe^{2+}/Fe^{3+}$. The open symbols indicate $\{Ala\text{-}Leu\}_nC$ peptides while the filled symbols indicate $\{Ala\text{-}Aib\}_nN$ sequences. Figure 4.4b shows the data for DNA duplexes. The effect of the basepair sequence is beyond the scope of this analysis, as few of the sequences studied are identical (identical sequences for a given length are denoted by open symbols in Figure 4.4b). The lengths of the oligopeptides were estimated assuming an alpha helical structure of 0.15 nm/ residue and the DNA was taken to increase in length by 0.34 nm/base pair. For the oligopeptides an average slope of 22±4% *SP* (or Hall slope) per nm was found and for DNA an average slope of 2.4±0.2% SP (or Hall slope) per nm was found. The $n$ = 5 data point of Reference 58 was excluded from the slope calculation of the average because of its anomalous value. The oligopeptides show a significantly stronger *SP* dependence per unit length than DNA. While representative CD spectra for the oligopeptides[56] show a monotonic increase with length, the increase per unit length is not necessarily comparable. It is noted that the data in Figure 4.4 only include those experiments where electrons are flowing through the full length of the molecule, as opposed to those where a charge polarization within the molecule is applied.

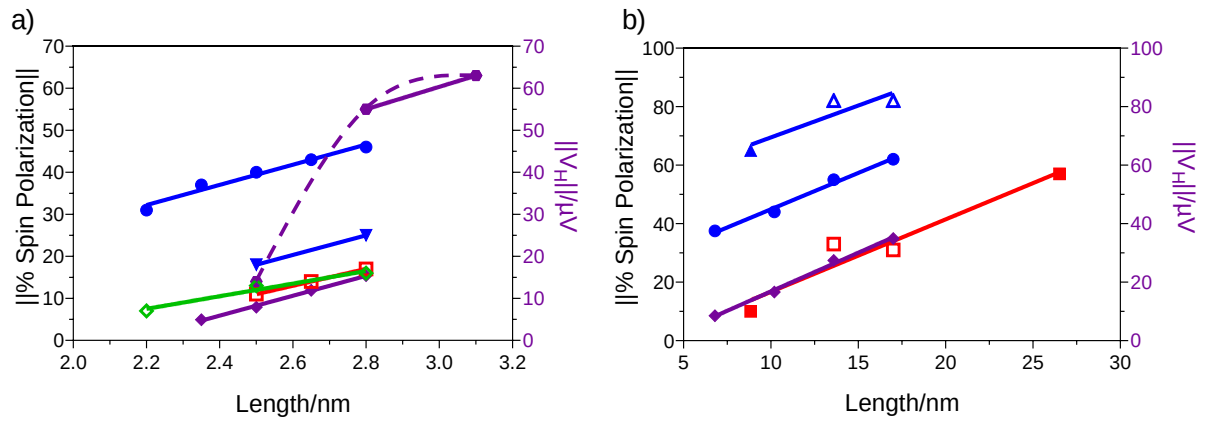


**Figure 4.4 The magnitude of spin polarization as a function of length across multiple experiments. Panel a) shows data for oligopeptides obtained by mc-AFM (References 56 (solid blue circles) and 63 (solid blue triangles)), photoemission (open red squares, Reference 59), electrochemistry (open green diamonds, Reference 59), and Hall voltage with electron transmission (Reference 56 (solid violet diamonds) and 58 (solid violet hexagons), right y-axis). The dashed line follows all the data points, though the shortest was deemed an outlier. Panel b) shows data for DNA obtained by mc-AFM (References 56 (solid blue circles) and 66 (solid blue triangles)), photoemission (red, Reference 67), and Hall voltage with electron transmission (violet diamonds, right y-axis, Reference 56). Open symbols denote identical sequences.**

The similarity of the slopes within each panel of Figure 4.4, despite differing magnitudes of *SP* measured, implies that the dependence of *SP* on length is independent of the specific method used to measure it, provided there is electron transmission through the molecule. More work will be required and a number of questions must still be addressed but the different length dependences in DNA and the peptides may provide a benchmark for theoretical/computational studies of a molecule's CISS response.[28] Some remaining experimental questions include: i) What is the range over which the correlation applies and does a maximum in spin polarization at a particular length manifest? ii) If the length dependence is universal, what causes the difference in length dependence between the DNA and the peptides?

### 4.2.4 Structural Contributions to Spin Polarization

The conformation of the molecule through which the electrons travel can affect the CISS response also. In a study by Göhler *et al.*, single-stranded DNA (ssDNA) showed no detectible *SP*, whereas double-stranded (dsDNA) gave *SP* values of 10% to 57% depending upon the number of base pairs (see Table 4.3), indicating that the helical secondary structure of the DNA contributes significantly to the CISS response.[67] In a similar vein, Zwang *et al.*, showed that changing the DNA helix from the right-handed B-DNA structure to a left-handed Z-DNA, caused the preferential spin transport to switch from anti-parallel to parallel, respectively.[70] Analogous studies with peptide-nucleic acid (PNA) helices show a similar change in preferred SP when comparing left-handed M-PNA to right-handed P-PNA; see Table 4.5.[71]

While right-handed helices of DNA (B-DNA) preferentially transmit electron spins oriented parallel to their velocity, PNA helices show the opposite preference,[71] after accounting for difference in the terminus of the thiol linker. Note that the magnitude of the *SP* for PNA is significant, even though the PNA is composed of achiral monomers. Modification of the γ-carbon on the PNA backbone, which makes the monomer units chiral and produces a helix with a shorter pitch, leads to an increase in the overall spin polarization. This observation suggests that point chirality and axial chirality can be synergistic.

We explored the synergy between axial and point chirality for peptides. A series of peptides with the same number of amino acid units, but different secondary structure content, were synthesized and their CISS response was investigated (Figure 4.5). Peptide 1 N is a water-soluble sequence containing three helix-promoting Aib residues. In peptides 2 N and 3 N, these Aib residues are substituted for Ala and Gly, respectively. The result is a series of sequences of similar size and physical properties but altered folding propensity.

**Table 4.5 Summary of spin polarizations for nucleic acids with differing helical structures. All the molecules are attached to a gold surface by thiol linkers, via the 5'-end for the DNA and the C-terminus for**

| Molecule | Spin Polarization (%) | Spin Polarization Alignment | Method | Reference |
|---|---|---|---|---|
| B-DNA, 16bp, 5' | 21±4 | Parallel | Electrochemistry | 70 |
| Z-DNA, 16bp, 5' | -11±2 | Anti-Parallel | Electrochemistry | 70 |
| B-DNA, 30bp, 5' | 36±5 | Parallel | Electrochemistry | 70 |
| Z-DNA, 30bp, 5' | -19±4 | Anti-Parallel | Electrochemistry | 70 |
| P-PNA, 20bp, C-terminus | 12±4 | Parallel | Photoemission | 71 |
| P-γ-PNA, 20bp, C-terminus | 24±4 | Parallel | Photoemission | 71 |
| M-PNA, 20bp, C-terminus | -7±4 | Anti-parallel | Photoemission | 71 |
| M-γ-PNA, 20bp, C-terminus | -16±4 | Anti-parallel | Photoemission | 71 |

Previously published CD measurements on these peptides in solution (Figure 4.5a) confirm they follow the expected trend in helical content, with peptide 1 N being the most helical (~19%) and peptide 3 N being the least helical (~3%).[72] The spin filtering properties of the peptides were measured by mc-AFM using a magnetized CoCr tip and the average *i*-*V* curves for the SAMs of peptides 1 N (Figure 4.3b), 2 N (Figure 4.5b), and 3 N (Figure 4.5c) with electron momentum parallel (solid line) and anti-parallel (dashed line) to its velocity were measured. The voltage bias dependence of the resulting *SP*s for all three peptides are reported in Figure 4.5d and illustrate that the *SP* increases with increasing peptide helicity. Table 4.6 shows a summary of the *SP* and percent helicity for the peptide series alongside those for the related sequence 1 C from Figure 4.3. The origins of the differing spin preference for the same handedness of a helix, observed in studies of nucleic acids, see Table 4.5, as well as the precise impact of the helix properties, and the strength of their impact on *SP* relative to point chirality are questions left for future studies.

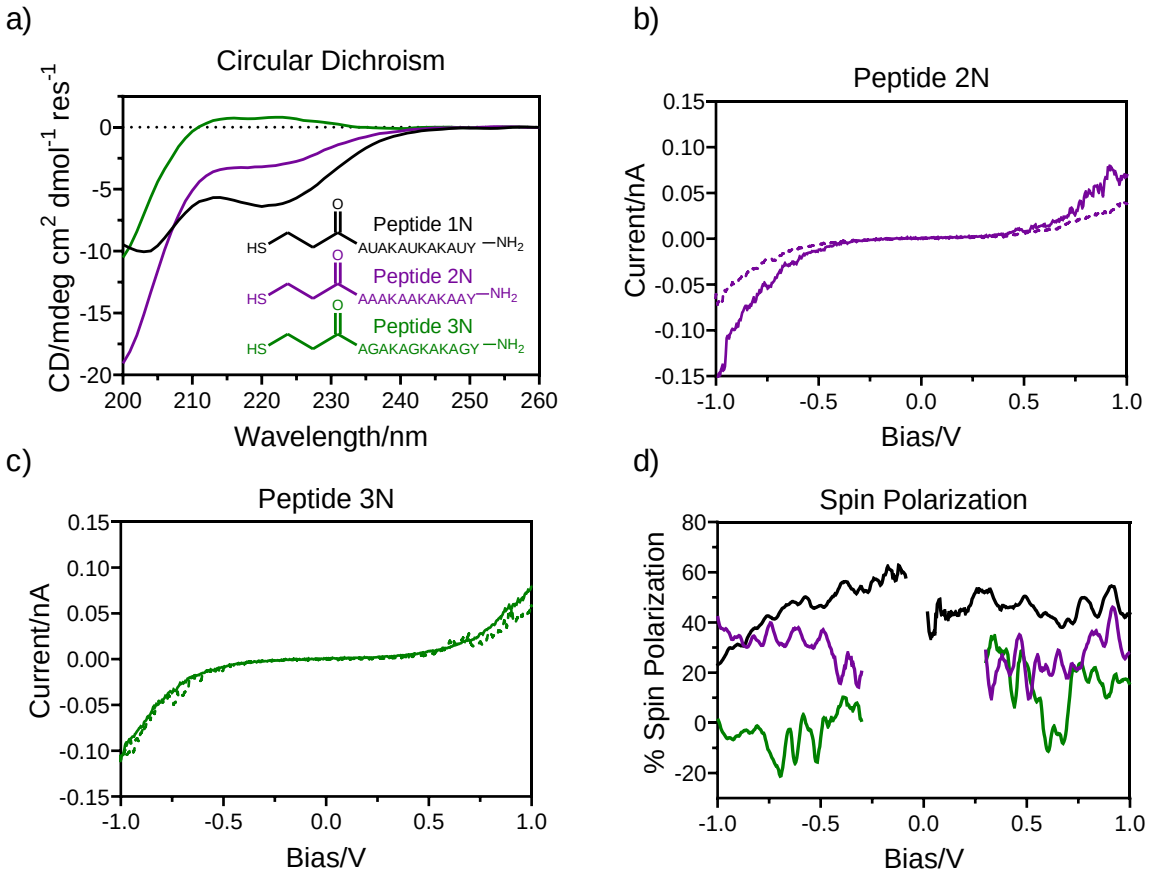


**Figure 4.5 a) Circular dichroism spectra of peptide 1 N (black), 2 N (violet), and 3 N (green), reprinted with permission from Reference 72. Magnetic Conductive Probe-AFM data for Peptide 2 (b) and Peptide 3 (c) with the electron spin polarization oriented parallel (solid line) or anti-parallel (dashed line). The percent spin polarization for each, calculated by Equation 4.1, is shown in Panel (d).**

**Table 4.6 Spin polarizations for peptides of different helicity.**

| Molecule | Spin Polarization (%) | Spin Polarization Alignment | % Helicity |
|---|---|---|---|
| Peptide 1, N-terminus | 44±7 | Parallel | 19% [72] |
| Peptide 1, C-terminus | -32±3 | Anti-Parallel | 15% |
| Peptide 2, N-terminus | 29±9 | Parallel | 9% [72] |
| Peptide 3, N-terminus | 6±14 | Parallel | 3% [72] |

## 4.3 Conclusions

This work summarizes the different phenomena known to affect the CISS response in various chiral biomolecules starting from amino acids with a single stereocenter to more complex molecules like oligopeptides and DNA, which possess a chiral secondary structure.

- The studies on amino acids illustrate that CISS manifests in systems with a single stereocenter and imply that the binding mode/geometry of the molecules at the substrate interface has an important effect on the spin polarization. The spin preference of adsorbed amino acid films can change with the molecules' ionization state and binding mode.
- Secondary structure contributes strongly to an oligomeric molecule's CISS response and can dominate over, or be synergistic with, the molecule's primary structure for spin filtering. The situations in which each may dominate over the other have not yet been addressed. More generally, it will be interesting to assess how chirality can be incorporated on multiple length scales (hierarchical chirality) to improve the CISS response.
- A consideration of the literature data suggest that the trend of increasing spin polarization with length of the chiral system persists through all the studies and that the length dependence is comparable across many experiments. The data also show that the *SP* increase with length is significantly different for peptides and nucleic acids. Given the robust nature of these comparisons, they may serve as a useful testing ground for theoretical/computational studies.
- The dipole moment of a helical peptide relative to the direction of charge transport correlates with the sign of the spin polarization. The effect of charge exchange between the molecule and the substrate has been shown to be significant and may affect both the sign and the

magnitude of the *SP*. Future studies of non-uniform charge distributions or charge reorganization will be useful for a deeper understanding of their effect on the sign and magnitude of the CISS effect.

While much progress has been made toward understanding the details of the CISS effect, numerous questions remain, primarily centered on its magnitude and the quantitative impact of a molecule's structural components. Addressing these questions is important for maximizing the CISS-response, and hence its applicability, in spintronics, photovoltaics, and enantioseparations.

## 4.4 Materials and Methods

### 4.4.1 Peptide Synthesis

Peptides 1 N, 2 N, and 3 N were prepared as detailed previously,[72] employing microwave-assisted Fmoc solid phase methods on NovaPEG Rink Amide resin for synthesis and preparative reverse-phase HPLC for purification. Peptide 1 C was synthesized by microwave-assisted solid-phase methods using a CEM MARS 5 microwave on cysteamine 2-chlorotrityl resin (0.05 mmol scale). Resin was swelled in $CH_2Cl_2$ for 30 min, then washed with DMF prior to the start of the synthesis. Coupling reactions were carried out by adding 0.1 M HCTU in NMP (0.20 mmol) to Fmoc-protected amino acid (0.20 mmol), followed by diisopropylethylamine (0.30 mmol). After a 2 min preactivation, this solution was transferred to resin and the mixture heated to 90°C over a period of 1.5 min, followed by a 2 min hold at that temperature. Coupling reactions for residues $Aib^{11}$ and $Ala^{10}$ employed PyAOP in place of HCTU. Coupling reactions for residues $Aib^{6}$, $Ala^{5}$, $Aib^{2}$, and $Ala^{1}$ employed HATU in place of

HCTU. Fmoc deprotection reactions were carried out by treating resin with 20% v/v 4-methylpiperidine in DMF, heating the mixture to 90°C over a period of 2 min followed by a 2 min hold at that temperature. Resin was washed three times with DMF after each coupling cycle and each deprotection cycle. The N-terminus was acetylated by treatment with 8:2:1 by volume DMF/diisopropylethylamine/acetic anhydride for 20 min at room temperature. Peptide was cleaved from resin by treatment with 2 mL of 92.5/3/3/1.5 by volume trifluoracetic acid (TFA)/$H_2O$/1,2-ethanedithiol/triisopropylsilane. Following agitation for 4 hours at room temperature, resin was filtered and peptide precipitated by addition of cold ether. The pellet was collected by centrifugation, dried under vacuum, and purified by preparative reverse-phase HPLC on a C18 column using gradients between 0.1% TFA in water and 0.1% TFA in acetonitrile. Identity and purity of the final product was confirmed by MALDI-TOF MS and analytical reverse-phase HPLC, respectively.

### 4.4.2 Circular Dichroism Spectroscopy

Circular dichroism (CD) experiments for phosphoserine and L-NACME were carried out on a Jasco J-810 Spectropolarimeter. CD spectra for phosphoserine were acquired from solutions of approximately 0.4 mM in pH 8 phosphate buffer and for L-NACME from a solution of approximately 0.25 mM concentration in ethanol. Scans were acquired on the sample above in a 1 cm path length cuvette at room temperature from 200– 260 nm, 1 nm bandwidth, at a scan rate of 100 nm/min. Circular dichroism (CD) experiments for the peptides were carried out on an Olis DSM 17 spectrophotometer. CD spectral data for peptides 1 N, 2 N, and 3 N were published previously and are reproduced here with permission.[72] A spectrum of peptide 1 C was acquired under the same conditions. Briefly, a stock solution of peptide was prepared in

water with concentration determined by UV absorbance ($\varepsilon_{276}$=1450 $cm^{-1}$ $M^{-1}$ for the single Tyr). This was used to prepare a solution 50 μM peptide in 10 mM phosphate buffer pH 7.2. A scan was acquired on the sample above in a 2 mm pathlength cuvette at 20°C from 200-260 nm with a 1 nm increment, 2 nm bandwidth, and 5 sec integration time. Fraction helicity for each peptide was estimated based on the molar ellipticity at 222 nm following known methods,[73] with limiting values of 34000 and 0 deg $cm^2$ $dmol^{-1}$ $res^{-1}$ for 100% and 0% helicity, respectively.

### 4.4.3 Hall Device Preparation

Hall effect devices were fabricated as reported previously.[57] Prior to use, the devices were cleaned by boiling in acetone and twice in ethanol for at least 30 minutes, etched for 30 seconds in 6 M HCl, rinsed with water and dried under argon stream. The devices were then oxidized in UV/Ozone cleaner for 30 minutes and placed in ethanol for at least 30 minutes prior to incubation. The devices were placed into a 30 mM Phosphoserine solution in pH 8 Tris/EDTA buffer for 24 hours. After incubation, the device was rinsed with water and dried under argon stream.

In the case of L-NACME, 2 nm Ti and 5 nm Au were added to the active area of the device, as in Reference 56 and the device was cleaned by boiling in acetone and ethanol as above, rinsed in ethanol and water and dried under argon stream. The devices were then oxidized in UV/Ozone cleaner for 2 minutes and placed in ethanol for at least 30 minutes prior to incubation. The device was placed into a 5 mM L-NACME solution in ethanol for 24 hours. After incubation, the device was rinsed with ethanol and dried under argon stream.

A cell of polydimethylsiloxane (PDMS) was placed over the device and cured at 45°C for 16 hours.

### 4.4.4 Hall Measurements

Measurements were conducted in 100 mM tetrabutylammonium hexafluorophosphate (TBA-$PF_6$) electrolyte in acetonitrile. Using a Keithley 2636 source measure unit, a constant current of 100 mA for Phosphoserine (50 mA for in the case of L-NACME) is applied between the Source and Drain while a polarizing 'Gate' voltage is applied perpendicular to both the Source-Drain current and the Hall voltage probes. The voltage was electrically insulated from the solution by a ~0.18 mm thick glass slide. The Hall Voltage is measured using a Keithley Nanovoltmeter 2182 A device. The direction of the Source-Drain current was then reversed and the measurements repeated, to account for any asymmetry in the device.

### 4.4.5 Magnetic Conductive Atomic Force Microscopy (mc-AFM) Measurements

Prior to conductance measurements the AFM tip with CoCr coating (Bruker MESP V2, k=3 N/m) was magnetized for 15 min by placing it on a pole (North or South) of a 0.5 T magnet. After magnetizing the AFM tip, the *i-V* traces were collected on a monolayer of a peptide immobilized on ultra-flat gold substrate in an argon atmosphere. After each magnetization of the tip, the measurements were performed for no longer than 2 hours. The loading force applied was 5 nN. The *i-V* traces were collected in random spots on the surface for all the samples.

## 4.5 References


1. K. Ray, S. P. Ananthavel, D. H. Waldeck, R. Naaman, Science 1999, 283, 5403, 814-816.
2. K. Banerjee-Ghosh, O. Ben Dor. F. Tassinari, E. Capua, S. Yochelis, A. Capua, S.-H. Yang, S. S. Parkin, S. Sarkar, L. Kronik, L. T. Baczewski, R. Naaman, Y. Paltil, Science 2018, 360, 1331-1334.
3. D. Bhowmick, Y. Sang, K. Santra, M. Halbauer, E. Capua, Y. Paltiel, R. Naaman, F. Tassinari, Cryst. Growth Des. 2021, 21, 5, 2925–2931.
4. T.S. Metzger, Y. Tokatly, E. Avigad, S. Yochelis, Y. Paltiel, Sep. Purif. Technol., 2020, 239, 116501.
5. C. Wang, A.- M. Gao, Q.- F. Sun, Y. Yan, J. Phys. Chem. Lett., 2021, 12, 10262-10269.
6. F. Tassinari, J. Steidel, S. Paltiel, C. Fontanesi, M. Lahav, Y. Paltiel, R. Naaman, Chem. Sci., 2019, 10, 5246-5250.
7. K. Santra, D. Bhowmick, Q. Zhu, T. Bendikov, R. Naaman. *J. Phys. Chem. C*, **2021**, 125, 17530-17536.
8. J. Wang, H. Lu, X. Pan, J. Xu, H. Liu, X. Liu, D. R. Khanal, M. F. Toney, M. C. Beard, Z. V. Vardeny, *ACS Nano*, **2021**, 15, 588-595.
9. N. Goren, T. K. Das, N. Brown, S. Gilead, S. Yochelis, E. Gazit, R. Naaman, Y. Paltiel, *Nano Lett.* **2021**, 21, 8657-8663.
10. H. Al-Bustami, B. P. Bloom, A. Ziv, S. Goldring, S. Yochelis, R. Naaman, D. H. Waldeck, Y. Paltiel. *Nano Lett.* **2020,** 20, 8675-8681.
11. H. Al-Bustami, G. Koplovitz, D. Primc, S. Yochelis, E. Capua, D. Porath, R. Naaman, Y. Paltiel, *Small*, **2018**, 14, 1801249.
12. S. H. Yang, R. Naaman, Y. Paltiel, S. S. P. Parkin, *Nat. Rev. Phys.* **2021**, 3, 328-343.
13. O. Ben Dor, S. Yochelis, S. P. Mathew, R. Naaman, Y. Paltiel, *Nat. Commun.* **2013**, 4, 2256.
14. G. Koplovitz, D. Primc, O. Ben Dor, S. Yochelis, D. Rotem. D. Porath, Y. Paltiel, *Adv. Mater.* **2017**, 29, 1606748.
15. G. Koplovitz, G. Leitus, S. Ghosh, B. P. Bloom, S. Yochelis, D. Rotem, F. Vischio, M. Striccoli, E. Fanizza, R. Naaman, D. H. Waldeck, D. Porath, Y. Paltiel, *Small*, **2019**, 15, 1804557.
16. K. B. Ghosh, W. Zhang, F. Tassinari, Y. Mastai, O. Lidor-Shalev, R. Naaman, P. Möllers, D. Nürenberg, H. Zacharias, J. Wei, E. Wierzbinski, D. H. Waldeck, *J. Phys. Chem. C* **2019**, 123, 5, 3024-3031.
17. S. Ghosh, B. P. Bloom, Y. Lu, D. Lamont, D. H. Waldeck, *J. Phys. Chem. C* **2020**, 124, 41, 22610-22618.
18. T. S. Metzger, R. Siam, Y. Kolodny, N. Goren, N. Sukenik, S. Yochelis, R. Abu-Reziq, D. Avnir, Y. Paltiel, *J. Phys. Chem. Lett*, **2021**, 12, 23, 5469-5472.

19. W. Zhang, K. Banerjee-Ghosh, F. Tassinari, R. Naaman, *ACS Energy Lett.* **2018**, 3, 10, 2308-2313.

20. F. Tassinari, K. Banerjee-Ghosh, F. Parenti, V. Kiran, A. Mucci, R. Naaman, *J. Phys. Chem. C*, **2017**, 121, 29, 15777-15783.

21. W. Mtangi, F. Tassinari, K. Vankayala, A. V. Jentzsch, B. Adelizzi, A. R. A. Palmans, C. Fontanesi, E. W. Meijer, R. Naaman, *J. Am. Chem. Soc.* **2017**, 139, 7, 2794-2798.

22. T.S. Metzger, S. Mishra, B. P. Bloom, N. Goren, A. Neubauer, G. Shmul, J. Wei, S. Yochelis, F. Tassinari, C. Fontanesi, D. H. Waldeck, Y. Paltiel, R. Naaman. *Angew. Chem.***2020**, 132, 1670 -1675.

23. B. P. Bloom, Y. Lu, T. Z. Metzger, S. Yochelis, Y. Paltiel, C. Fontanessi, S. Mishra, F. Tassinari, R. Naaman, D. H. Waldeck, *Phys. Chem. Chem. Phys.* **2020**, 22, 21570-21582.

24. Y. –H. Kim, Y. Zhai, H. Lu, X. Pan, C. Xiao, E. A. Gaulding, S. P. Harvey, J. J. Berry, Z. V. Vardeny, J. M. Luther, M. C. Beard, *Science*, **2021**, 371, 1129-1133.

25. D. D. Nuzzo, C. Kulkarni, B. Zhao, E. Smolinsky, F. Tassinari, S. C. J. Meskers, R. Naaman, E. W. Meijer, R. H. Friend, *ACS Nano*, **2017**, 11, 12713-12722.

26. V. Kiran, S. P. Mathew, S. R. Cohen, I. Hernández Delgado, J. Lacour, R. Naaman, *Adv. Mater.* **2016**, *28*, 1957-1962.

27. C. Kulkarni, A. K. Mondal, T. K. Das, G. Grinbom, F. Tassinari, M. F. J. Mabesoone, E. W. Meijer, R. Naaman, *Adv. Mater.*, **2020,** 32, 1904965.

28. K. Mondal, M. D. Preuss, M. L. Ślęczkowski, T. K. Das, G. Vantomme, E. W. Meijer, R. Naaman, *J. Am. Chem. Soc.* **2021**, 143, 18, 7189-7195.

29. M. W. Rahman, K. M. Alam, S. Pramanik, *ACS Omega*, **2018**, 3, 17108-17115.

30. C. Aragones, E. Medina, M. Ferrer-Huerta, N. Gimeno, M. Teixido, J. L. Palma, N. Tao, J. M. Ugalde, E. Giralt, I. Diez-Perez, V. Mujica, *Small*, **2017**, 13, 1602519

31. D. Mishra, T. Z. Markus, R. Naaman, M. Kettner, B. Gohler, H. Zacharias, N. Friedman, M. Sheves, C. Fontanesi, *Proc. Natl. Acad. Sci.* **2013**, 110, 14872-14876.

32. S. Mishra, S. Pirbadian, A. K. Mondal, M. Y. El-Naggar, R. Naaman, *J. Am. Chem. Soc.* **2019**, 141, 19198-19202.

33. J. J. Wei, C. Schafmeister, G. Bird, A. Paul, R. Naaman, D. H. Waldeck, *J. Phys. Chem. B*, **2006**, 110, 1301-1308.

34. Z. Huang, B. P. Bloom, X. Ni, Z. N. Georgieva, M. Marciesky, E. Vetter, F. Liu, D. H. Waldeck, D. Sun, *ACS Nano*, **2020**, 14, 10370-13075.

35. B. P. Bloom, V. Kiran, V. Varade, R. Naaman, D. H. Waldeck, *Nano Lett.* **2016**, 16, 4583-4589.

36. H. Lu, J. Wang, C. Xiao, X. Pan, X. Chen, R. Brunecky, J. J. Berry, K. Zhu, M. C. Beard, Z. V. Vardeny, *Science*, **2019**, 5, eaay0571.

37. U. Huizi-Rayo, J. Gutierrez, J. M. Seco, V. Mujica, I. Diez-Perez, J. M. Ugalde, A. Tercjak, J. Cepeda, E. S. Sebastian.*Nano Lett*, **2020**, 20, 8476-8482.

38. K. Mondal *et al*. *ACS Nano* **2020**, *14*, 16624-16633.

39. Inui, R. Aoki, Y. Nishiue, K. Shiota, Y. .Kousaka, H. Shishido, D. Hirobe, M. Suda, J. Ohe, J. Kishine, H. M. Yamamoto, Y. Togawa, *Phys. Rev. Lett.* **2020**, 124, 16, 166602.

40. Y. Nabei, D. Hirobe, Y. Shimamoto, K. Shiota, A. Inui, Y. Kousaka, Y. Togawa, H. M. Yamamoto, *Appl. Phys. Lett.* **2020**, 117, 052408.

41. T. Bai, J. Ai, L. Liao, J. Luo, C. Song, Y. Duan, L. Han, S. Che, *Angew. Chem. Int. Ed.* **2021**, 60, 9421-9426.

42. F. Evers, A. Aharony, N. Bar-Gill, O. Entin-Wohlman, P. Hedegård, O. Hod, P. Jelinek, G. Kamieniarz, M. Lemeshko, K. Michaeli, V. Mujica, R. Naaman, Y. Paltiel, S. Refaely-Abramson, O. Tal, J. Thijssen, M. Thoss, J. M. van Ruitenbeek, L. Venkataraman, D. H. Waldeck, B. Yan, L. Kronik, *Adv. Mater.* **2022**, 34, 2106629.

43. D. Aiello *et al. ACS Nano*, **2022**, 16, 4989-5035.

44. S. P. Shinto, P. C. Mondal, H. Moshe, Y. Mastai, R. Naaman, *Appl. Phys. Lett.* **2014**, 105, 242408.

45. N. Amdursky, M. M. Stevens, *ChemPhysChem*, **2015**, 16, 2768-2774.

46. P. Bloom, B. M. Graff, S. Ghosh, D. N. Beratan, D. H. Waldeck, *J. Am. Chem. Soc.* **2017**, 139, 26, 9038–9043.

47. Y. Lu, B. P. Bloom, S. Qian, D. H. Waldeck, *J. Phys. Chem. Lett.* **2021**, 12, 7854-7858.

48. M. J. Schaible, R. A. Rosenberg, S. Kundu, T. M. Orlando, *J. Phys. Chem. Lett.* **2020**, 11, 10182-10187.

49. R. A. Rosenberg, E. A. Rozhkova, V. Novosad, *Langmuir* **2021**, 37, 2985-2992.

50. Z. Georgieva, Z. Zhang, P. Zhang, B. P. Bloom, D. Beratan, D. H. Waldeck, Ligand Coverage and Exciton Delocalization Control Chiral Imprinting in Perovskite Nanoplatelets, *J. Phys. Chem. C*, **2022**, 126, 37, 15986–15995.

51. V. A. Kuznetsova, E. Mates-Torres, N. Prochukhan, M. Marcastel, F. Purcell-Milton, J. O'Brien, A. K. Visheratina, M. Martinez-Carmona, Y. Gromova, M. Garcia-Melchor, Y. K. Gun'ko, *ACS Nano*, **2019**, 13, 11, 13560–13572.

52. Carmeli, V. Skakalova, R. Naaman, Z. Vager, *Angew. Chem., Int. Ed.* **2002,** 41, 5, 761-764.

53. Carmeli, G. Leitus, R. Naaman, S. Reich, Z. Vager, *Isr. J. Chem.*, **2003,** 43, 399-405.

54. S. Dalum, P. Hedegård, *Nano Lett.* **2019**, 19, 5253-5259.

55. S. Ghosh, S. Mishra, E. Avigad, B. P. Bloom, L. T. Baczewski, S. Yochelis, Y. Paltiel, R. Naaman, D. H. Waldeck, *J. Phys. Chem. Lett.*, **2020**, 11, 1550-1557.

56. S. Mishra, A. K. Mondal, S. Pal, T. K. Das, E. Z. B. Smolinsky, G. Siligardi, R. Naaman, *J. Phys. Chem. C* **2020**, 124, 10776-10782.

57. Kumar, E. Capua, M. K. Kesharwani, J. M. L. Martin, E. Sitbon, D. H. Waldeck, R. Naaman, *Proc. Natl. Acad. Sci. U. S. A.* **2017**, 114, 10, 2474–2478.

58. Kumar, E. Capua, K. Vankayala, C. Fontanesi, R. Naaman, *Angew. Chem. Int. Ed.* **2017**, 56, 14587 –14590.

59. M. Kettner, B. Göhler, H. Zacharias, D. Mishra, V. Kiran, R. Naaman, C. Fontanesi, D. H. Waldeck, S. Sęk, J. Pawłowski, J. Juhaniewicz, *J. Phys. Chem. C*, **2015**, 119, 14542-14547.

60. J. Gersten, K. Kaasbjerg, A. Nitzan, *J. Chem. Phys.* **2013**, 139, 114111.

61. Y. Liu, J. Xiao, J. Koo, B. Yan, *Nat. Mater.*, **2021**, 20, 638-644.

62. S. Alwan, Y. Dubi, *J. Am. Chem. Soc.*, **2021**, 143, 14235-14241.

63. W. Mtangi, V. Kiran, C. Fontanesi, R. Naaman, *J. Phys. Chem. Lett.* **2015**, 6, 4916-4922.

64. V. Kiran, S. R. Cohen, R. Naaman, *J. Chem. Phys.*, **2017**, 146, 092302.

65. R. Naaman, Z. Vager, *Phys. Chem. Chem. Phys.* **2006**, 8, 2217-2224.

66. Z. Xie, T. Z. Markus, S. R. Cohen, Z. Vager, R. Gutierrez, R. Naaman, *Nano Lett.* **2011**, 11, 11, 4652-4655.

67. Göhler, V. Hamelbeck, T. Z. Markus, M. Kettner, G. F. Hanne, Z. Vager, R. Naaman, H. Zacharias, *Science,* **2011,** 331, 894-897.

68. P. Mondal, C. Fontanesi, D. H. Waldeck, R. Naaman, *ACS Nano* **2015**, 9, 3, 3377-3384.

69. N. Sukenik, F. Tassinari, S. Yochelis, O. Millo, L. T. Baczewski, Y. Paltiel, *Molecules*, **2020**, 25, 6036.

70. T. Zwang, S. Hürlimann, M. G. Hill, J. K. Barton, *J. Am. Chem. Soc.*, **2016**, 138, 15551-15554.

71. P. V. Möllers, S. Ulku, D. Jayarathna, F. Tassinari, D. Nürenberg, R. Naaman, C. Achim, H. Zacharias, Chirality, 2021, 33, 93-102.

72. W. Marvin, H. M. Grimm, N. C. Miller, W. S. Horne, G. R. Hutchison, *J. Phys. Chem. B*, **2017**, 121, 10269-10275.

73. R. Banerjee, S. Chattopadhyay, G. Basu, *Proteins*, **2009**, 76, 184-200.

# 5.0 Water Electrolysis and Spin

## 5.1 Past Studies

The electrolysis of water is a reaction of interest for applications such as energy storage and hydrogen fuel cells. The process is defined by the four half-reactions: the oxygen reduction reaction (ORR), the hydrogen oxidation reaction (HOR), the oxygen evolution reaction (OER), and the hydrogen evolution reaction (HER).

ORR: $4H^+ + O_2 + 2e^- \rightarrow 2H_2O$ HER: $2H^+ + 2e^- \rightarrow H_2$

OER: $2H_2O \rightarrow O_2 + 4H^+ + 2e^-$ HOR: $H_2 \rightarrow 2H^+ + 2e^-$

OER and ORR have been shown to be 'improved' by the introduction of electron spin control which changes the preferred mechanism's rate-determining step and inhibits the formation of by-products.[1-3] The improvement is inferred from changes in the reaction overpotential, the rate-determining step of the mechanism, or the faradaic efficiency when efforts are made to spin polarize the electron current being injected into the working electrode (anode for OER and cathode for ORR). These results are attributed to spin polarization of radical intermediates which promote the formation of the triplet ground state of $O_2$.

In recent work we studied chiral and racemic Fe-doped cobalt oxide electrocatalysts and compared their performance, as a way to assess the importance of electron spin filtering.[3] Using a rotating ring-disk electrode (RRDE), we measured the Faradaic efficiency for doped and undoped cobalt oxide; see Figure 5.1, top left. The cobalt oxide catalyst was dropcast onto a glassy carbon disk electrode. In the measurement, the potential at the disk was swept to promote OER. The platinum ring electrode was held at a constant potential of 0.1 V vs RHE. The

electrode is rotated so that the products of the reaction at the disk electrode are driven to the ring electrode, where oxygen is reduced back to water. Thus the ratio of the current at the ring to that at the disk can be used to quantify the faradaic efficiency of the oxygen evolution reaction. Figure 5.1 shows a sample voltammogram for the undoped L-cobalt oxide in 1M NaOH (top right), and the equation for determining the ratio of chiral to achiral faradaic efficiency (bottom left). In both the doped and undoped cases, the ratio of Faradaic efficiency for chiral electrocatalysts versus racemic ones is within error, e.g. ratio of 1, at high pH (1M NaOH); however, the chiral system shows increased efficiency at lower pH (0.1M sodium carbonate at pH 10 and 0.02M potassium phosphate at pH8 buffer solutions). These data are plotted using a bar plot in Figure 5.1, bottom right.

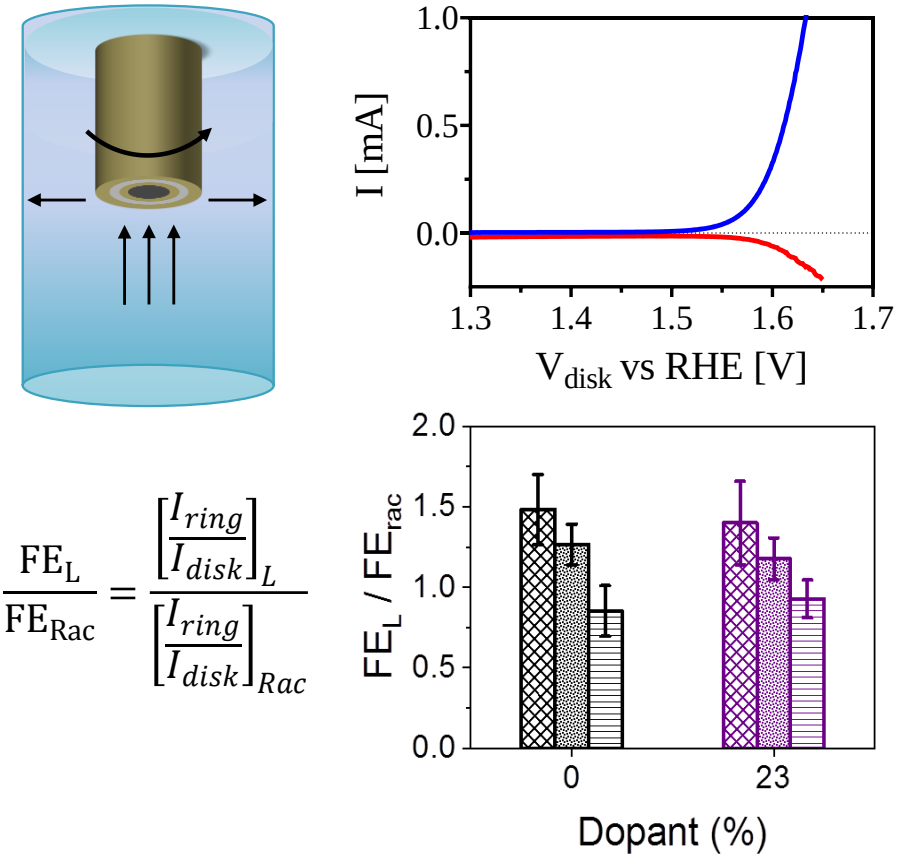


$$\frac{\mathrm{FE_L}}{\mathrm{FE_{Rac}}} = \frac{\left[\frac{I_{ring}}{I_{disk}}\right]_L}{\left[\frac{I_{ring}}{I_{disk}}\right]_{Rac}}$$

**Figure 5.1 Top Left: Diagram of RRDE cell and electrode. Top Right: Sample voltammogram for OER at the disk (blue) and ORR at the ring (red). Bottom Left: Equations for Faradaic Efficiency and the change between chiral and racemic catalysts. Bottom Right: The enhancement in Faradaic efficiency for undoped (black) and 23% Fe-doped (purple) chiral catalysts, compared to their achiral analogs in 1M NaOH (horizontal dash) and in a 0.1M pH 10 sodium carbonate (dotted) and 0.02 M pH 8 potassium phosphate (cross hatched) buffer solutions. The error bars represent the average across at least three independent electrode preparations. Adapted from Reference 3.**

These findings are consistent with previous studies which indicate that the amount of peroxide that can be detected decreases with increasing pH.[4] Hydrogen peroxide is not stable at high pH, chemically decomposing into $O_2$. At lower pH $H_2O_2$ is more stable, and a chiral electrocatalyst is found to proceed more efficiently than an achiral electrocatalyst as the pH decreases towards neutral.[2] These data imply that the introduction of chirality to the

electrocatalyst makes the reaction more selective for the generation of oxygen over hydrogen peroxide. This can be explained by the ground state of oxygen being a triplet state and the ground state of hydrogen peroxide being a singlet state.

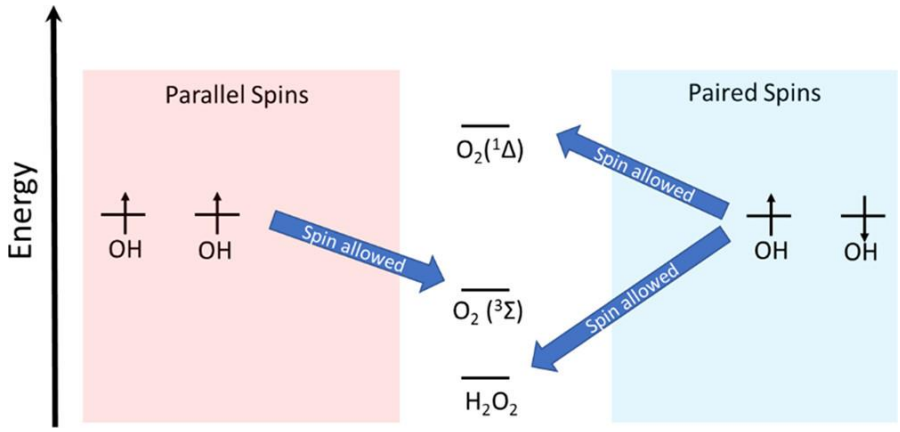


**Figure 5.2 The relative energy levels of the reaction products for OER from the recombination of hydroxyls when the electron spins are aligned versus paired. Reproduced from Reference 5.**

As indicated by the diagram in Figure 5.2, if electron spins are not aligned, the lowest energy product for the combination of hydroxyl groups is hydrogen peroxide. Whereas if the spins are parallel, the formation of $H_2O_2$ is spin-forbidden, and the triplet ground state of $O_2$ becomes the lowest energy spin-allowed pathway.

## 5.2 Hydrogen Evolution Reaction

While the electronic ground state of diatomic oxygen is a triplet, the ground state of diatomic hydrogen is a singlet. Extending the interpretation of spin effects for OER and ORR, we hypothesize that spin polarized electron currents can hinder the hydrogen evolution reaction. As HER competes with the reduction of $CO_2$ and of $N_2$, lowering their efficiency, the inhibition of HER could be used to improve the efficiency of these reactions.[6,7]

The mechanism of the Hydrogen Evolution Reaction (HER) on a metal catalyst is understood to proceed by one of two reaction mechanisms, dependent upon the catalyst and the solution conditions.[8]

| Volmer-Heyrovsky: | Volmer-Tafel: |
| --- | --- |
| Volmer: $H_3O^+ + e^- + M \rightarrow M\text{-}H + H_2O$ | Volmer: $H_3O^+ + e^- + M \rightarrow M\text{-}H + H_2O$ |
| Heyrovsky: $M\text{-}H + H_3O^+ + e^- \rightarrow H_2 + H_2O + M$ | Tafel: $2M\text{-}H \rightarrow H_2 + 2M$ |

The reactions listed above are for an acidic solution and M-H denotes a hydrogen atom adsorbed to the electrocatalyst's surface. The mechanistic steps are the same in neutral or alkaline pH, only with hydroxide ions replacing the water molecules and water replacing the hydronium ions.[9] Both mechanisms have the same first step, the Volmer step, in which a proton in solution is reduced at the catalyst surface and adsorbs as the species denoted M-H. This adsorbed hydrogen can then combine with the reduction of a second proton from solution to form $H_2$, via the Heyrovsky step, or it can react with another adsorbed hydrogen to form $H_2$, via the Tafel step.

In each mechanistic pathway, the adsorption of the hydronium ion (or water molecule, in the case of a more alkaline pH) to the catalyst surface must be the initial step. The subsequent step can then be an electrochemical step, between the adsorbed hydrogen and a second hydronium ion (or water molecule) from solution, in the case of the Volmer-Heyrovsky pathway, or a chemical combination of two of the adsorbed hydrogen species, in the Volmer-Tafel pathway. The rate-determining step of the HER mechanism, i.e. which of these two mechanisms is followed, is dependent on the catalyst choice.[10]

Both the Volmer and Heyrovsky steps incorporate protons from the aqueous solution, which should have no spin preference, as they arise from achiral $H_3O^+$ or some other solvated

proton form. However, the use of a chiral electrolyte should introduce a chiral bias at the interface; we ask whether it will polarize the electron spins being transferred from the electrolyte to the electrode surface and allow for the possibility of a spin-dependence in the Volmer or Heyrovsky steps. If the H-radical intermediates on the electrode surface are spin polarized and the reaction follows the Heyrovsky mechanism, then the HER occurring by this mechanism should be inhibited, as the lowest lying triplet of $H_2$ is not formed.

If the Volmer-Tafel pathway is the preferred mechanism, one should be able to use a ferromagnetic film electrode and polarize the electron spins in the electrode to inhibit the HER. In the presence of a magnetic field, the spin states of the adsorbed M-H will be aligned. Thus the M-H intermediates will be spin aligned, which should inhibit HER because the lowest energy $H_2$ triplet is unbound. Thus $H_2$ singlet state formation should be hindered by spin aligned intermediates which result from spin-polarized electrochemistry. Because the Tafel step is believed to be rate-determining on palladium,[10] it is most likely that the introduction of spin control from a magnetized electrode would impact the reaction in this case.

We performed a series of rotating disk electrode (RDE) measurements on different metal catalysts (Pt, Ni, and Pd), each of which are expected to have a different rate-determining step for the mechanism. The use of tartaric acid as a chiral electrolyte, as well as the magnetization of the working electrode, were used to affect the electron spin in the reaction. To determine the impact of spin control, we examined the 'onset' potential required to achieve a current density of 1 $mA/cm^2$ (by geometric surface area) and the exchange current density, $j_0$, as it is directly proportional to the rate constant. Also, we used the Tafel slope for the reaction, which serves as an indicator for the ease of driving the reaction. A Tafel analysis plots the applied voltage vs the decadic logarithm of the current, and the slope of this plot represents the potential required to

achieve an order of magnitude increase in current density. Lastly, we use the transfer coefficient, α, which denotes the symmetry of the energy barrier.[11]

### 5.2.1 Results and Discussion

#### 5.2.1.1 Platinum

The use of a chiral electrolyte, such as tartaric acid, allows for the possibility of an electrolyte-mediated spin dependence in the reaction pathway. HER at a platinum electrode is believed to proceed by a mechanism in which the Heyrovsky step is rate-determining.[10] HER was performed at a Pt electrode for a series of pH's of solutions of L-, D-, racemic-, and meso-tartaric acid.

Figure 5.3a shows a sample voltammogram for D-tartaric acid at different rotation rates. The Tafel plots for the HER on Pt in alkaline pH, presented in Figure 5.3b, show no significant difference between the HER in enantiopure and racemic tartaric acid solutions. Table 5.1 shows the onset potential, transfer coefficient (α), exchange current density ($j_0$), and Tafel slope for HER on platinum in alkaline and neutral pH in the 50mM tartaric acid solution. The onset potential is taken as the potential required to achieve a current density of 1mA/cm$^2$. In the presence of meso-tartaric acid, a slight hindrance of the HER is observed as a change in Tafel slope and in $j_0$ at alkaline pH. This is contrary to the proposed mechanistic spin dependence. However, at a neutral pH, a slight increase in $j_0$ is observed for meso-tartaric acid, though the Tafel slope is still higher than for the homochiral or racemic tartrate. Racemic tartaric acid exhibits no difference from the enantiopure electrolyte solutions.

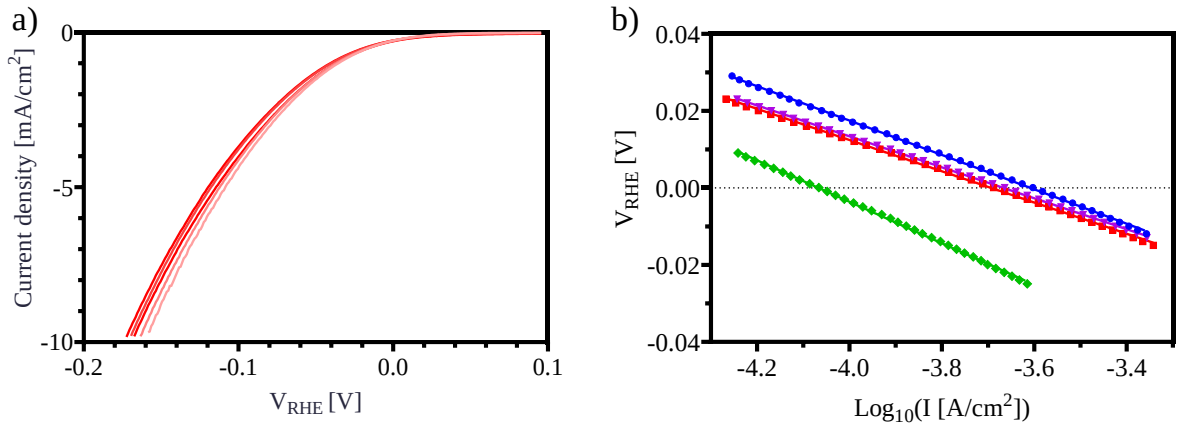


**Figure 5.3 a) HER Voltamograms in 50mM D-tartaric acid, with sufficent KOH to reach a pH≈13, on a Pt rotating disk electrode at 400, 900, 1600, 2500, and 3600 rpm (light to dark), taken at a scan rate of 10mV/s. Panel b) shows the Tafel plot for L- (blue), D- (red), meso- (green), and racemic (violet) tartaric acid.**

**Table 5.1 Reaction parameters observed for HER on platinum in 50mM tartaric acid of different chiralities in KOH, at pH≈7 and 13.**

| | Onset Potential [mV][a] | | Transfer Coefficient, $\alpha$ | | $j_0$ [mA/cm$^2$] | | Tafel Slope [mV/decade] | |
|---|---|---|---|---|---|---|---|---|
| | Neutral | Basic | Neutral | Basic | Neutral | Basic | Neutral | Basic |
| **L-tartrate** | -270±20 | -37±4 | 0.58±0.01 | 0.58±0.01 | 0.7±0.1 | 0.25±0.01 | 44±1 | 45±2 |
| **D-tartrate** | -280±20 | -37±7 | 0.55±0.01 | 0.63±0.01 | 0.7±0.1 | 0.20±0.01 | 47±1 | 40±3 |
| **Rac-tartrate** | -270±20 | -37±5 | 0.56±0.01 | 0.64±0.01 | 0.7±0.1 | 0.22±0.01 | 46±1 | 40±2 |
| **m-tartrate** | -270±30 | -42±9 | 0.47±0.01 | 0.48±0.03 | 0.9±0.1 | 0.086±0.004 | 55±1 | 56±1 |
| **Literature** | ---[d] | ---[d] | | 0.48±0.03[b] | | 0.60±0.08[b] | ≈40[c] | ≈40[c] |

a) Taken at 1 mA/cm$^2$ geometric current density. Potentials are referenced to the Reversible Hydrogen Electrode.
b) Reference 12.
c) Reference 9.
d) Due to the lack of a singular definition[13] for onset potential, no literature values are reported here.

Similarly, at acidic pH only small differences between chiral tartaric acid and its achiral analog were observed, see Table 5.2. Note that due to the solution pH being close to the $pK_a$s of tartaric acid, meso-tartaric acid was not studied as observed changes could not be attributed definitively to chirality as opposed to differences in protonation state of the tartrate.

**Table 5.2 Reaction parameters observed for HER on platinum in 50mM tartaric acid of different chiralities. The tartaric acid solutions were titrated with KOH to achieve a slightly acidic pH.**

| | Onset Potential [mV][a] | | | Transfer Coefficient, α | | | $j_0$ [mA/cm$^2$] | | | Tafel Slope [mV/decade] | | |
|---|---|---|---|---|---|---|---|---|---|---|---|---|
| | **4.5** | **4.9** | **5.1** | **4.5** | **4.9** | **5.1** | **4.5** | **4.9** | **5.1** | **4.5** | **4.9** | **5.1** |
| **L-tartrate** | -35±2 | -57±1 | -58±1 | 0.6± 0.01 | 0.5± 0.01 | 0.5± 0.01 | 0.17± 0.02 | 0.33± 0.03 | 0.18± 0.03 | -43±1 | -49±1 | -53±1 |
| **Rac-tartrate** | -32±2 | -56±1 | -57±1 | 0.5± 0.01 | 0.5± 0.01 | 0.5± 0.01 | 0.25± 0.03 | 0.39± 0.03 | 0.28± 0.03 | -49±1 | -53±1 | -50±1 |
| **Literature** | ---[d] | | | 0.54±0.02[c] | | | 1.0[b]<br>1.12[c]<br>0.62±0.01[c] | | | 45[c] | | |

a) Taken at 1 mA/cm$^2$ geometric current density. Potentials are referenced to the Reversible Hydrogen Electrode.
b) In 0.1-1M $H_2SO_4$. Reference 14.
c) Values not reported with electrode area. Reference 15.
d) Due to the lack of a singular definition[13] for onset potential, no literature values are reported here.

As expected, when the Heyrovsky step is rate-determining, the electrolyte chirality does not affect the HER. The spin states of the protons from solution are not controlled by chiral electrolyte, likely due to the abundance of hydronium (or hydroxide) ions inundating the reaction intermediates with randomized spin states.

### 5.2.1.2 Nickel

The Volmer adsorption step is believed to be rate determining for HER on a nickel surface.[10] We used a Ni-coated magnet as the working electrode (the surface Ni coating is ≈7μm thick) in addition to the chiral electrolyte, with the idea that it will allow for the possibility of cooperative interaction of spin preferences. If the chirality of the electrolyte in solution favors spins that are also favored by the direction of the nickel's magnetic orientation, then a cooperative effect should increase the propensity of the controlled spins to affect the HER. Figure 5.4 presents sample voltammograms (Figure 5.4a) and Tafel plots (Figure 5.4b). Table 5.3 summarizes the reaction parameters for different magnetization directions and chiralities.

Due to the propensity for Nickel to oxidize in aqueous solutions, the literature is sparse and disparate (see Table 5.3).

The change in magnetic field does not show a significant difference in the reaction's kinetic parameters in an L-tartaric acid electrolyte. Nor was there any evidence of a change in the reaction mechanism when the enantiopure electrolyte was replaced with racemic tartaric acid.

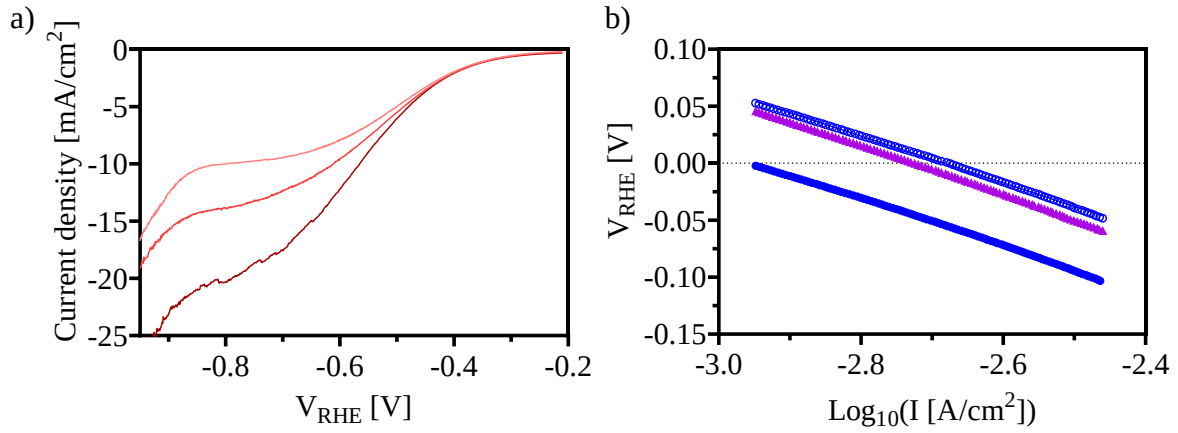


**Figure 5.4 a) HER Voltamograms in a D-tartaric acid solution on the nickel surface of a NdFeB magnet rotating disk electrode at 900, 1600, and 3600 rpm (light to dark), taken at a scan rate of 10mV/s. Panel b) shows the Tafel plot for HER in an L-tartaric acid solution (blue) with the North (filled circles) and South (hollow circles) poles of the magnet as the working electrode, and for racemic tartaric acid at the North pole (violet).**

**Table 5.3 Reaction parameters observed for HER on a nickel magnet in 50mM tartaric acid of different chiralities in KOH, at mildly acidic pH.**

| | Onset Potential [mV][a] | | Transfer Coefficient, α | | $j_0$ [mA/cm$^2$] | | Tafel Slope [mV/decade] | |
|---|---|---|---|---|---|---|---|---|
| | North | South | North | South | North | South | North | South |
| **pH 4.3, L-tartrate** | -360± 20 | -350± 10 | 0.30± 0.01 | 0.30± 0.01 | 2.0±0.1 | | -209±2 | -207±2 |
| **pH 4.3, Rac-tartrate** | -340± 10 | --- | 0.30± 0.01 | --- | 1.9±0.1 | --- | -215±2 | --- |
| **Literature** | ---[d] | | ≈0.5[e] | | 5.8±0.8[b] | | ≈121-142[c] | |

a)Taken at 1 mA/cm$^2$ geometric current density. Potentials are referenced to the Reversible Hydrogen Electrode.
b)Reference 14.
c)In 1M NaOH. Reference 9.
d)Due to the lack of a singular definition[13] for onset potential, no literature values are reported here.
e) Reference 10.

For HER on nickel, the spin states of the reactants come from the solvent, and so, as with the platinum electrode, possess randomized spins. As the Volmer step is rate-determining, this will preclude significant kinetic changes for the HER, despite the aligned spin states on the magnetic electrode.

#### 5.2.1.3 Palladium

For palladium-catalyzed HER, the Tafel step controls the reaction rate.[10] We hypothesize that since the Tafel step comprises two adsorbed hydrogen atoms combining to form diatomic hydrogen, whose ground state is a singlet, that this combination is hindered if the electron spins are aligned by the application of a magnetic field. Figure 5.5a shows the structure of the Palladium electrodes, see Methods for more details. Sample voltammograms and Tafel plots are shown in Figure 5.5b and c, respectively. While there is no evident change in reaction onset nor Tafel slope, the shift in x-intercept of the Tafel plot denotes a change in exchange current density with and without a magnetic field.

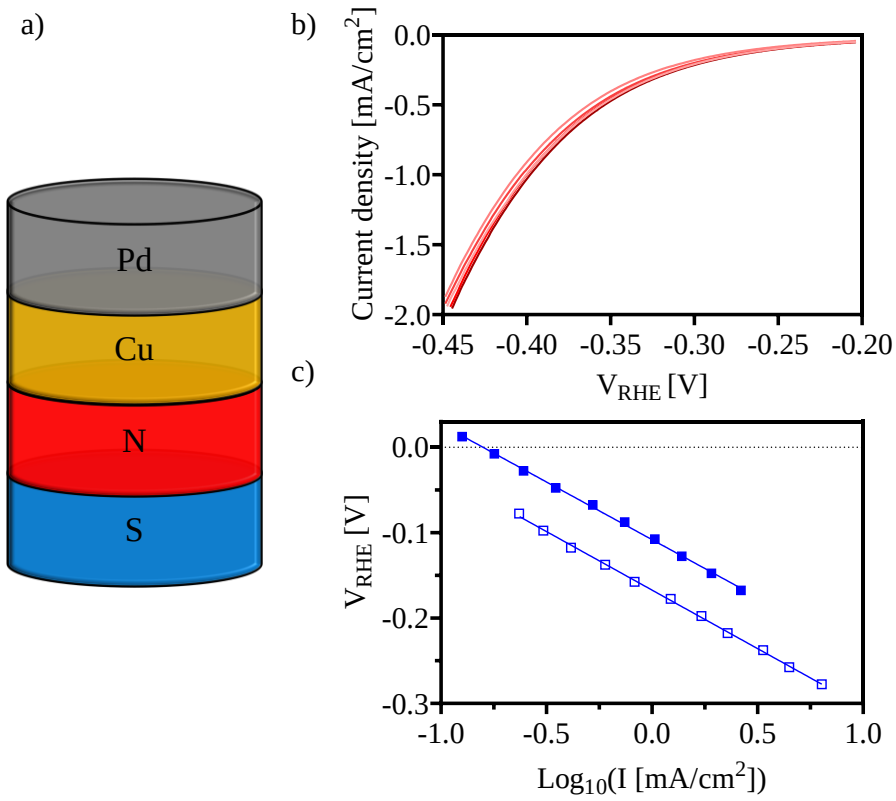


**Figure 5.5 Panel a) shows the construction of the magnetized Pd electrode with the North magnetization. 100nm Pd was evaporated onto a copper disk and subsequently adhered to a Nd magnet with Ag Epoxy. In the case of no magnetic field, the magnet is replaced with a Cu disk. Panel b) shows HER Voltamograms in 0.5M $H_2SO_4$ on a Pd rotating disk electrode at 400, 900, 1600, 2500, and 3600 rpm (light to dark), taken at a scan rate of 10mV/s. Panel b) shows the Tafel plot for Pd with (solid) and without (hollow) an applied magnetic field.**

Table 5.4 shows the onset potential, transfer coefficient (α), exchange current density ($j_0$), and Tafel slope for HER on Pd with and without a magnetic field. The introduction of a magnetic field to the working electrode does not produce significant changes in the onset potential, transfer coefficient, or Tafel slope (i.e. the rate-determining step) for HER. However, there is evidence of a shift in $j_0$ by three to four times, indicating a possible change in the rate constant.

**Table 5.4 Reaction parameters and standard deviations measured for HER on Pd with and without the presence of a magnetic field. Standard deviations are across at least three different electrodes.**

| | Onset Potential [mV][a] | Transfer Coefficient, $\alpha$ | $j_0$ [mA/cm$^2$] | Tafel Slope [mV/decade] |
|---|---|---|---|---|
| **0mT** | -380±20 | 0.20±0.01 | 0.04±0.03 | -135±5 |
| **80mT** | -400±50 | 0.20±0.01 | 0.14±0.03 | -128±6 |
| **Literature** | ---[f] | --- | 3.0±0.6[b]<br>0.9±0.4[c] | -121[d]<br>-127±8[b]<br>-100[e] |

a) Taken at 1 mA/cm$^2$ geometric current density. Potentials are referenced to the Reversible Hydrogen Electrode.
b) In 0.1M $HClO_4$ at 40°C. Reference 12.
c) In 0.1-1M $H_2SO_4$. Reference 14.
d) Reference 16.
e) In $H_2SO_4$. Reference 15.
f) Due to the lack of a singular definition[13] for onset potential, no literature values are reported here.

The use of Pd under an applied magnetic field as a catalyst for HER shows a slight increase in the exchange current density, suggesting that the magnetic field improves the reaction rate for HER, contrary to the hypothesis. However, HER on palladium is not as straightforward as on other catalysts, given the tendency for hydrogen to intercalate into the Pd lattice[10], leading to the rather disparate literature values. Future studies with a stronger magnetic field would also be of importance to better confirm what, if any, effect it has on the hydrogen evolution reaction. In this study, the Palladium was evaporated onto a copper disk to facilitate a robust electrode surface. However, coating Pd directly onto the magnet's surface, or utilizing a Pd-coated or Pd-based permanent magnet would yield a more direct effect on the electron spin of the catalyst electrode, as well as an increased magnetic field strength.

## 5.3 Conclusions

Although the oxygen evolution reaction has been shown to be dependent upon controlled spins, the preliminary studies presented here do not display a clear spin effect for the hydrogen

evolution reaction. We examined a series of metal electrocatalysts for HER, each of which should display a different mechanistic pathway, and affected the electron spins through the introduction of electrolyte chirality or of magnetization of the working electrode. Some differences in the reaction kinetics are noted, however no change in the mechanistic pathways is evident. Given the numerous mechanistic pathways for HER, these data do not preclude the possibility that, under some reaction conditions, controlling spin in the reaction could affect the efficiency of the HER.

## 5.4 Methods

### 5.4.1 Electrode preparation

Platinum electrodes (ALS Co., RDE Platinum disk electrode) were polished to mirror finish using 0.05μm diameter Alumina slurry (Electron Microscopy Sciences). For nickel and palladium, custom disk electrodes were used in a disk replaceable electrode (ALS Co.).

For the measurements on nickel, a cylindrical NdFeB magnet coated with Ni-Cu-Ni (K&J Magnetics, D0505) was polished lightly, so as not to strip the coating, as evidenced by a marked color change when the underlying copper layer becomes exposed.

For the preparation of pallidum electrodes, copper disks were polished to mirror finish using 0.05μm diameter Alumina slurry. Then the disks were placed in a Plassys Electron Beam Evaporator (MEB550S). The samples were further cleaned for 3 minutes using Ar RIE at 250mV and a 100nm film of Pd was evaporated onto the surface. A Neodymium magnet (McMaster-Carr) was attached to the rear of the Pd/Cu electrode with Ag Epoxy (Chemtronics

CW2400) and allowed to cure at room temperature for ≈18 hours. The strength of the magnetic field at the electrode surface was approximately 80mT as measured by a Gauss Meter (PCE-MFM 3000). For measurements with no magnetic field, a copper disk was attached in lieu of the magnet.

### 5.4.2 Electrochemical measurements

Rotating disk electrode measurements were conducted using an RDE (ALS Co., RRDE-3A). The reference electrode was Ag/AgCl in 3 M KCl (CH Instruments) and the counter electrode was a Pt wire. A CHI 750c bipotentiostat was used for all electrochemical measurements.

For high pH measurements, potassium hydroxide was added to 50mM tartaric acid until the desired pH was reached. Measurements on palladium were conducted in 0.5M $H_2SO_4$. In all cases, the solution was purged with Ar for 15 minutes.

Prior to RDE measurements, the surface was cleaned electrochemically via the oxidation and subsequent reduction of the metal surface, ensuring a fresh metal surface. For hydrogen evolution, the potential was swept from -0.07 to -0.5 V vs RHE at a scan rate of 10 mV/s and rotation rates of 400, 900, 1600, 2500, and 3600rpm.

## 5.5 References


1. Sang, Y., Tassinari, F., Santra, K., Zhang, W., Fontanesi, C., Bloom, B.P., Waldeck, D.H., Fransson, J., Naaman, R., *Proc. Natl. Acad. Sci. U. S. A.*, **2022**, *119*(30), p.e2202650119.
2. Ghosh, S., Bloom, B. P., Lu, Y., Lamont, D., Waldeck, D. H., *J. Phys. Chem. C*, **2020**, *124*(41), 22610-22618.
3. Vadakkayil, A.; Clever, C.; Kunzler, K. N.; Tan, S.; Bloom, B. P.; Waldeck, D. H., *Nat. Commun.*, **2023**, *14*, 1067.
4. Khataeea, A., Sajjadia, S., Pourana, S.R., Hasanzadeha, A., Jooc, S.W., *Electrochim. Acta*, **2017**, 244, 38–46.
5. Ghosh, K. B., Zhang, W., Tassinari, F., Mastai, Y., Lidor-Shalev, O., Naaman, R., Möllers, P., Nürenberg, D., Zacharias, H., Wei, J., Wierzbinski, E., Waldeck, D.H., *J. Phys. Chem. C*, **2019**, 123, 5, 3024–3031.
6. Tomboc, G. M., Choi, S., Kwon, T., Hwang, Y. J., Lee, K., *Adv. Mater.*, **2020**, 32, 1908398.
7. Höskuldsson, Á. B., Tayyebi, E., & Skúlason, E., *J. Catal.*, **2021**, 404, 362-370.
8. Murthy, A. P., Theerthagiri, J., Madhavan, J., *J. Phys. Chem. C*, **2018**, 122, 23943-23949.
9. Shinagawa, T., Garcia-Esparza, A. T., Takanabe, K. (2015). *Sci. Rep.*, **2015**, 5, 13801.
10. Compton, R. G., Banks, C. E., *Understanding Voltammetry*. World Scientific, **2018**.
11. Bard, A.J., Faulkner, L.R., *Electrochemical Methods.* John Wiley & Sons Inc., **2001**.
12. Rheinländer, P. J., Herranz, J., Durst, J., Gasteiger, H. A., *J. Electrochem. Soc.*, **2014**, 161, F1448.
13. Batchelor-McAuley, C., *Curr. Opin. Electrochem.*, **2023**, 37, 101176.
14. Trasatti, S., *J. Electroanal. Chem.*, **1972**, 39, 163.
15. Choudhury, D., Das, R., Tripathi, A. K., Priyadarshani, D., Neergat, M., *Langmuir*, **2022**, 38, 4341-4350.
16. Sarkar, S., Peter, S. C., *Inorg. Chem. Front.*, **2018**, 5, 2060-2080.

## 6.0 Concluding Remarks

This work has explored electron charge and spin transport in chiral systems, with an emphasis on biomolecules and their fundamental relation to chirality. Advancement in the fields of molecular electronics and the applications of the CISS effect are contingent upon the understanding and tractability of charge transport pathways as well as its impact on the electron spin transport. The projects described here have explored the molecular conductance through nucleic acids as a foundation for furthering the field of molecular electronics and also investigated the importance of spin control on charge transport, chemical reactions, and electrochemical reactions involving biomolecules.

Chapter 2 discussed a study of the single molecule conductance of nucleic acids and the impact of introducing a gap, or 'nick', in the backbone structure. The data show that the inclusion of a 'nick' in the nucleic acid backbone results in molecules with similar average conductance to that of non-nicked systems. However, statistical analyses reveal a greater variability in the conductance values when the backbone structure is interrupted. The examination of DNA/PNA heteroduplexes revealed that an increase in the fraction of PNA in the backbone of the heteroduplex resulted in higher conductance values and that the variability in the junction is lower than that for the corresponding homoduplex. Thus we expect that supramolecular assemblies of 'nicked' nucleic acids maintain the conductance of the larger strands, but with a slight increase in variability, suggesting that assemblies of nucleic acids can support complex functions. To realize the goals to which this work builds, future work should explore alternate backbone structures which demonstrate similar Watson-Crick basepair

hybridization but facilitate improved basepair coupling, given the significant improvement in conductivity for PNA (Peptide Nucleic Acid) over the typical DNA backbone.

Chapter 3 expanded on the conductance through nucleic acids by examining the impact of the basepair sequence, specifically, the structure comprising a series of adjacent guanine bases, $G_nC_n$, or 'G-blocks'. It was seen that PNA is ≈30 times higher conductance than the analogous DNA. However, the conductance oscillations with length are diminished, elucidating the interplay between resonant and non-resonant charge carrier transport mechanisms. Theoretical analyses point towards the primary differences in conductance between DNA and PNA duplexes arising from the molecule-electrode interactions and in the strength of the cross-strand coupling. It was concluded that the greater cross-strand coupling in PNA allows for more delocalization across the G-blocks, allowing more pathways for charge transport and consequently higher conductivity. Future work towards increasing the conductance of nucleic acids should explore the effects of nonstandard basepairs on the conductivity of nucleic acids, with a focus on those that display strong π-π stacking and electronic coupling, particularly at the cross-strand. Because the choice of linker group and material-type for the macroscopic electrode was shown to be important, a linker group which facilitates strong electronic coupling to the basepair sequence would be ideal for maximizing the conductivity of nucleic acids as molecular wires. Based on our findings, the macroscopic electrode or wire would ideally have a Fermi level near the HOMO levels of the linker group and basepair sequence, in order to facilitate efficient charge transport.

Chapter 4 presented new data for the chiral induced spin selectivity effect, and incorporated it with the literature to summarize the different phenomena which are known to affect the CISS response. The discrepancies between measurement techniques and nomenclature

were examined and a unified terminology was defined. The impact of length, molecular dipole moment, the molecule-substrate interaction, and the secondary structure on the sign and magnitude of the spin polarization, *SP*, was examined. It was observed that, when referenced to the relative directions of an electron's velocity and its intrinsic angular momentum (spin) vector, the sign of the spin polarization is dependent upon the dipole moment of the molecule as well as the interfacial dipole moment between the molecule and a substrate. Further, the increase in *SP* with respect to length for peptides, and for nucleic acids, persists across experimental techniques, despite different reported values for the asymmetry. Further work to delineate the structure-property relations which engender the CISS effect is also required to realize the dream of CISS-based spintronics. The finding that the magnitude of the spin-filtered current flowing through the entirety of a chiral molecule is significantly different from that where the spin polarization results from charge polarization, with no net current flow, implies that the spin polarization depends on the local geometry of the electric field of the chiral system. Based on this work, the spin polarization due to the CISS response is suspected to be related to the cross product of the electric field setup by a chiral molecule and the charge flowing through it. To test this hypothesis, the correlation of 3D models of the electric field setup by a chiral molecule with empirical measurements of the spin polarization due to the CISS effect should be examined.

Chapter 5 presented ongoing work on the impact of controlling spin in electrochemical reactions, specifically the hydrogen evolution reaction (HER) portion of water electrolysis on different metal catalysts. While the mechanistic pathway for HER was not observed to change upon the introduction of a magnetic field, the data does not preclude the possibility of more subtle effects of spin on the reaction or of other catalysts facilitating a spin dependent reaction pathway.

The work presented in this dissertation has explored the pathways of charge transport as a foundation for molecular electronics utilizing nucleic acid chains. Control of the backbone and of the basepair sequence should facilitate the tailoring of the nucleic acid strands towards desired properties. This work also explored the structure-property relations of the CISS effect in biomolecules. A standardized nomenclature for reporting the orientation and magnitude of the CISS effect was established in order to better facilitate the development of a unified model which can predict not only which properties determine the preferred spin for a given chiral system, but also the magnitude of the spin selectivity exhibited. Finally, the potential applications of spin-controlled electrolysis for controlling water electrolysis pathways were examined with regards to the hydrogen evolution reaction. Progress in molecular electronics and applications of the CISS effect will utilize the foundation established in this dissertation to advance the feasibility of complex molecular circuits and the understanding of the fundamental properties which engender the CISS effect.

# Appendix A Supporting Information for Chapter 2

## Appendix A.1 Nucleic Acid Sequences

The sequences for the nucleic acid oligomers which were studied are listed in Table A.1. Note that a $(CH_2)_3SH$ linker group was used for the strands involved in the conductance measurements to bind the duplexes to the electrodes. The strands used for the fluorescence measurements have pyrene modifications (indicated by "pyr") and these oligomers do not have thiol modifications.

**Table A.1 Sequence of oligonucleotides[a]**

| | **PNA Sequences** |
|---|---|
| **P1** | H-CGTACAAACTTAGACACCAG $Lys_3$-$(CH2)_3SH$ |
| **P2** | H-CTGGTGTCTAAGTTTGTACG $Lys_3$-$(CH2)_3SH$ |
| **P2a**<br>**P2a(p)**<br>**PT-PNA** | H- AGTTTGTACG Lys-$(CH_2)_3SH$<br>H- AGTTTGTACG Lys(pyr)Lys-NH<br>Ac-AGTTTGTACG-$(CH_2)_3SH$ |
| **P2b**<br>**P2b(p)** | H-Lys-CTGGTGTCTA-$NH_2$<br>H-Lys-Lys(pyr)CTGGTGTCTA-$NH_2$ |
| | **DNA Sequences** |
| **D1**<br>**D2** | CGTACAAACTTAGACACCAG-$(CH_2)_3SH$<br>CTGGTGTCTAAGTTTGTACG-$(CH_2)_3SH$ |
| **D1(2p)** | (pyr)CGTACAAACTTAGACACCAG(pyr) |
| **D2a**<br>**D2a(p)**<br>**D2b**<br>**D2b(p)** | AGTTTGTACG-$(CH_2)_3SH$<br>AGTTTGTACG(pyr)<br>CTGGTGTCTA<br>(pyr)CTGGTGTCTA |

a) (p) = one terminal pyrene; (2p) = two terminal pyrenes; PT = propylthiol

## Appendix A.2 Materials and Methods

### Appendix A.2.1 Synthesis of PNA Oligomers

The PNA oligomers were synthesized on 10% *L*-lysine-downloaded MBHA resin (0.45 meq. $NH_2$/g, Peptides International). The oligomers were cleaved from the resin using a mixture containing *m*-cresol/thioanisole/TFA/TFMSA (150/150/900/300 μL per 100 mg of resin). The crude mixture was eluted and precipitated with diethyl ether, dissolved in water, and purified by reversed-phase HPLC using a C18 silica column. All oligomers were characterized by MALDI-ToF mass spectrometry (Table A.2) on an Applied Biosystems Voyager Biospectrometry Workstation using α-cyano-4-hydroxycinnamic acid matrix (10 mg/mL in 1:1 water/acetonitrile, 0.1% TFA).

### Appendix A.2.2 Attachment of Pyrene to the C-End Of PNA

Pyrene can be used as a fluorescent marker that makes it possible to measure the distances between, or within biomolecules. Pyrene can be inserted in PNA oligomers either as part of a PNA monomer, or as a side chain of an amino acid.[1,2] In this study, pyrene was coupled to the side chain of a C- or N-terminal lysine.

Attachment of the pyrene moiety to the C-end of PNA was carried out using a combined Fmoc/Boc strategy. First, the MBHA resin was downloaded with Boc-Lys(2-Cl-Z)-OH, followed by the removal of the Boc group (95% TFA: 5% *m*-cresol) and the addition of Fmoc-Lys(Boc)-OH. Then, the Boc protection of the side-chain was removed (95% TFA: 5% *m*-cresol) and 1-pyreneacetic acid was coupled to the free $NH_2$ group in the presence of HBTU and

DIPEA. After capping with 5% acetic anhydride and 6% lutidine in DMF, the Fmoc group from the N-terminus of lysine was removed using 20% piperidine in DMF; the solid-phase synthesis was continued applying the Boc protection strategy.

### Appendix A.2.3 Attachment of Pyrene to the N-end of PNA

Fmoc-Lys(Boc)-OH was added to the growing oligomer after the last PNA monomer. The Boc group of this terminal lysine was removed using a mixture of 95% TFA : 5% *m*-cresol, followed by the HBTU/DIPEA activated coupling of 1-pyreneacetic acid. Then, the Fmoc group was removed with 20% piperidine in DMF, and the cleavage of the PNA oligomer was carried out using the mixture consisting of *m*-cresol/thioanisole/TFA/TFMSA (150/150/900/300 μL per 100 mg of resin).

**Table A.2 Oligomer Sequences and MALDI MS Data**

| Oligomer | Oligomer sequence N to C | Calc. MW | Obs. MW |
|---|---|---|---|
| P1 | H-CGTACAAACTTAGACACCAG $Lys_3$-$(CH_2)_3SH$ | 5783.55 | 5782.34 |
| P2 | H-CTGGTGTCTAAGTTTGTACG $Lys_3$-$(CH2)_3SH$ | 5858.83 | 5859.84 |
| P2a | H-AGTTTGTACG Lys-$(CH2)_3SH$ | 2885.85 | 2886.86 |
| P2a(p) | H-AGTTTGTACG Lys(*pyr*)Lys-$NH_2$ | 3257.03 | 3257.15 |
| PT-PNA | Ac-AGTTTGTACG-$(CH_2)_3SH$ | 2874.67 | 2875.25 |
| P2b | H-Lys-CTGGTGTCTA-$NH_2$ | 2861.83 | 2861.13 |
| P2b(p) | H-Lys Lys(*pyr*) CTGGTGTCTA-$NH_2$ | 3233.29 | 3233.14 |

### Appendix A.2.4 Thermal Stability

UV melting curves were recorded in the temperature range 5°C to 95°C. The rate of both cooling and heating was 1°C/min. Prior to the measurement of the melting profiles, the solutions

were kept at 95°C for 20 min. The melting temperature, $T_m$, was taken at the inflection point of the Boltzmann sigmoidal fit function, which assumes a two-state model.

**Table A.3 Summary of Thermal Stabilities for DNA/DNA and PNA/PNA Homo-duplexes($T_m$[°C]), and DNA/PNA Hetero-duplexes($T_m$[°C])**

| Homo-DNA duplex | $T_m$[°C] | Homo-PNA/PNA Duplex | $T_m$[°C] | Hetero- DNA/PNA Duplex | $T_m$[°C] |
|---|---|---|---|---|---|
| D1(2p)D2a(p)D2b(p) | 30 | P1P2 | >90 | P1P2aD2b | 68 |
| D1(2p)D2a(p) | 25 | | | D1(2p)P2a(p)P2b(p) | 66 |
| D1(2p)D2b(p) | 31 | | | D1(2p)P2a(gRH)P2b(p) | 73 |
| | | | | D1(2p)P2a(p) | 65 |
| | | | | D1(2p)P2b(p) | 66 |

$T_m$ are known within 2°C. $T_m$ were obtained from the curve-fitting data or estimated from the first derivative of the melting curves. The $T_m$ values are an average of at least two experiments.

Figure A.1 shows melting curves for the full and nicked versions of the DNA/DNA and DNA/PNA duplexes. The effect of the nick is demonstrated by a shift in the melting temperature to smaller values for the nicked versions of the duplexes.

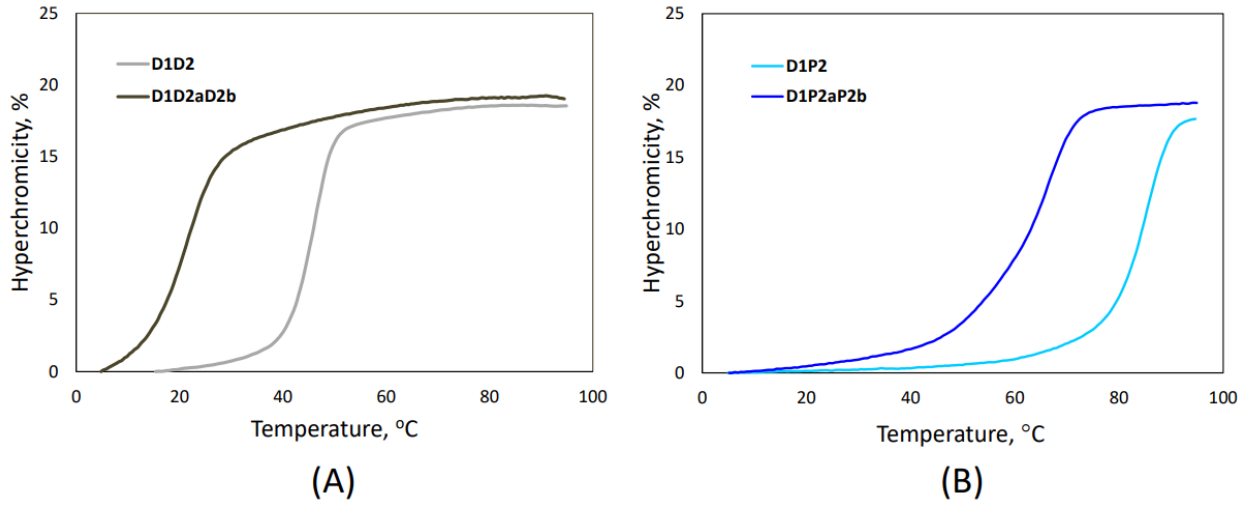


**Figure A.1 (A) The melting curves for the full DNA and nicked DNA. (B) The melting curves for the full DNA/PNA and nicked DNA/PNA.**

## Appendix A.3 Chirality of the nicked homo-and heteroduplexes

The handedness of the nicked PNA/PNA:DNA and DNA duplexes was determined by circular dichroism (CD) spectroscopy. Figure A.2 shows the CD spectra for both duplexes. While the spectra show exciton coupling patterns consistent with literature findings for DNA and DNA/PNA duplexes,[5] the CD responses are markedly different for the nicked nucleic acid duplexes. The spectrum for the PNA/PNA:DNA heteroduplex has an additional point of inflection compared to the spectrum for the nicked DNA duplex, resulting in an additional negative peak in the spectrum at ~ 290 nm.

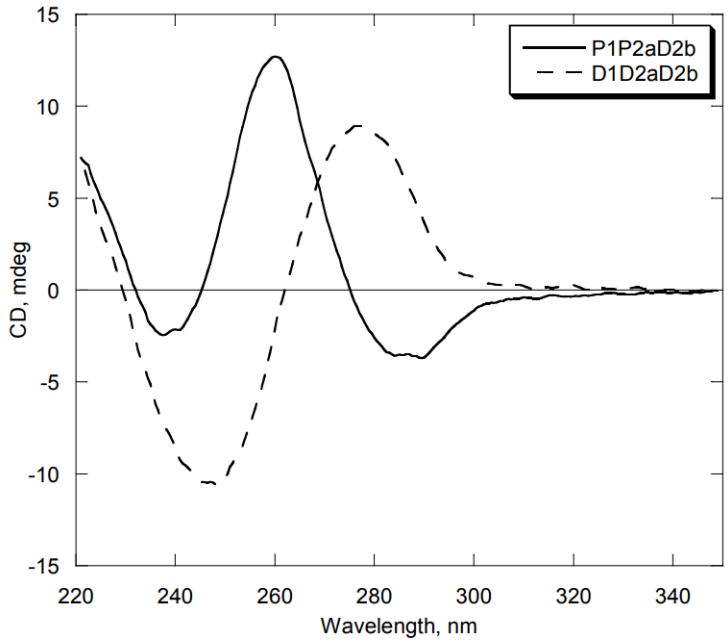


**Figure A.2 CD spectra of nicked PNA/PNA:DNA and DNA duplexes. Samples containing stoichiometric amounts of oligonucleotides at 3 µM strand concentration were prepared in 10 mM sodium phosphate buffer.**

## Appendix A.4 Fluorescence Studies

Excitation and emission spectra were obtained using a Cary Eclipse fluorimeter. Emission spectra were recorded with 0.2 ms delay time and 5 ms gate time in the range 350-600 nm with selective irradiation at 345 nm ($\lambda_{ex}$= 345 nm).

## Appendix A.5 Conductance Measurements

### Appendix A.5.1 Equipment

All conductance measurements were performed using an Agilent 5500 Scanning Probe Microscope system with a Stanford Research Systems DS345 function generator. Experiments were performed in an environmental chamber housed in an acoustically isolated Faraday cage. The Faraday cage was mounted on an anti-vibrational table (Table Stable). The current was collected using a 10 nA/V preamplifier.

### Appendix A.5.2 Nucleic Acid Duplexes

DNA oligomers were purchased from Integrated DNA Technologies and the PNA strands were synthesized following procedures detailed above. Hybridization of the strands was achieved by heating solutions containing 20 μM of each nucleic acid strand in pH=7.0 Tris-EDTA buffer to 95°C for 10 minutes and allowing them to cool to room temperature over several hours. The characterization of the nicked duplexes was performed as detailed above.

### Appendix A.5.3 Substrate Fabrication

The gold substrates were fabricated using the template-stripping technique.[6] A 100 nm Au film was evaporated onto freshly-cleaved mica sheets using an AJA ATC-T Series Thermal Evaporation System. Glass slips (10 mm x 25 mm) were cleaned in a piranha solution and affixed to the gold surface using an epoxy resin (Epo-Tek). Prior to each experiment, a glass slip was peeled from the mica sheet, and the gold film was transferred to the glass slip.

### Appendix A.5.4 Substrate Preparation

50 μL of the hybridized nucleic acid solution was deposited on the gold surface for 10 seconds to allow for a diffuse monolayer to form via the thiol linkers. The substrates were then washed with water, washed with ethanol, and dried under a stream of inert gas.

### Appendix A.5.5 Conductance Measurements

All conductance measurements were performed using freshly cut gold wire (0.25 mm, 99.95%, Alfa Aesar). The prepared substrates were immersed in a mesitylene solution in an inert atmosphere. The current-distance characteristics were monitored between 0.09 nA and 100 nA with current below 0.09 nA attributed to the solvent and removed.

## Appendix A.5.6 Data Analysis

Thousands of current-distance trajectories were collected for each duplex. Data sets were manually filtered to remove trajectories without molecular junctions. The procedure for fitting the trajectories is detailed in Reference 7 The resulting conductance histograms were fit using Gaussian functions, as shown in Figure A.3.

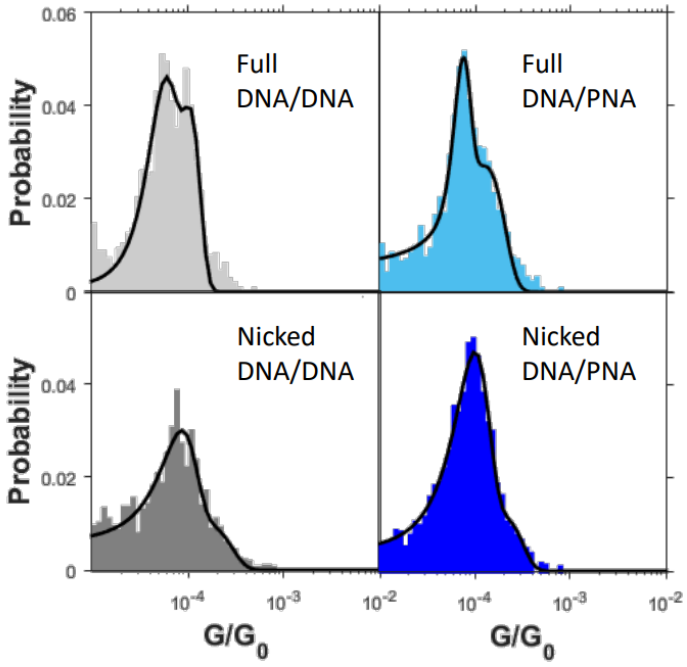


**Figure A.3 The conductance histograms for the full and nicked versions of the DNA/DNA and DNA/PNA duplexes. The Gaussian fits are shown as overlaid black curves.**

## Appendix A.5.7 Thiol Location Control

To exclude any effect of the thiol location on a backbone in the nicked PNA/PNA:DNA heteroduplex, a control was performed in which the nicked PNA/PNA:DNA heteroduplex was measured with the thiol linker on the DNA 10-mer rather than on the PNA 10-mer. In these duplexes, the base stack remains composed of the same strands; however, the identity of the

strand with the second thiol linker is DNA in one case and PNA in the other. Conductance histograms are shown in Figure A.4 for both nicked heteroduplexes.

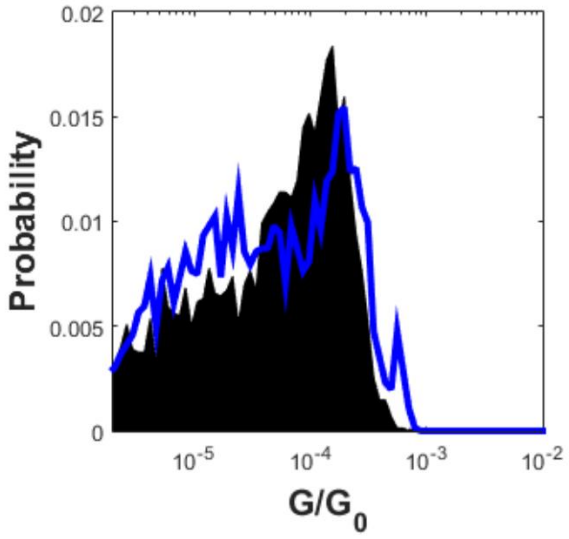


**Figure A.4 Conductance histograms for the nicked PNA/PNA:DNA heteroduplex with the thiol linker on the DNA 10-mer (black), and with the thiol linker on the PNA 10-mer (blue).**

The results of this control experiment showed equivalent high-mode conductances for both duplexes. This suggests that the location of the thiol, whether on a DNA strand or a PNA strand, does not affect the molecular conductance. This supports the conclusion that charge moves through the base stack, as the base stack composition is the same for both duplexes.[8]

### Appendix A.5.8 Serial Correlation

In an attempt to distinguish the behavior of the molecular junctions for each duplex, serial correlation analyses were employed for the conductance measurements.[9] The serial correlation is defined as:

$$r_k = \frac{\frac{1}{N-1}\sum_{n=1}^{N-k}(G_n - \overline{G})(G_{n+k} - \overline{G})}{c_0} \qquad \textbf{Equation A.1}$$

where $n$ and $k$ index periods in the trajectory, $G$ is the conductance for a given period, $\bar{G}$ is the average conductance, and $c_0$ is the variance of the conductance of the trajectory.

Correlation analyses utilizing the STM-BJ technique display a rapid decay as the movement of the STM tip drives an eventual breakdown of the junction.[10-12] The calculated serial correlation values are indistinguishable between the duplexes because of the rapid loss of correlation. This behavior is attributed to the multiple conductance modes that are probed in the frozen junction technique.[13,14] Therefore, a statistical analysis of the conductance value fitted for each current response period was performed to compare the full duplexes to their nicked analogues for stabilized molecular junctions.[15] Utilizing custom Matlab scripts, periods of the current response that have a current greater than the solvent threshold are assumed to arise from molecular junctions and are separated from the full current-time, I(t), trajectory (see Figure A.5). The set of periods containing molecular junctions was concatenated for correlation analysis.

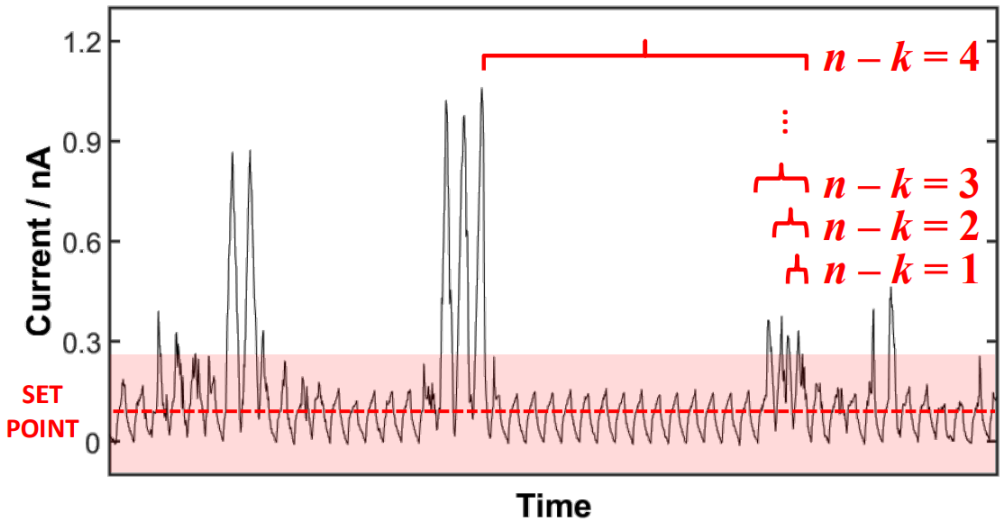


**Figure A.5 A current-time, I(t), trajectory showing the method of solvent removal and period concatenation. The set-point of the conductance measurements is shown as a red, dashed line. The red, shaded region depicts the periods of the current response that are within the solvent threshold and are filtered out of the correlation analysis.**

The serial correlation (the correlation of the conductance in the n$^{th}$ period of a trajectory with that in the $(n - k)^{th}$ period) is calculated for the full and nicked duplexes and shown in Figure A.6 for the frozen junction technique. Despite creating stabilized molecular junctions, serial correlation analyses did not show distinguishable decay characteristics between the set of duplexes. Correlation analyses were subsequently directed to the initial periods of the STM-BJ measurements to ensure a comparison within a similar range of current values (see Figure 2.5).

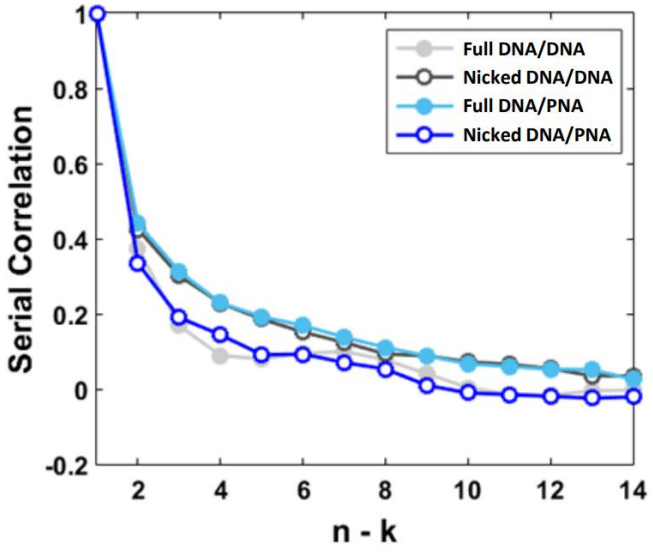


**Figure A.6 Serial correlation is shown for the full and nicked versions of the DNA/DNA and DNA/PNA duplexes using the 'frozen junction' method.**

## Appendix A.5.9 DNA Conductance Comparison

The conductance data presented in Figure A.7 are shown versus the total number of base pairs. Inclusion of the G/C base pairs in the length count eliminates the exponential dependence demonstrated in Figure 2.7, in which only the number of A/T pairs are used as a metric for the tunneling length.

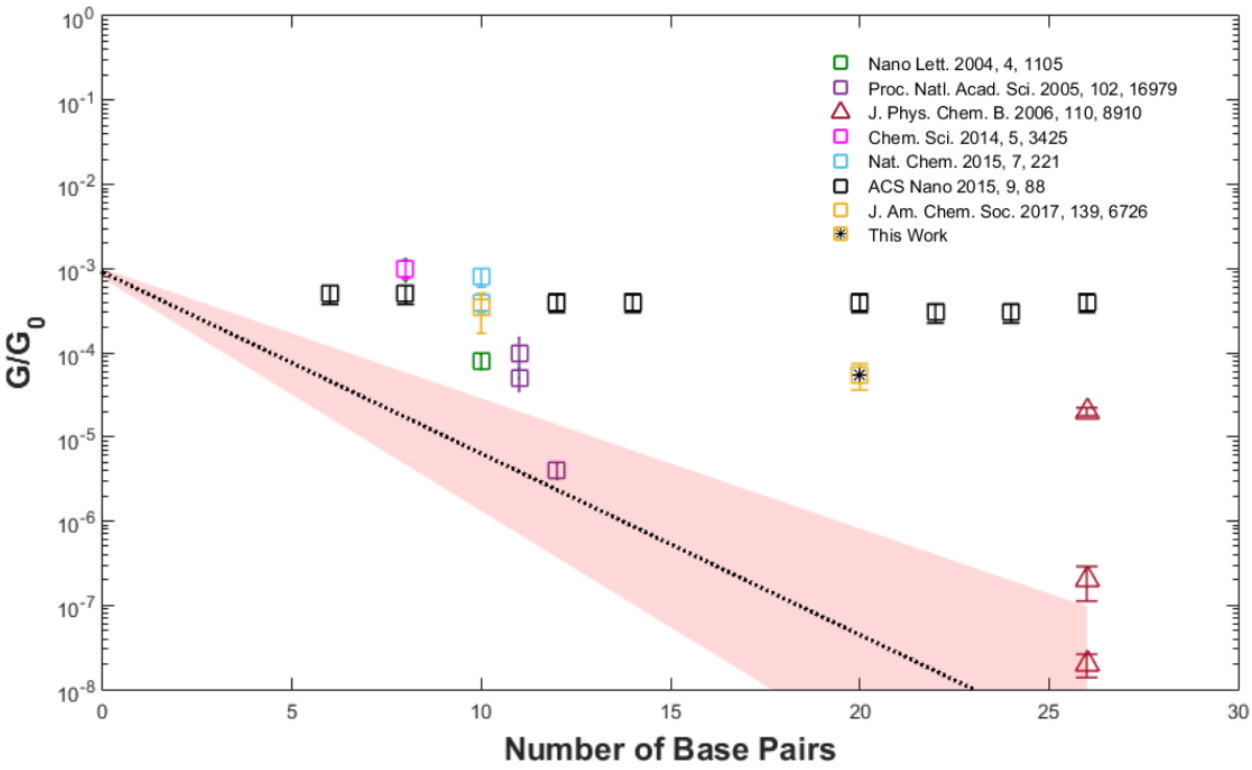


**Figure A.7 Conductance values for DNA duplexes as a function of the total number of base pairs of the duplex measured by various methods. In the conductance measurements, the DNA was attached to the surface by three-carbon (C3) thiol linkers. Squares identify the conductance measured by the scanning tunneling microscope break junction method. Triangles identify values measured by atomic force microscopy conductance utilizing a gold nanoparticle. The dashed line indicates the best fit function shown in Figure 2.7; and the shaded region shows a 95% confidence interval for the best fit.**

## Appendix A.6 References


1. Manicardi, A. G., L.; Ghidini, A.; Corradini, R., *Beilstein J. Org. Chem.* **2014**, 10, 1495-1503.
2. Sacui, I.; Hsieh, W.-C.; Manna, A.; Sahu, B.; Ly, D. H., *J. Am. Chem. Soc.* **2015**, *137*, 8603-8610.
3. Beall, E.; Ulku, S.; Liu, C.; Wierzbinski, E.; Zhang, Y.; Bae, Y.; Zhang, P.; Achim, C.; Beratan, D. N.; Waldeck, D. H., *J. Am. Chem. Soc.* **2017**, 139, 6726-6735.
4. Yeh, J. I.; Shivachev, B.; Rapireddy, S.; Crawford, M. J.; Gil, R. R.; Du, S.; Madrid, M.; Ly, D. H., *J. Am. Chem. Soc.* **2010**, 132, 10717-10727.
5. Berova, N.; Polavarapu, P. L.; Nakanishi, K.; Woody, R.W., Eds.; *Comprehensive Chiroptical Spectroscopy: Applications in Stereochemical Analysis of Synthetic Compounds, Natural Products, and Biomolecules*, John Wiley & Sons, **2012**.
6. Hegner, M.; Wagner, P.; Semenza, G., *Surf. Sci.* **1993**, 291, 39-46.
7. Beall, E.; Yin, X.; Waldeck, D. H.; Wierzbinski, E., *Nanoscale* **2015**, 7, 14965-14973.
8. Liu, T.; Barton, J. K., *J. Am. Chem. Soc.* **2005**, 127, 10160-10161.
9. Dunn, P. F., *Measurement and Data Analysis for Engineering and Science*; McGraw-Hill: New York, **2005**.
10. Park, Y. S.; Whalley, A. C.; Kamenetska, M.; Steigerwald, M. L.; Hybertsen, M. S.; Nuckolls, C.; Venkataraman, L., *J. Am. Chem. Soc.* **2007**, 129, 15768-15769.
11. Zhou, J.; Chen, F.; Xu, B., *J. Am. Chem. Soc.* **2009**, 131, 10439-10446.
12. Bruot, C.; Xiang, L.; Palma, J. L.; Tao, N., *ACS Nano*, **2015**, 9, 88-94.
13. Li, C.; Pobelov, I.; Wandlowski, T.; Bagrets, A.; Arnold, A.; Evers, F., *J. Am. Chem. Soc.* **2008**, 130, 318-326.
14. Haiss, W.; Martín, S.; Leary, E.; Zalinge, H. v.; Higgins, S. J.; Bouffier, L.; Nichols, R. J., *J. Phys. Chem. C*, **2009**, 113, 5823-5833.
15. Zhou, J.; Chen, G.; Xu, B., *J. Phys. Chem. C*, **2010**, 114, 8587-8592.

# Appendix B Supporting Information for Chapter 3

## Appendix B.1 Sample Preparation

### Appendix B.1.1 PNA Synthesis

The PNA materials prepared were N-to-C: (Dap-T)$G_nC_nA$ for n = 3-7; and $AC_nG_n$(Dap-T) n = 3.

All reagents were purchased from commercial suppliers and used as received. Boc/Z and Fmoc/Bhoc PNA monomers were purchased from PolyOrg Inc. and ASM Research Chemicals and used without further purification. The acetic acid form of the thymine 5-C2 amino linker (T($C_2$-$NH_2$) acetic acid) was synthesized using a modified published procedure described in Reference 1. The thymine 5-C2 amino linker was connected to the PNA oligomer through 2,3-diaminopropionic acid (DAP); the T($C_2$-$NH_2$) acetic acid was coupled to the side chain of the Dap. We used Boc-Dap(Fmoc)-OH (Sigma-Aldrich) at the N-end of the PNA and Fmoc-Dap(Mtt)-OH (Acrotein ChemBio) at the C-end. The PNA oligomers were prepared by solid phase synthesis using standard Fmoc procedures.[2] The PNAs that contained the T linker at the N-end were synthesized as described in Reference 1.

The PNA $AC_3G_3$(Dap-T) that contained the T linker at the C-end was synthesized on Rink-Amide MBHA Resin (200-400 mesh, 0.3 milli-equivalent/g) acquired from Chem-Impex. The synthesis began with downloading the resin with Fmoc-Dap(Mtt)-OH, followed by the

deprotection of the Mtt group using DCM/TFA/TIS 94:1:5 (v/v) 3x10 minutes and by coupling of the thymine 5-C2 linker. The synthesis continued with the addition of the G, C, and A monomers. The PNA oligomer $AC_3G_3$(Dap-T) was cleaved from the resin using TFA/DCM/triisopropylsilane (10:85:5) for 30 min. Attempts to synthesize by the same procedure PNAs ACnGn(Dap-T) where n = 4-7 were unsuccessful. An attempt to attach the T linker to DAP after the G, C, and A monomers were coupled was also unsuccessful.

PNA strands were purified by reverse-phase HPLC using a C18 column (5 μm; 19 × 100 mm; Waters Corporation, Milford, MA) and were subsequently lyophilized for long-term storage. Characterization of the oligomers was performed by MALDI-TOF on an Applied Biosystems Voyager Biospectrometry Workstation using R-cyano-4-hydroxycinnamic acid matrix (10 mg/mL in 1:1 water/acetonitrile, 0.1% TFA). The purified PNAs were dissolved in nano-pure water and used in the preparation of surfaces for STM-BJ.

C-end T linker*
$AC_3G_3$(Dap-T) m/z[M+H]+ calcd/obsvd 2270/2270
N-end T linker*
(Dap-T)C3G3-A m/z[M+H]+ calcd/obsvd 2270/2271
(Dap-T)C4G4-A m/z[M+H]+ calcd/obsvd 2812/2813
(Dap-T)C6G6-A m/z[M+H]+ calcd/obsvd 3897/3896
(Dap-T)C7G7-A m/z[M+H]+ calcd/obsvd 4439/4430
Sequences are written N-to-C

We could not measure melting temperatures of the reported duplexes by UV spectroscopy. Changes in absorbance at 260 nm for solutions of $G_3C_3$ PNA duplexes were very small and non-sigmoidal, which is attributed to the high stability of GC-rich nucleic acid duplexes. The stability would be even higher for longer G-block duplexes.

### Appendix B.1.2 DNA Duplexes

DNA duplexes were purchased from Alpha DNA. The lyophilized DNA material was used to create 100 µM stock solutions in pH 8.0 Tris-EDTA buffer (Sigma-Aldrich). The stock solutions were stored in a freezer and thawed prior to hybridization.

### Appendix B.1.3 Hybridization

Hybridization involved diluting the stock solutions with pH 8.0 Tris-EDTA buffer containing 50 mM NaCl until the concentration of oligomer was 40 µM. The 40 µM solutions were heated to 95°C and allowed to slowly cool to room temperature over the course of several hours. Because the oligomers are self-complementary, the final concentration of hybridized duplex was 20 µM.

## Appendix B.2 Conductance Measurements

### Appendix B.2.1 Substrate Preparation

The Au films were 100 nm in thickness and were prepared by evaporation onto freshly cleaved mica using an AJA ATC-T Series Thermal Evaporation System. Piranha-cleaned glass slips (10 mm × 22 mm) were affixed to the gold films by epoxy (EPO-TEK 302-3M). Prior to each experiment, a glass slip was peeled from the mica surface, transferring the gold film to the glass.[3] 50 µL of 20 µM PNA (or DNA) duplex solutions in a Tris/EDTA buffer were deposited

on the gold substrates and allowed to form a diffuse monolayer under a water saturated atmosphere for 30 min. The substrates were subsequently rinsed with deionized water, then rinsed with ethanol, and dried under an argon stream.

### Appendix B.2.2 Conductance Measurements

The conductance measurements were performed in an Agilent 5500 scanning probe microscope system using a PicoView interface. The PNA coated substrates were immersed in 800 μL of mesitylene (Extra-pure, 99%, Acros Organics). Gold STM tips (0.25 mm, 99.95%, Alfa Aesar) were freshly cut prior to each experiment. The experimental cell was maintained under a positive pressure of argon and contained within an environmental chamber. The environmental chamber was housed in a custom-made Faraday cage that was located on an anti-vibration platform (Table Stable). For most experiments, a 50 ± 50 mV triangle waveform was applied across the tip-substrate gap at a modulation frequency of 500 Hz (DS345 Function Generator, Stanford Research Systems). Currents in the range of 5-1000 nA were sampled using a 100 nA/V preamplifier. The withdraw speed of the STM tip was 10 nm/sec in order to balance the duration and stability of the molecular junctions.

### Appendix B.2.3 Data Analysis

Conductance data were analyzed following reported procedures utilizing a custom MATLAB script.[4] Currents below 5 nA were excluded from the analysis. Only the current traces that showed a clean break in the surface-tip conductance (indicated by a strong, precipitous drop in conductance with retraction distance), and were followed by at least 4 voltage

modulation periods at a similar current level. Current-time trajectories that did not display molecular junctions were removed. Only about 3% of traces were judged analyzable by these criteria. The collection and removal of background counts are detailed below.

## Appendix B.3 STM-BJ Background and Control Experiments

To ensure that the histograms created for the PNA duplexes can be attributed to PNA molecular junctions, conductance measurements on the PNA assemblies were compared to those that were performed on Au substrates for which the PNA incubation step was excluded. All other procedural steps were followed as described. The number of experiments (i.e., STM tip approach and subsequent withdraw from the surface) performed for the PNA coated surface and the bare Au surface in this control study was the same. The results of the control study are shown in Figure B.1. The histogram shown on the left is an unmodified histogram built from the total counts observed for the $n = 5$ N-to-N linker PNA duplex, as an example. The histogram shown on the right is the background histogram corresponding to the Au surface with no PNA. To generate the histograms shown in Figure 3.3, the total counts for the background were subtracted from the unmodified histograms.

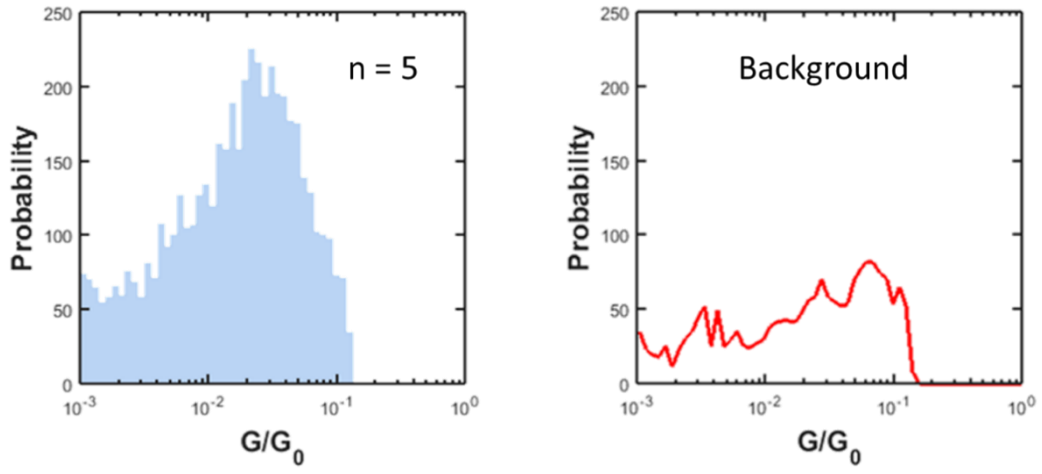


**Figure B.1 The results of the control study are shown for the PNA coated surface (left) and the bare Au surface (right). Although the number of STM tip cycles with the surface is the same for each dataset, the number of modulation periods is considerably less for the bare Au surface than those found for the surfaces with PNA duplexes.**

In an attempt to determine the origin of the current responses observed on the bare Au surfaces (i.e., no PNA present), a substrate was electrochemically oxidized (1.5 V, 60 s) and measured alongside a substrate that did not undergo electrochemical oxidation. A comparison is shown Figure B.2. The unmodified surface shows significantly fewer modulation periods than the oxidized surface. While the origin of the modulation periods observed in the control experiments with a bare Au surface cannot be concluded to arise solely from gold oxidation, oxidizing the gold substrate surface results in many more 'background' current responses, implying that Au oxide is a likely contributor to the background signal.

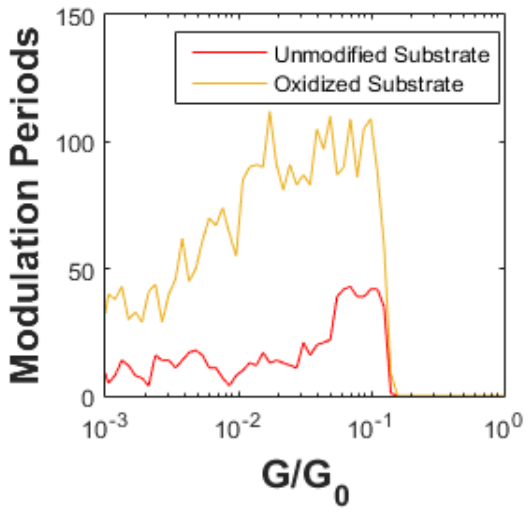


**Figure B.2 A comparison of the modulation periods observed for an unmodified substrate and a substrate that has undergone electrochemical oxidation. An equivalent number of trajectories was collected for both substrates.**

The histograms shown in Figure 3.3, display a bimodal character. The presence of different 'modes' in the conductance population of thiol linked molecules to Au surfaces is well known.[5] There exist different conductance modes, based primarily on the arrangement of the linker amine groups with gold atoms on the STM tip and the other end of the molecule with the substrate. When the linker group is in contact with multiple gold atoms, a higher conductance is expected than if it contacts only one Au atom. As the tip retracts, only a single gold atom maintains contact, and a lower conductance value should be observed.

## Appendix B.4 Low Conductance Mode for PNA

The fits to the histograms in Figure 3.3 also provided conductance values for the lower conductance modes of the G-block PNA duplexes, and these are reported in Table B.1. The

lower conductance mode is a factor of three to five smaller than that found for the higher conductance mode.

**Table B.1 The average conductance of the lower conductance mode, $G$, and the standard deviation, $\sigma_G$, from the Gaussian fits are shown for the N-linker PNA duplexes for lengths $n = 3 - 7$.**

| $n$ | $G/G_0$ $(\times 10^{-2})$ | $\sigma_G/G_0$ $(\times 10^{-2})$ |
|---|---|---|
| 3 | 1.5 | 1.1 |
| 4 | 1.4 | 1.1 |
| 5 | 1.6 | 0.9 |
| 6 | 0.6 | 0.2 |
| 7 | 0.6 | 0.4 |

In order to compare the lower conductance mode of the PNA with the other conductance data, Figure B.3 shows a plot of the lower conductance PNA data (green triangles) on a graph with the high conductance mode PNA data (blue squares), the 3'-linker DNA(black triangles), and the 5'-linker DNA (red circles). Note that the lower conductance mode for the PNA G-block duplexes has a significantly higher conductance than the DNA G-block duplexes.

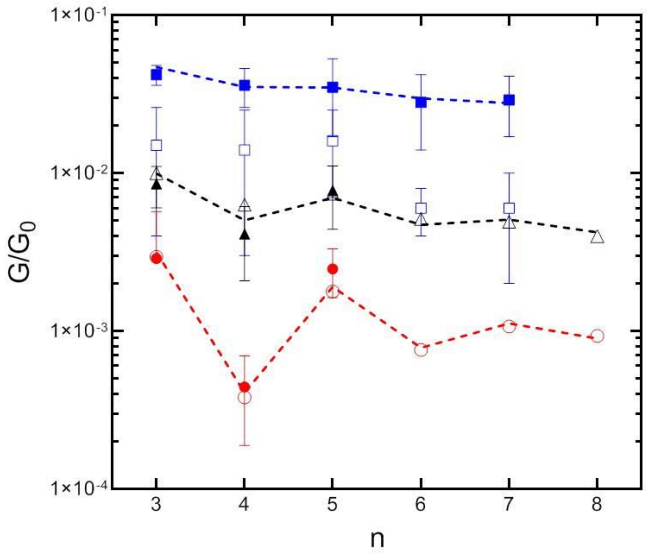


**Figure B.3 The conductance values found for the lower conductance mode of the N-linker PNA (open blue squares) are shown in relation to the high conductance modes plotted in Figure 3.4. The high conductance mode for the N-linker PNA (solid blue squares) as well as for the high conductance mode of 5'-linker DNA (red circles) and 3'-linker DNA (black triangles) are reproduced from Figure 3.4.**

## Appendix B.5 DNA Conductance Measurements

The molecular conductance histograms that were obtained for 3'-linked and 5'-linked G-block DNA duplexes of lengths $n = 3$ to $n = 5$ are shown in Figure B.4. The full range of conductance data recorded is included in the histograms, any differences in the ranges of the conductance values are the result of the molecules themselves. The average conductance values that were extracted from these data are in good agreement with the average conductance values that were reported by Liu and coworkers.[6] The average conductances obtained from these histograms are plotted in Figure 3.4 of the main text and reported in Table B.2.

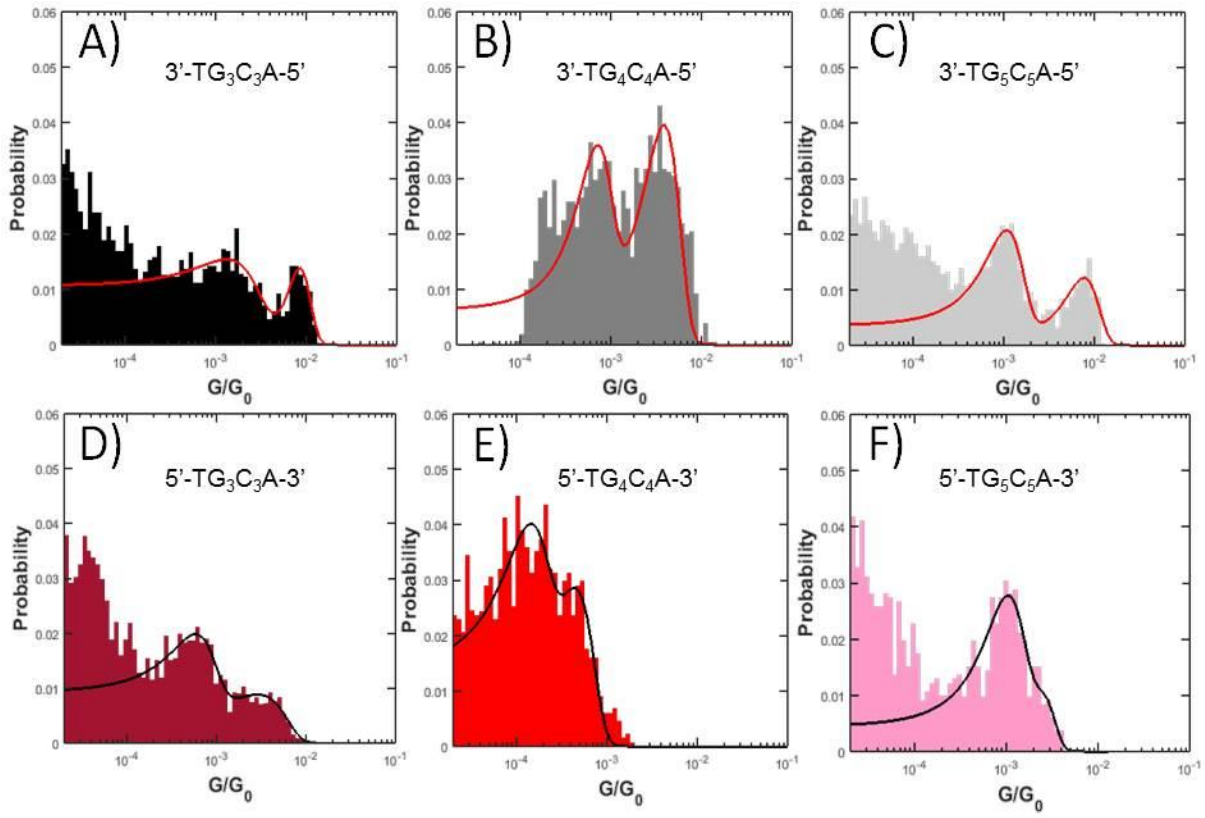


**Figure B.4 Conductance histograms are shown for 3'-linked and 5'-linked G-block DNA duplexes for lengths $n = 3$ to $n = 5$. For the 3'-linked duplexes (A-C), the histograms are shown as shades of black and each histogram is fit with a sum of two Gaussian functions, shown as a red overlay. For the 5'-linked duplexes (D-F), the histograms are shown as shades of red and the Gaussian fit is shown in black.**

**Table B.2 The average conductance of the highest observable mode, $G$, and the standard deviation, $\sigma_G$, from the Gaussian fits are shown for the 5'- and 3'-linker DNA duplexes for lengths $n = 3 - 5$.**

| $n$ | 5'-linker $G/G_0$ ($\times 10^{-2}$) | 5'-linker $\sigma_G/G_0$ ($\times 10^{-2}$) | 3'-linker $G/G_0$ ($\times 10^{-2}$) | 3'-linker $\sigma_G/G_0$ ($\times 10^{-2}$) |
|---|---|---|---|---|
| **3** | 0.29 | 0.28 | 0.85 | 0.25 |
| **4** | 0.044 | 0.025 | 0.41 | 0.20 |
| **5** | 0.25 | 0.08 | 0.77 | 0.33 |

## Appendix B.6 Classical Molecular Dynamics

### Appendix B.6.1 Molecular Dynamics Procedure

The nucleic acid duplexes were solvated in a TIP3P water box[7] that extended at least 15.0 Å from each atom. DNA duplexes were neutralized with $Na^+$ ions. CHARMM36 force field parameters for DNA[8] and PNA[9] were used. The scaling factor for 1-4 electrostatic interactions was set to 1.00. A distance of 12 Å was selected for truncating van der Waals interactions. The maximum non-bonded interaction distance for the periodic calculation of the interaction energy was set to 14 Å. The Particle Mesh Ewald method[10] with a grid spacing of 1 Å was used to compute the electrostatic interactions. Full electrostatic interaction energies were evaluated every 2 time steps. The lengths of all chemical bonds between hydrogens and heavy atoms were constrained. The unit cell vectors were (in Å): (74, 54, 54) for DNA 5', (74, 54, 54) for DNA 3', and (62, 80, 58) for PNA N-end.

The NAMD 2.11 software[11] was used to run the MD simulations. First the duplexes were optimized with $8x10^4$ energy minimization steps. The minimization was followed by 225 ps of solvent equilibration (fixed nucleic acid duplex) at 300 K to allow water molecules and ions to adjust. Next, the constraints were removed, and a Langevin thermostat and piston[12,13] were used to equilibrate the systems at constant temperature and pressure for 1.5 ns (temperature = 300 K, pressure = 1 bar, barostat period = 100 fs, characteristic damping time = 50 fs, damping coefficient = 2.0 $ps^{-1}$). The final MD production run lasted 100 ns. Snapshots were saved for each system every 33 ps (3000 coordinate frames in total).

## Appendix B.6.2 Analysis of MD structural ensembles

Figure B.5 shows the root-mean-square deviation (RMSD) maps for the nucleic acid duplexes generated using MDAnalysis.[14,15] Each frame is compared and color-coded according to the RMSD. Both DNA structures have somewhat higher RMSD values than PNA, in contrast to previous studies.[16] Figure B.6 includes the percent change in flexibility, $\Delta\sigma$, of helical parameters related to nucleic acid flexibility (rise, roll, shift, slide, tilt, twist). $\Delta\sigma = {\sigma_r - \sigma_d}/{\sigma_r} \cdot 100$, where $\sigma_r$ is the standard deviation of the reference (DNA 5') and $\sigma_d$ is the standard deviation of the nucleic acid duplex (DNA 3' or PNA N-end). Negative values show a decrease in flexibility.

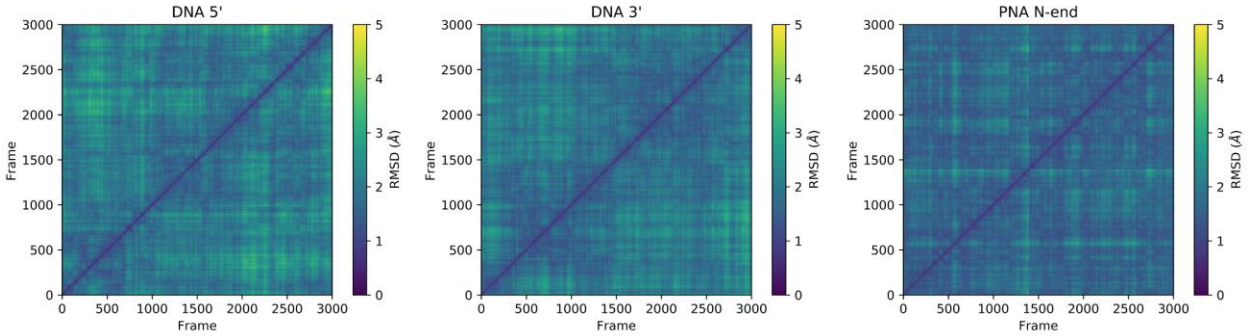


**Figure B.5 RMSD maps for the MD production simulations of the nucleic acid duplexes.**

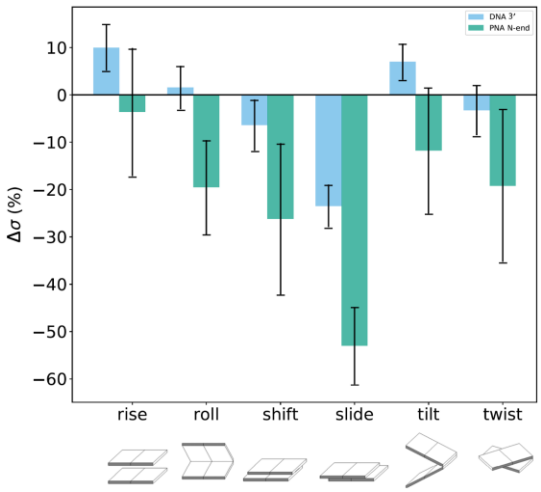


**Figure B.6 Comparisons between the standard deviations of several parameters between duplexes (using 5' DNA as the reference). All base pairs were considered. Structural parameters are defined and calculated with the 3DNA software package.[17]**

## Appendix B.6.3 HOMO Energies

Table B.3 shows the HOMO energies and standard deviations of all of the base pairs of the $n = 5$ duplexes.

**Table B.3 HOMO energies and standard deviations ($\sigma$) in eV for each base pair of the $n = 5$ duplexes.**

| Base Pair | DNA 5' | | DNA 3' | | PNA N-end | |
|---|---|---|---|---|---|---|
| | $E_{HOMO}$ | σ | $E_{HOMO}$ | σ | $E_{HOMO}$ | σ |
| **A1-T1** | 7.45 | 0.21 | 7.57 | 0.23 | 7.39 | 0.19 |
| **G1-C1** | 6.61 | 0.23 | 6.73 | 0.22 | 6.56 | 0.18 |
| **G2-C2** | 6.45 | 0.22 | 6.43 | 0.21 | 6.45 | 0.19 |
| **G3-C3** | 6.31 | 0.19 | 6.34 | 0.19 | 6.49 | 0.17 |
| **G4-C4** | 6.31 | 0.20 | 6.38 | 0.21 | 6.70 | 0.18 |
| **G5-C5** | 6.56 | 0.22 | 6.52 | 0.20 | 6.99 | 0.19 |
| **G6-C6** | 6.55 | 0.23 | 6.56 | 0.21 | 6.97 | 0.19 |
| **G7-C7** | 6.34 | 0.22 | 6.52 | 0.21 | 6.70 | 0.19 |
| **G8-C8** | 6.40 | 0.20 | 6.41 | 0.22 | 6.51 | 0.18 |
| **G9-C9** | 6.48 | 0.21 | 6.47 | 0.21 | 6.43 | 0.17 |

| | | | | | | |
|---|---|---|---|---|---|---|
| **G10-C10** | 6.68 | 0.21 | 6.62 | 0.22 | 6.51 | 0.18 |
| **A2-T2** | 7.54 | 0.20 | 7.44 | 0.22 | 7.31 | 0.17 |

## Appendix B.6.4 Average Structures

The average structures over the 3000 coordinate snapshots for each duplex were obtained from VMD.[18] Figure B.7 shows the average structures of the duplexes and Figure B.8 shows the four nucleotides at the cross-strand section. The RMSDs of the four nucleobases at the cross-strand section are in Figure B.9 and the calculated electronic couplings for the average structures are in Table B.4. The base pair electronic couplings are consistent with previous results.[19]

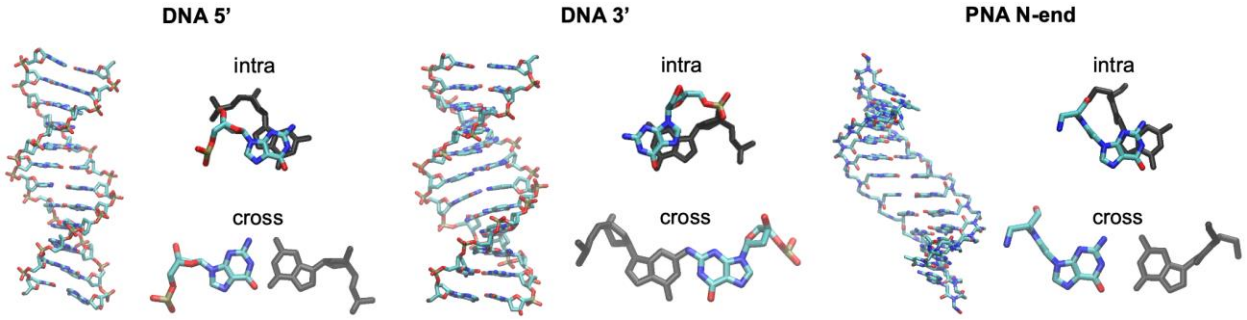


**Figure B.7 Average structures from the 3000 MD snapshots. The intra-strand and cross-strand G-G overlaps are shown for each duplex.**

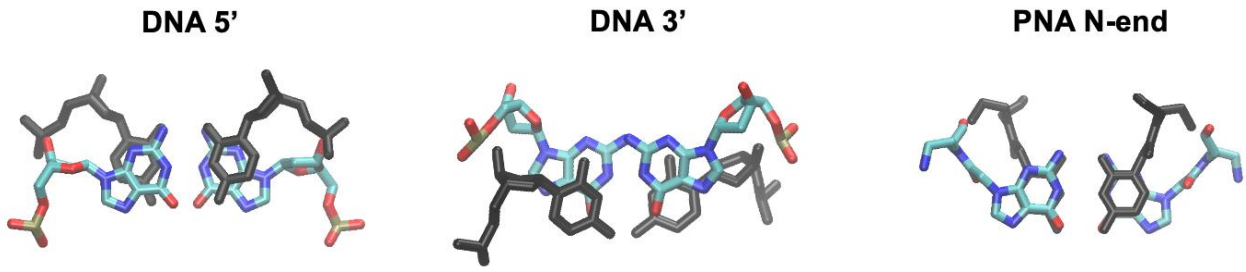


**Figure B.8 Average structures from the 3000 MD snapshots for the four nucleobases at the cross-strand section.**

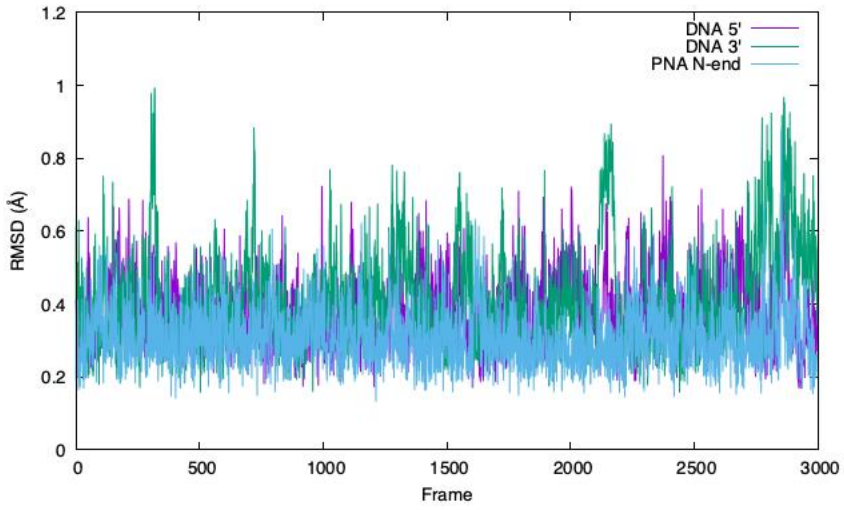


**Figure B.9 RMSDs (excluding H atoms) from its average structure along the MD production runs for the four nucleobases at the cross-strand section.**

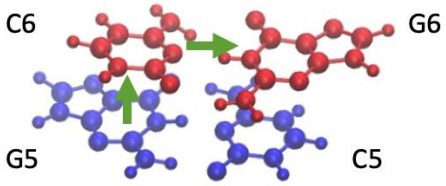


**Figure B.10 Nucleobase labeling for the calculation of $V_C^{SE}$.**

**Table B.4 $V_{RMS}$ values of the electronic couplings in eV of the four nucleotides at the cross-strand section (Figure B.10) calculated at the M11/ma-def2TZVPP level of theory[20,21] using single snapshots taken every 5 ns. The superexchange cross-strand coupling, $V_C^{SE} = {V_{G5-C6}V_{G6-C6}}/{\Delta E}$. $\Delta E$ is approx. 0.7 eV[22,23] The $V_C^{SE}$ value calculated with the alternative pathway ($V_{G5-C5}V_{C5-G6}$) gives similar results. (i.e. $V_{G5-C6} \approx V_{C5-G6}$ and $V_{C6-C6} \approx V_{G5-C5}$)**

| DNA 5' | | | DNA 3' | | | PNA N-end | | |
|---|---|---|---|---|---|---|---|---|
| G5-C6 | G6-C6 | $V_C^{SE}$ | G5-C6 | G6-C6 | $V_C^{SE}$ | G5-C6 | G6-C6 | $V_C^{SE}$ |
| 0.015 | 0.052 | 0.001 | 0.069 | 0.046 | 0.005 | 0.250 | 0.040 | 0.014 |

## Appendix B.7 Double-Barrier Model

The DNA conductance data were fit using a double-barrier transmission model that includes coherent and incoherent transport,[24] where the conductance ($G$) and the effective resistance ($R_{tot}$) are given by

$$\frac{1}{G} = R_{tot} = R_0 + \frac{h}{e^2 T_{GG}} \frac{2n+1}{1 - 2e^{-B(2n+1)}\cos(C(2n+1))} \qquad \textbf{Equation B.1}$$

This model was used earlier to describe the measured resistance in G-block DNA duplexes.[25-27] $R_0$ is the effective resistance of the molecule-electrode contacts, and it includes the resistance between the electrodes and the AT base pairs. The second term on the right side of Equation B.1 describes mixed coherent and incoherent transport from the AT base pair through the G-blocks; it includes a coherent transport correction that produces conductance oscillations. $T_{GG}$ is the probability of incoherent transmission through the π-stack. In the double-barrier model, the inelastic ('phase randomizing') events are associated with the carrier reservoir, and, in the molecular analogy, the phase randomizing events are likely associated with the 'cross-strand' charge flow. The double barrier model includes coherence effects through a 'correction' term, associated with parameters $B$ and $C$. The parameter $B = {w_0}/{(v\,\tau_i)}$ describes the decrease in the coherent mechanism with distance, where $w_0$ is the inter-base pair distance, $v$ is the velocity of the charge carrier, and $\tau_i$ is the scattering time. The $C$ parameter represents the change in phase of the charge carrier for coherent transport, and $C = {2w_0\sqrt{2mE}}/{\hbar}$ where $m$ is the effective mass of the charge carrier and $E$ is its energy. Fits of the experimental data using Equation B.1 are shown in Figure 3.4 and the fitted parameters appear in Table B.5. The presence of oscillations has been interpreted as a signature that reflects a coherent-resonant (ballistic) mechanism,[6,28,29]

and the smaller amplitude of oscillations for PNA indicates a smaller relative contribution from the fully delocalized G-blocks to the overall conductance.

The data were fit by this model in a two-step process. In the first step, we estimated the contact resistance (between the molecule and the electrode), the PNA data were fit by a sequential hopping model based on the steady-state flux method.[30,31] The model is given by

$$\frac{1}{G} = R_{tot} = R_0 + \frac{2n+1}{e^2\rho(E_F)}k^{-1}e^{E_a/k_BT} \qquad \textbf{Equation B.2}$$

where $R_0$ is the effective resistance of the molecule-electrode contact, $e$ is the electron charge, $\rho(E_F)$ is the density of states at the Fermi level, $k$ is the hole transfer rate constant between hopping sites, $E_a$ is the activation energy, $k_B$ is Boltzmann's constant, and $T$ is the temperature. In the second step we used the contact resistance $R_0$ from step 1 as an initial guess for $R_0$ and we assumed similar carrier energies for PNA and DNA (i.e., similar $C$ values) to constrain the fit by Equation B.1. The fitting parameters are shown in Table B.5.

**Table B.5 Best fit parameters for the data in Figure 3.4 using Equation B.1.**

| | DNA 5' | DNA 3' | PNA N-end |
|---|---|---|---|
| $R_0$ /MΩ | 1.26 | 0.65 | 0.15 |
| $B$ | 0.11 | 0.19 | 0.32 |
| $C$ | 1.38 | 1.40 | 1.40 |
| $T_{GG}$ | 0.03 | 0.19 | 1.23 |
| Slope/MΩ | - | - | 0.02 |

The parameters found in the fitting indicate that the contact resistance $R_0$ is larger for DNA than for N-linked PNA. 5' DNA has a larger resistance than 3' DNA. The decrease in molecule-lead coupling for DNA compared to PNA is attributed to the structural fluctuations of the duplex ends that manifested in the MD simulations.

The single barrier transmission factor $T_{GG}$ is determined by the cross-strand, intra-strand, and AT-GC couplings (Table 3.3). Given the similar HOMO energies and intra-strand couplings for 3'-DNA and 5'-DNA, the small $T_{GG}$ value found for 5'-DNA is believed to arise from its much smaller 5' cross-strand coupling. Figure B.11 shows contour plots that indicate the correlation among the fitting parameters. Although the $R_0$ and $T_{GG}$ parameters in Equation B.1 are coupled in the fitting, the uncertainty in the best fit parameters is small enough that it does not change the above interpretations. The large $T_{GG}$ value for PNA arises from the strong coupling among G base pairs and between AT and GC pairs.

The effects of coherent transport through the cross-strand junction (i.e., the even-odd effect) manifest in the *B* and *C* parameters of Equation B.1. The *B* parameter reflects the strength of the dephasing as a function of distance and affects the magnitude of this coherent correction to the transmission. The small value of *B* for 5' DNA indicates that the duplex has a larger coherent contribution to the overall conductance, which accounts for the larger amplitude of the even-odd effect that is seen experimentally. As the value of *B* increases, the coherent contribution becomes less important and $T_{GG}$ dominates, which leads to a dampening of the conductance oscillations. For 3'-DNA, the coherent contribution decreases and seems to arise from the increase in the cross-strand coupling, which is the only significant difference between the 3' and 5' G-block DNAs.[6] The *C* parameter is similar in 5'-DNA and 3'-DNA, which indicates that the hole energies are not too different among the species. For N-linked PNA, the strong cross-strand coupling and the molecule-lead coupling reduces the relative importance of the coherent correction, resulting in the largest *B* value among the structures.[6,28,29]

Figure B.11 shows the correlation between the parameters $R_0$ and $T_{GG}$. The parameters used in Table B.5 guarantee a good fit as described by the parameter $\chi^2$.

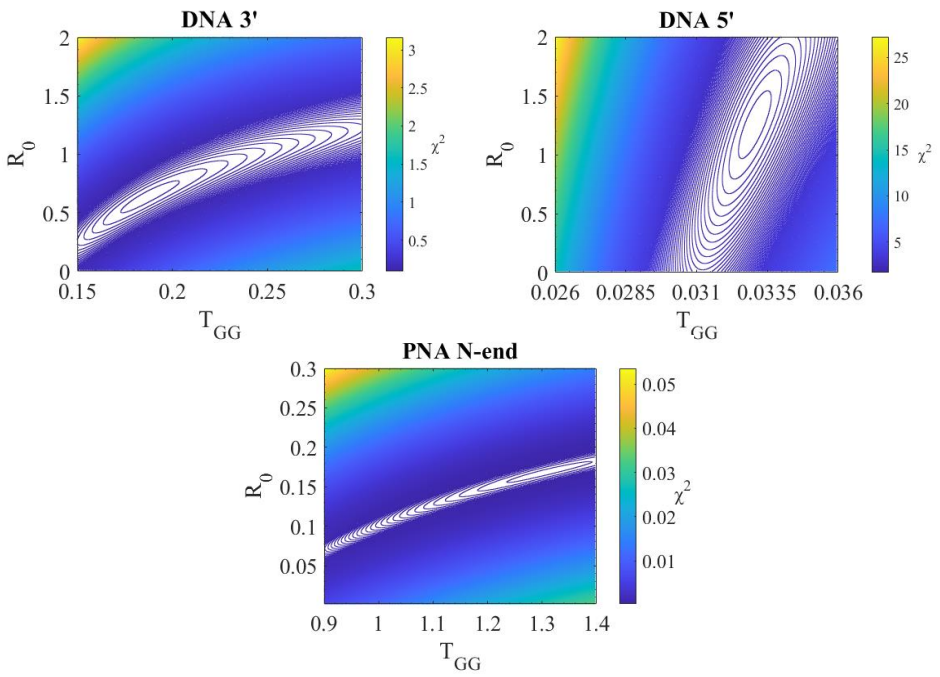


**Figure B.11 Contour plots of fitting parameters $R_0$ and $T_{GG}$. $B$ and $C$ are fixed at the values given in Table B.5.**

The authors acknowledge support from the National Science Foundation (1412030 to D.H.W. and 1413202 to C.A.). E.B. acknowledges a fellowship from the Pittsburgh Quantum Institute during part of this work.

## Appendix B.8 References


1. Beall, E.; Ulku, S.; Liu, C.; Wierzbinski, E.; Zhang, Y.; Bae, Y.; Zhang, P.; Achim, C.; Beratan, D. N.; Waldeck, D. H., Effects of the backbone and chemical linker on the molecular conductance of nucleic acid duplexes. *J. Am. Chem. Soc.* **2017**, 139 (19), 6726-6735.
2. Nielsen, P. E., *Peptide nucleic acids: protocols and applications*. Horizon Bioscience: Wymondham, **2004**.
3. Hegner, M.; Wagner, P.; Semenza, G., Ultralarge atomically flat template-stripped Au surfaces for scanning probe microscopy. *Surf. Sci.* **1993**, 291 (1-2), 39-46.
4. Beall, E.; Yin, X.; Waldeck, D. H.; Wierzbinski, E., A scanning tunneling microscope break junction method with continuous bias modulation. *Nanoscale* **2015**, 7 (36), 14965-14973.
5. Chen, F.; Li, X.; Hihath, J.; Huang, Z.; Tao, N., Effect of anchoring groups on single-molecule conductance: comparative study of thiol-, amine-, and carboxylic-acid-terminated molecules. *J. Am. Chem. Soc.* **2006**, 128 (49), 15874-15881.
6. Liu, C.; Xiang, L.; Zhang, Y.; Zhang, P.; Beratan, D. N.; Li, Y.; Tao, N., Engineering nanometre-scale coherence in soft matter. *Nat. Chem.* 2016, 8 (10), 941-945.
7. Jorgensen, W. L.; Chandrasekhar, J.; Madura, J. D.; Impey, R. W.; Klein, M. L., Comparison of simple potential functions for simulating liquid water. *J. Chem. Phys.* **1983**, 79 (2), 926-935.
8. Hart, K.; Foloppe, N.; Baker, C. M.; Denning, E. J.; Nilsson, L.; MacKerell Jr, A. D., Optimization of the CHARMM additive force field for DNA: Improved treatment of the BI/BII conformational equilibrium. *J. Chem. Theory Comput.* **2012**, 8 (1), 348-362.
9. Jasiński, M.; Feig, M.; Trylska, J., Improved force fields for peptide nucleic acids with optimized backbone torsion parameters. *J. Chem. Theory Comput.* **2018**, 14 (7), 3603-3620.
10. Darden, T.; York, D.; Pedersen, L., Particle mesh Ewald: An N· log (N) method for Ewald sums in large systems. *J. Chem. Phys.* **1993**, 98 (12), 10089-10092.
11. Phillips, J. C.; Braun, R.; Wang, W.; Gumbart, J.; Tajkhorshid, E.; Villa, E.; Chipot, C.; Skeel, R. D.; Kale, L.; Schulten, K., Scalable molecular dynamics with NAMD. *J. Comput. Chem.* **2005**, 26 (16), 1781-1802.
12. Martyna, G. J.; Tobias, D. J.; Klein, M. L., Constant pressure molecular dynamics algorithms. *J. Chem. Phys*. **1994**, 101 (5), 4177-4189.
13. Feller, S. E.; Zhang, Y.; Pastor, R. W.; Brooks, B. R., Constant pressure molecular dynamics simulation: the Langevin piston method. *J. Chem. Phys*. **1995**, 103 (11), 4613-4621.
14. Michaud-Agrawal, N.; Denning, E. J.; Woolf, T. B.; Beckstein, O., MDAnalysis: a toolkit for the analysis of molecular dynamics simulations. *J. Comput. Chem.* **2011**, 32 (10), 2319-27.

15. Gowers, R. J.; Linke, M.; Barnoud, J.; Reddy, T.; Melo, M. N.; Seyler, S.; DombDski, J.; Dotson, D.; Buchoux, S.; Kenney, I. M.; Beckstein, O. In *MDAnalysis: A Python Package for the Rapid Analysis of Molecular Dynamics Simulations*, Benthall, S.; Rostrup, S., Eds. Proc. of the 15th Python in Science Conf.: **2016**; 98 - 105.

16. Hatcher, E.; Balaeff, A.; Keinan, S.; Venkatramani, R.; Beratan, D. N., PNA versus DNA: Effects of structural fluctuations on electronic structure and hole-transport mechanisms. *J. Am. Chem. Soc.* **2008**, 130 (35), 11752-11761.

17. Lu, X. J.; Olson, W. K., 3DNA: a software package for the analysis, rebuilding and visualization of three-dimensional nucleic acid structures. *Nucleic Acids Res*. **2003**, 31 (17), 5108-5121.

18. Humphrey, W.; Dalke, A.; Schulten, K., VMD: visual molecular dynamics. *J. Mol. Graphics* **1996**, 14 (1), 33-38.

19. Senthilkumar, K.; Grozema, F. C.; Guerra, C. F.; Bickelhaupt, F. M.; Lewis, F. D.; Berlin, Y. A.; Ratner, M. A.; Siebbeles, L. D., Absolute rates of hole transfer in DNA. *J. Am. Chem. Soc.* **2005**, 127 (42), 14894-14903.

20. Peverati, R.; Truhlar, D. G., Improving the accuracy of hybrid meta-GGA density functionals by range separation. *J. Phys. Chem. Lett*. **2011**, 2 (21), 2810-2817.

21. Zheng, J.; Xu, X.; Truhlar, D. G., Minimally augmented Karlsruhe basis sets. *Theor. Chem. Acc.* **2011**, 128 (3), 295-305.

22. Roca-Sanjuán, D.; Rubio, M.; Merchán, M.; Serrano-Andrés, L., Ab initio determination of the ionization potentials of DNA and RNA nucleobases. *J. Chem. Phys.* **2006**, 125 (8), 084302.

23. Kawai, K.; Majima, T., Hole transfer kinetics of DNA. *Acc. Chem. Res.* **2013**, 46 (11), 2616-2625.

24. Buttiker, M., Coherent and sequential tunneling in series barriers. *IBM J. Res. Dev.* **1988**, 32 (1), 63-75.

25. Xiang, L.; Palma, J. L.; Bruot, C.; Mujica, V.; Ratner, M. A.; Tao, N., Intermediate tunnelling–hopping regime in DNA charge transport. *Nat. Chem.* **2015**, 7 (3), 221.

26. Artés, J. M.; Li, Y.; Qi, J.; Anantram, M.; Hihath, J., Conformational gating of DNA conductance. *Nat. Commun*. **2015**, 6 (1), 1-8.

27. Bruot, C.; Palma, J. L.; Xiang, L.; Mujica, V.; Ratner, M. A.; Tao, N., Piezoresistivity in single DNA molecules. *Nat. Commun*. **2015**, 6 (1), 1-8.

28. Kim, H.; Kilgour, M.; Segal, D., Intermediate Coherent–Incoherent Charge Transport: DNA as a Case Study. *J. Phys. Chem. C* **2016**, 120 (42), 23951-23962.

29. Karasch, P.; Ryndyk, D. A.; Frauenheim, T., Vibronic dephasing model for coherent-to-incoherent crossover in DNA. *Phys. Rev. B* **2018**, 97 (19), 195401.

30. Segal, D.; Nitzan, A.; Ratner, M.; Davis, W. B., Activated conduction in microscopic molecular junctions. *J. Phys. Chem. B* **2000**, 104 (13), 2790-2793.

31. Nitzan, A., The relationship between electron transfer rate and molecular conduction 2. The sequential hopping case. *Isr. J. Chem.* **2002**, 42 (2-3), 163-166.

# Appendix C Hall Effect Measurements

## Appendix C.1.1 Device Structure and Cleaning

Hall effect devices were fabricated as reported previously.[1] Figure C.1a shows an assembled device with PDMS cell (denoted by the white outline and shading) mounted on a chip. A schematic of the Hall device (denoted by the red outline in Figure C.1a) is shown in Figure C.1b. Figure C.1c shows a cross-section of the structure of the active area.

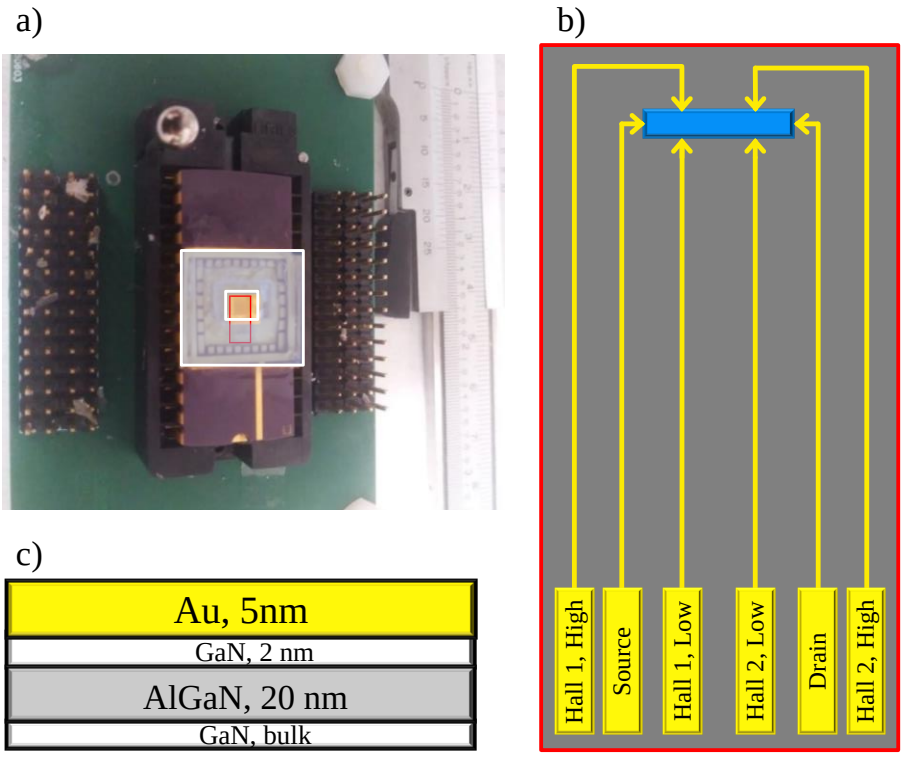


**Figure C.1 Panel (a) shows an assembled device (red outline) and PDSM cell (shaded area). Panel (b) presents a top view scheme of the the device. The blue area denotes the active channel of the device. Electrical leads are shown in gold; the large rectangles indicate the contact pads for the wirebonding of**

**electical connection from the device to the chip. From left to right, the connections are Hall probe 1a, Source, Hall probe 1b, Hall probe 2b, Drain, and Hall probe 2a. Panel c shows the cross section structure for the active channel of the device. The 2DEG and source-drain current is between the bulk GaN and the AlGaN layer.**

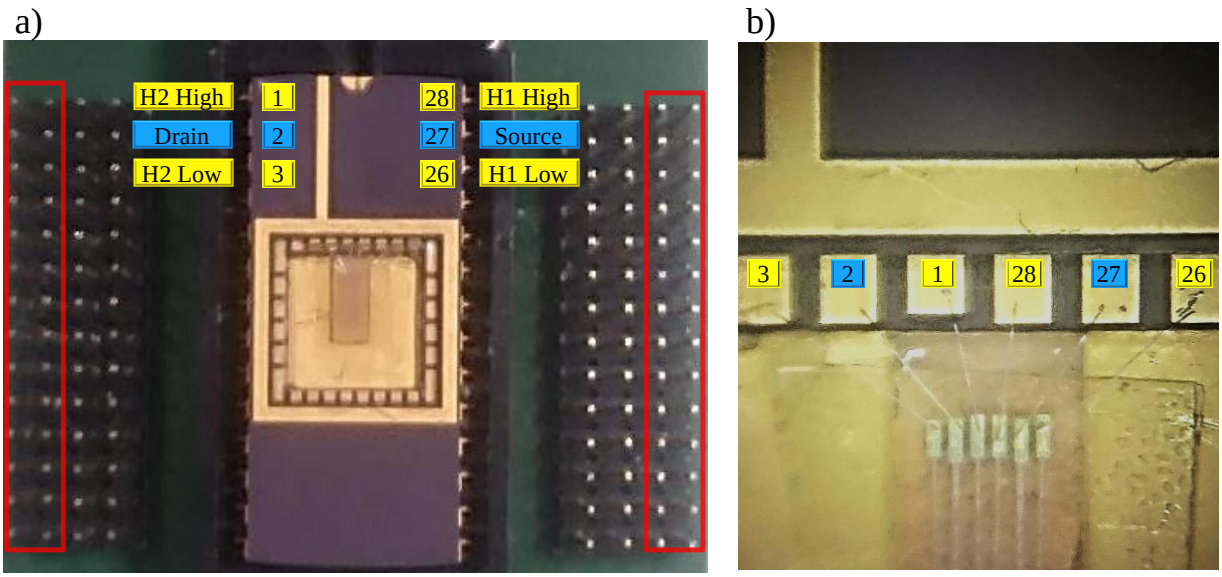


**Figure C.2 Panel (a) shows the pin connections of the chip carrier for a typical Hall measurement setup. The pegs within the red rectangles are all electrically connected. The remaining two pegs in each row on either side are electrically identical pairs. Panel (b) shows the typical wiring arrangement for wirebonding of the device to the chip. Pin 1 is denoted by the smaller square on the chip.**

The devices have been coated in MICROPOSIT S1813 photoresist, which must be thoroughly removed prior to SAM formation. This was done by heating in 1-methyl-2-pyrilidone (NMP) at 80°C for at least 5 hours. The devices were then rinsed with NMP, acetone, isopropanol, ethanol, water, and dried under Ar stream. Removal of photoresist was confirmed by SEM and AFM. It is essential to note that this cleaning was not always sufficient, so the confirmation of a clean, smooth surface is essential prior to any SAM formation, see Figure C.3. Once a clean surface is obtained, devices should be promptly incubated under conditions suitable for SAM formation of the analyte molecule.

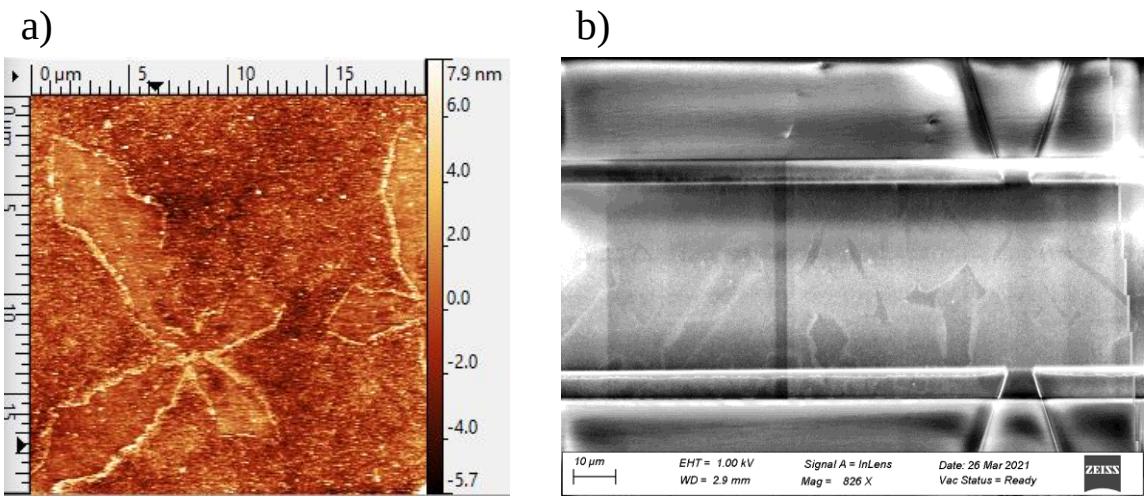


**Figure C.3 AFM (a) and SEM (b) images of a device channel with significant photoresist residue. Further cleaning is required in this case.**

The device is attached to a standard chip (28-lead Sidebraze, Global Chip Materials) using double-sided tape. Electrical connections were accomplished by wirebonding with Aluminum.

### Appendix C.1.2 Polydimethylsiloxane (PDMS) Cell Assembly

To facilitate measurements in solution, a PDMS cell was constructed around the device. PDMS (Sylgard 184) was mixed as directed, degassed under vacuum, and poured into an aluminum mold (see Figure C.4) and allowed to cure for at least 24 hours at 80°C.

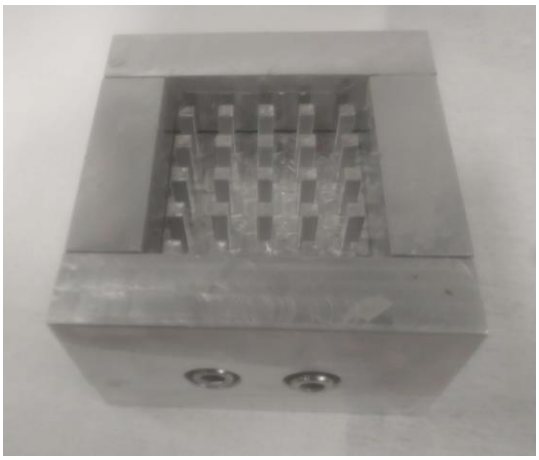

**Figure C.4 Mold for making PDMS cells. While this mold has an inner cavity of 4x4 cm and results in a PDMS square of 8x8x10 mm with a cell of 3x3x10 mm, more ideal dimensions should instead yield PDMS squares of approximately 2x2x0.5 cm with a cell of 5x5x5 mm.**

The PDMS cell is removed from the mold and carefully placed onto the chip with the Hall device so that the active channel of the device is uncovered. It is best to have the device recessed in the cavity of the chip and the PDMS cell is attached to the perimeter of the recession. Fresh PDMS was applied from a syringe to adhere the cell to the chip, being very careful to not sever the wirebonds, as the weight of the uncured PDMS alone can cause them to separate (although they must be electrically isolated from solution during the Hall measurement), nor coat the active channel. The PDMS was cured for at least 18 hours at 80°C.

### Appendix C.1.3 Hall Measurements

Hall measurements were conducted using a Keithley 2636A Source Meter and a Keithley 2182A Nanovoltmeter. Both are allowed to reach a stable internal temperature, ≈ 3 hours. A custom LabVIEW script is used to conduct the measurements, see Appendix C.1.5. Pipette in any desired solution to completely fill the cell, ≈100-200μL. A glass microscope slide coverslip (2.5cm by 2.5cm by ≈0.2mm), coated with 5nm Ti and 80nm Au, evaporated using Plassys

Electron Beam Evaporator, is placed on top of the cell, with the uncoated side towards the solution. Ensure that no air bubble is present and that there is not solution overflow.

The Keithley 2636A Source Meter provides both the current driven through the 2DEG channel ('Channel A' in Figure C.5) and the polarizing 'Gate' voltage ('Channel B' in Figure C.5. Typically, 50 μA of current driven with the each application of the Gate voltage having a duration of ≈10 s ('Pulse On/Off' in Figure C.6) for each Gate voltage step are good starting values. The maximum Gate voltage ('Gate Range' in Figure C.6) should never exceed ±20 V.

**Appendix C.1.4 Analysis**

The Hall voltage data for the 'forward' ($I_{SD}$ = +50 μA) and 'reverse' ($I_{SD}$ = -50 μA) applied current is averaged by the equation:

$$\boldsymbol{Hall\ Voltage = \frac{\Delta V_{Hall}^{Forward} - \Delta V_{Hall}^{Reverse}}{2}} \qquad \textbf{Equation C.1}$$

where $\Delta V_{Hall} = V_{peak} - V_{baseline}$. To minimize impact of any change in the baseline over time, $V_{baseline}$ is taken as the value immediately prior to the application of a Gate voltage. $V_{peak}$ will frequently display an initial spike concurrent with the application of Gate voltage; this is an artifact of the instruments and should be ignored. However, due to the rapid decay of Hall voltage typically seen, the value for $V_{peak}$ should be taken in the first 0.5 s (≈5 data points) after the Gate voltage is applied. The slope of the plot of Hall Voltage vs Gate voltage, see Figure 4.2c-d, is indicative of the intensity of the CISS response, as disucssed in Chapter 4.

## Appendix C.1.5 LabVIEW Code for Hall Measurements

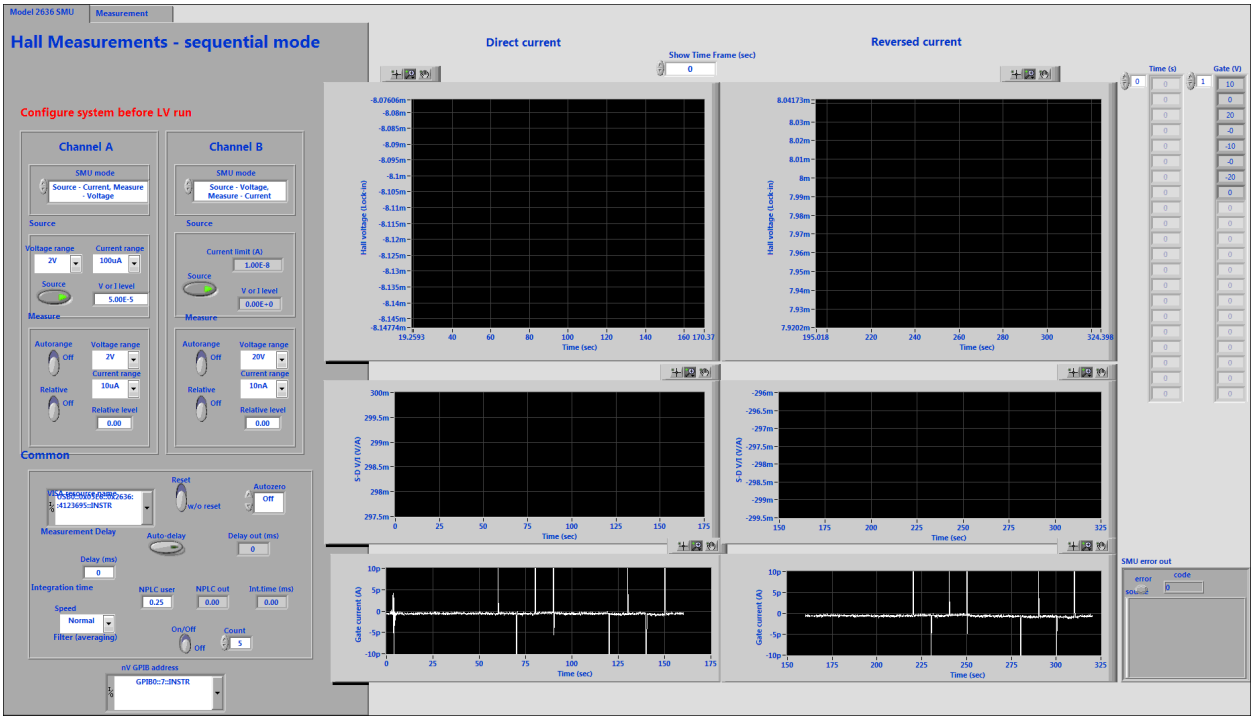


**Figure C.5 LabVIEW Front panel for the setup of the Source-Drain current for Hall measurements.**

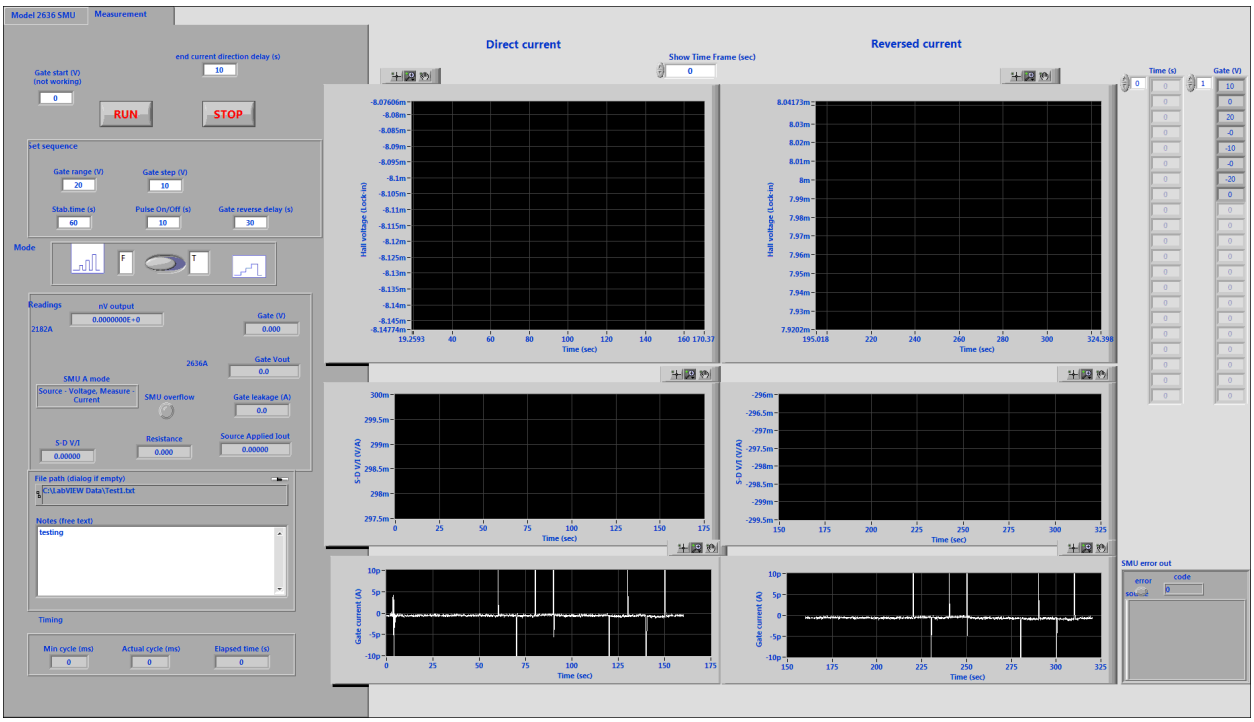


**Figure C.6 LabVIEW Front panel for the setup of the Gate voltages applied for Hall measurements.**

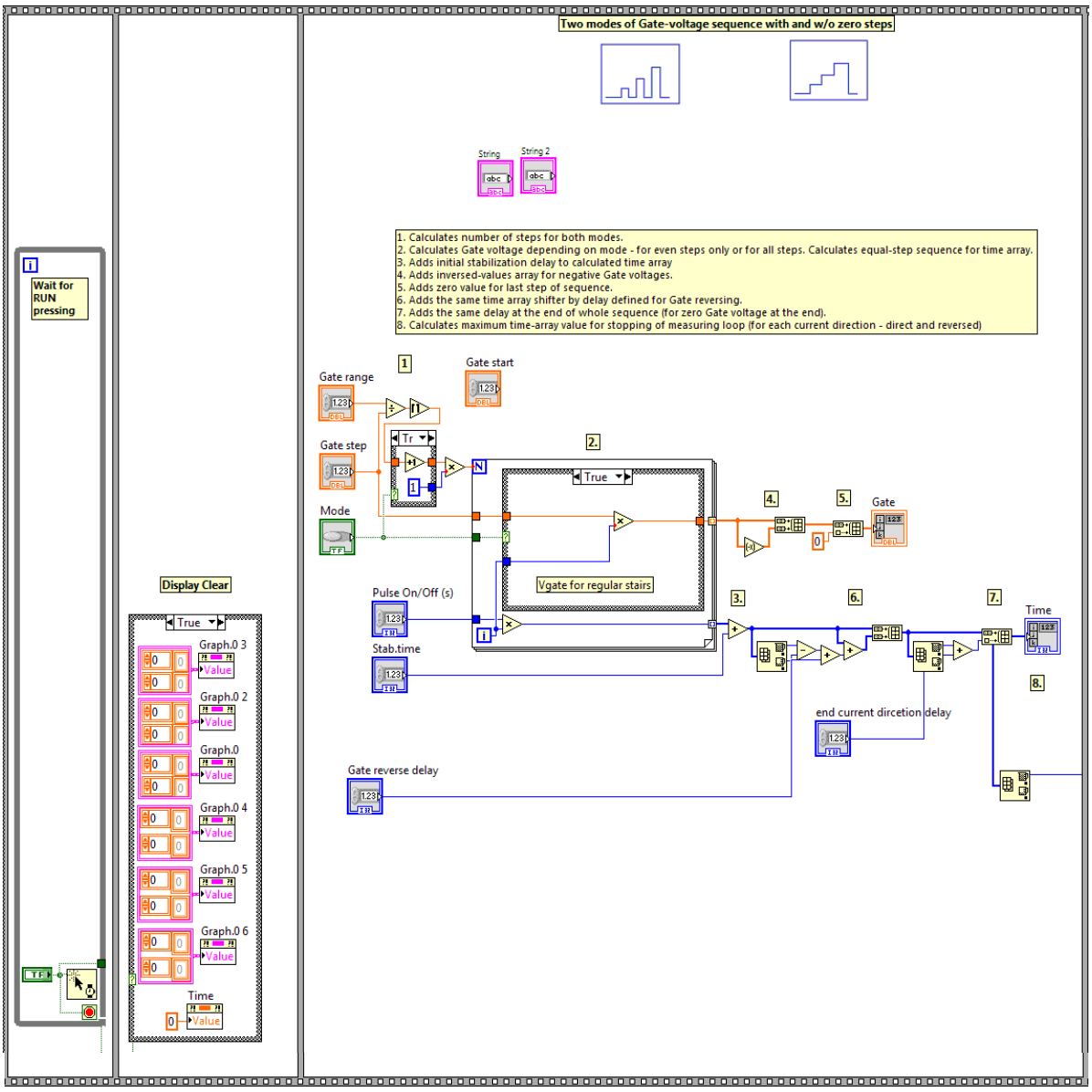


**Figure C.7 LabVIEW Block Diagram for Hall effect measurements.**

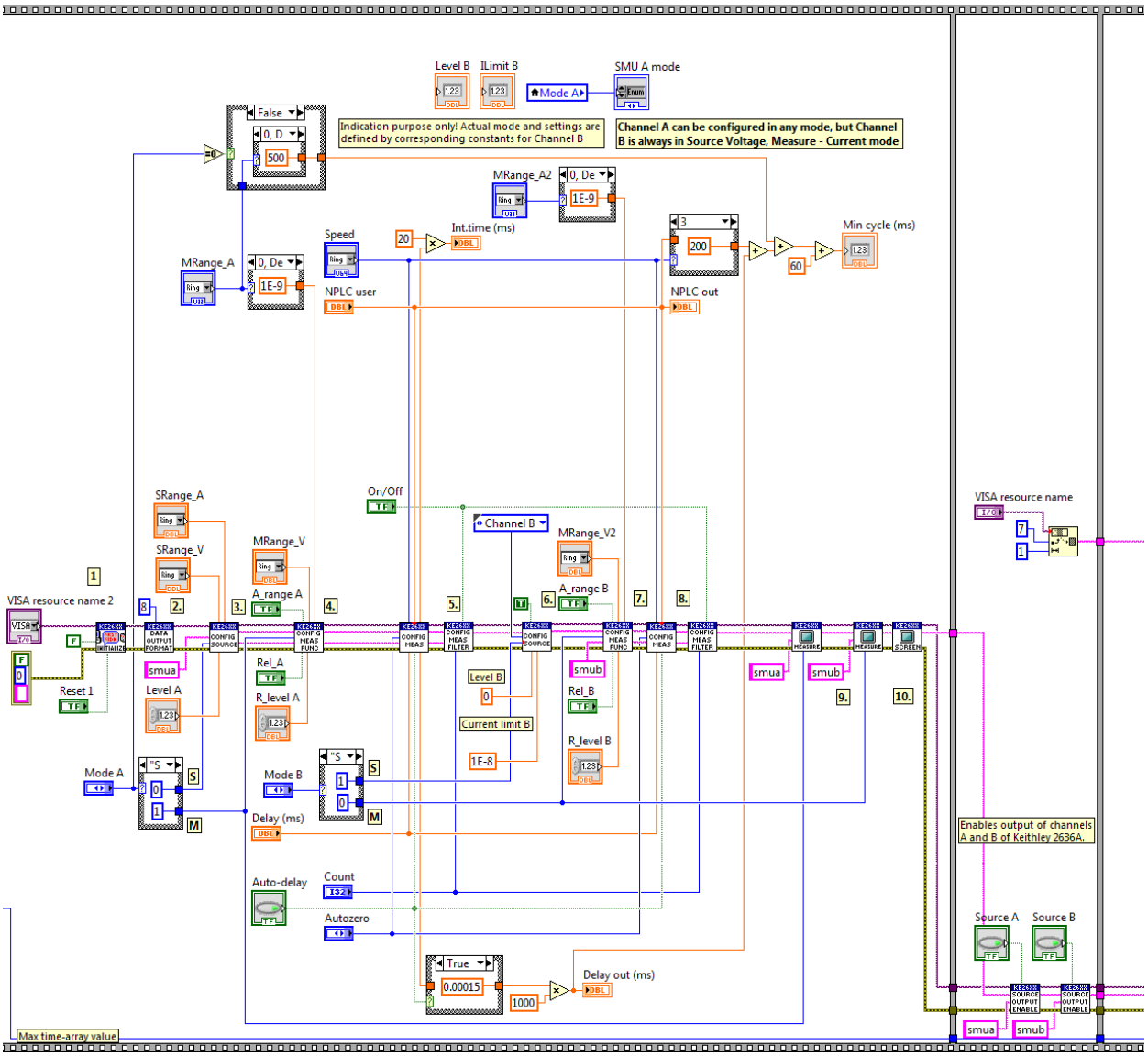


**Figure C.8 LabVIEW Block Diagram for Hall effect measurements.**

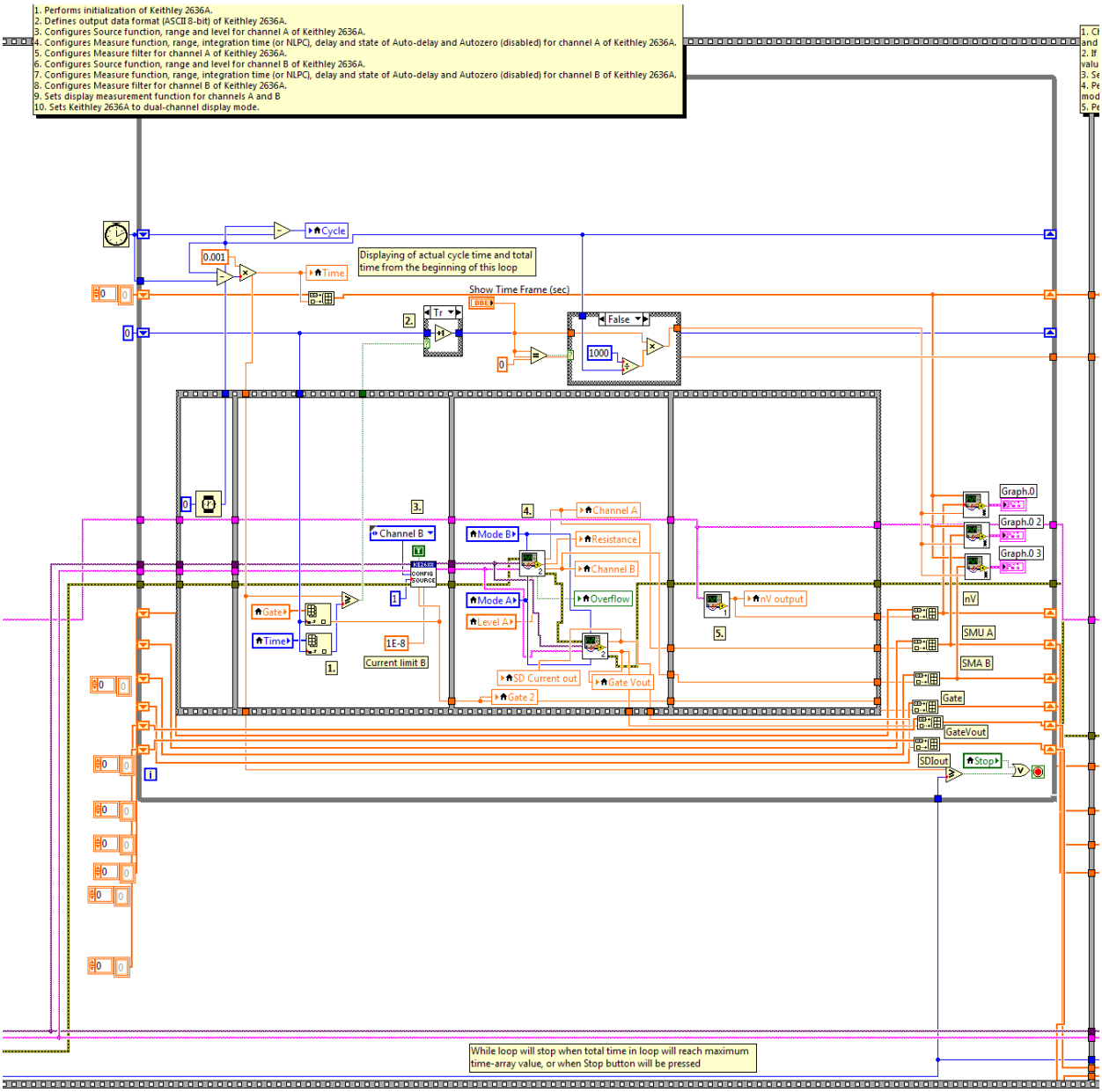


**Figure C.9 LabVIEW Block Diagram for Hall effect measurements.**

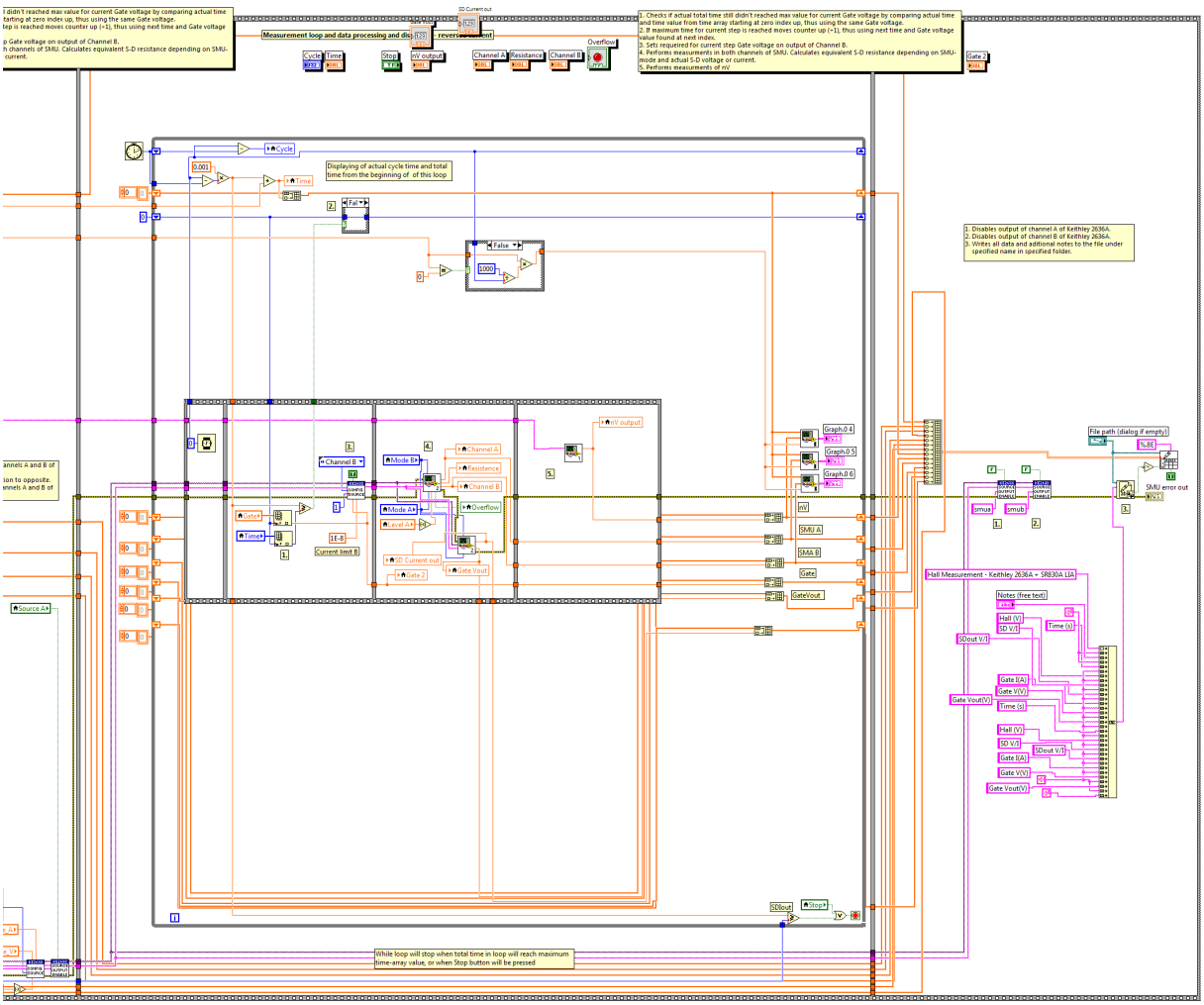

**Figure C.10 LabVIEW Block Diagram for Hall effect measurements.**

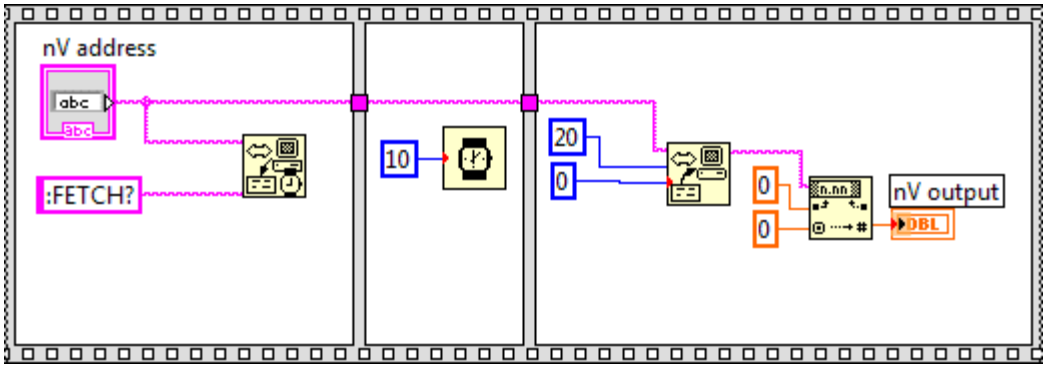


**Figure C.11 LabVIEW Block Diagram for Hall effect measurements. SubVI 2182A single measurement.vi.**

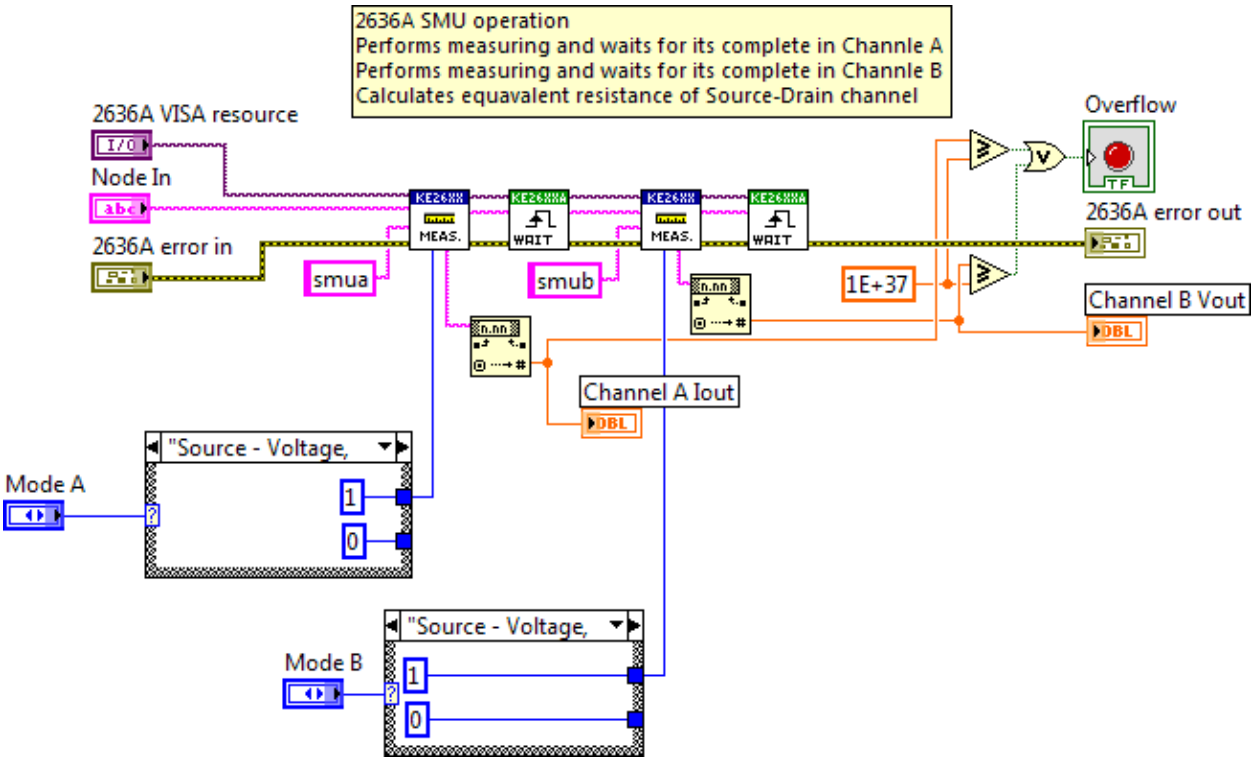


**Figure C.12 LabVIEW Block Diagram for Hall effect measurements. SubVI 2636A single measurement_full WITH OPP SOURCE-MEASURE.vi.**

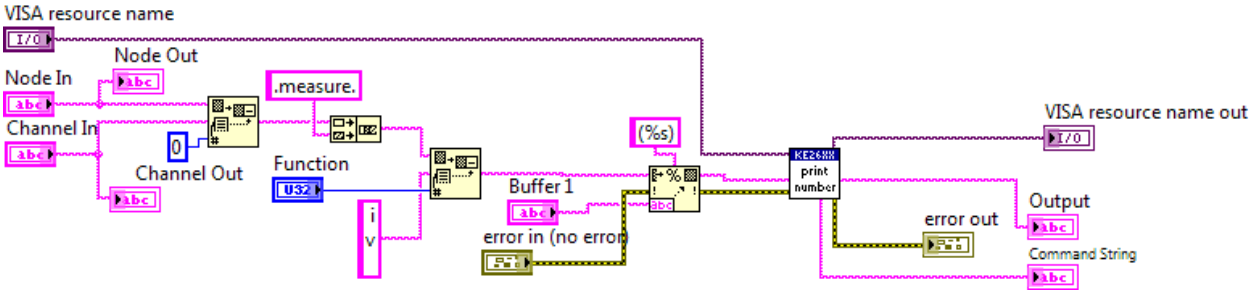


**Figure C.13 LabVIEW Block Diagram for Hall effect measurements. SubVI Keithley 2600 Series.lvlib:Measure no buffer.vi.**

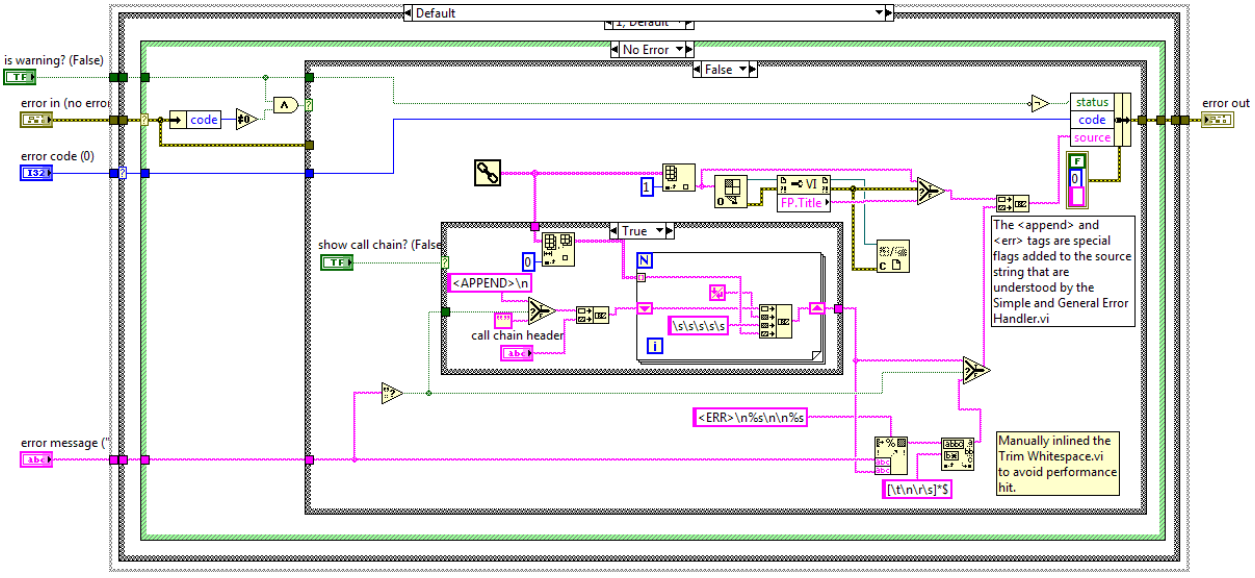


**Figure C.14 LabVIEW Block Diagram for Hall effect measurements. SubVI Error Cluster From Error Code.vi.**

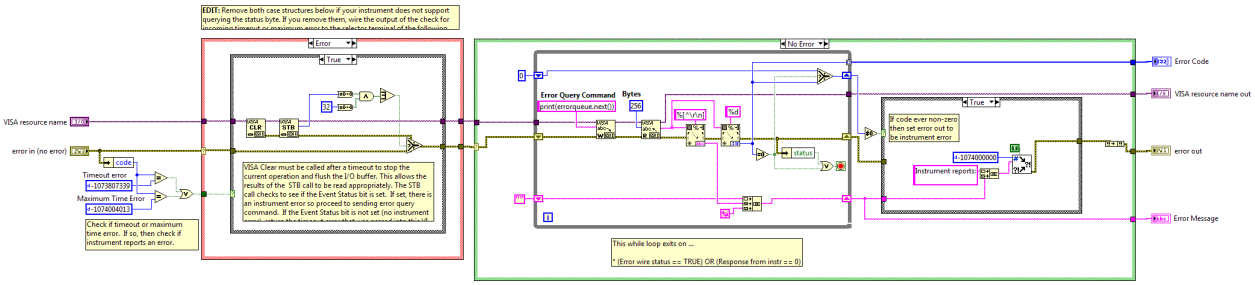


**Figure C.15 LabVIEW Block Diagram for Hall effect measurements. SubVI Keithley 2600 Series.lvlib:Error Query.vi.**

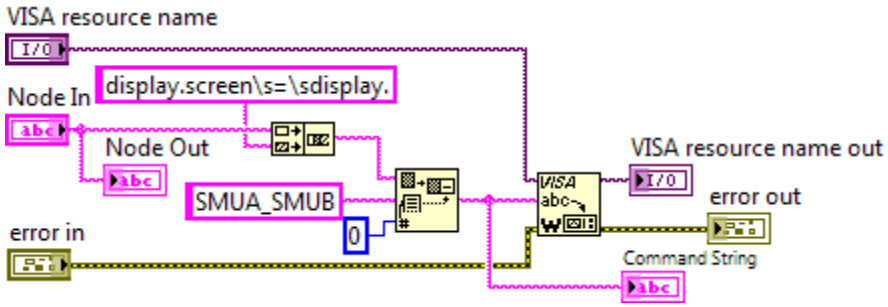


**Figure C.16 LabVIEW Block Diagram for Hall effect measurements. SubVI Keithley 2600 Series.lvlib:Display Dual Screen.vi.**

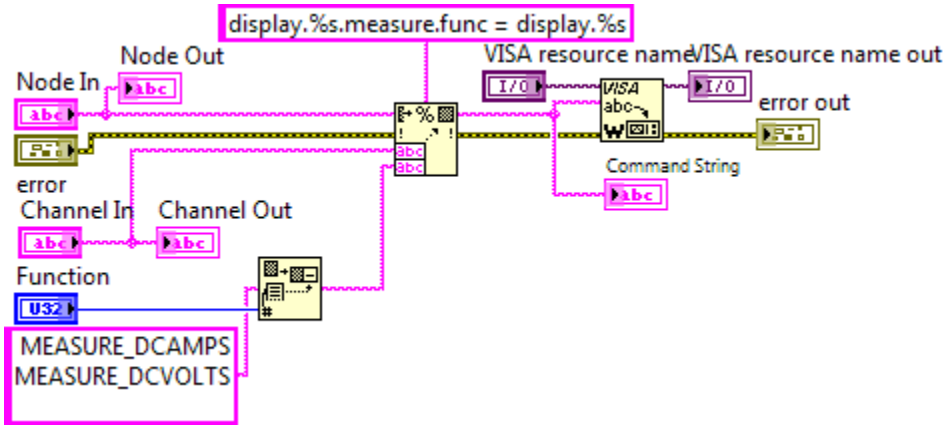


**Figure C.17 LabVIEW Block Diagram for Hall effect measurements. SubVI Keithley 2600 Series.lvlib:Display Measure Function_mod.vi.**

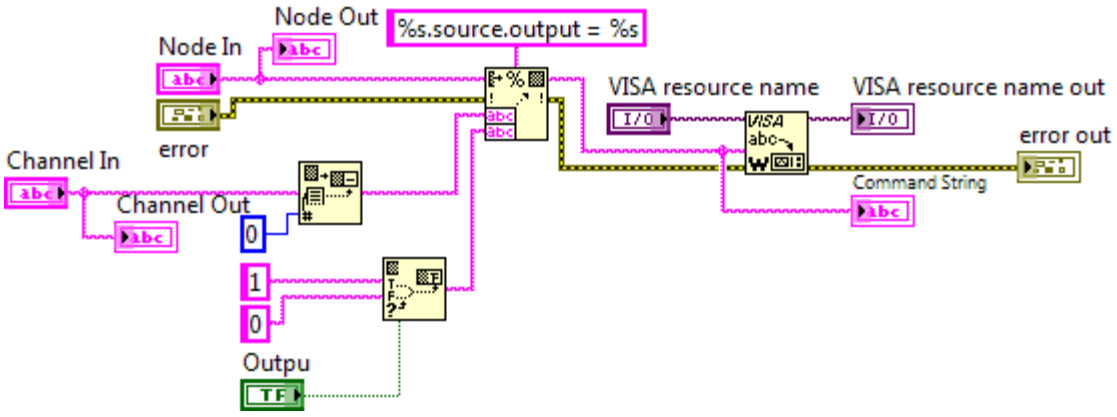


**Figure C.18 LabVIEW Block Diagram for Hall effect measurements. SubVI Keithley 2600 Series.lvlib:Source Output Enable_mod.vi.**

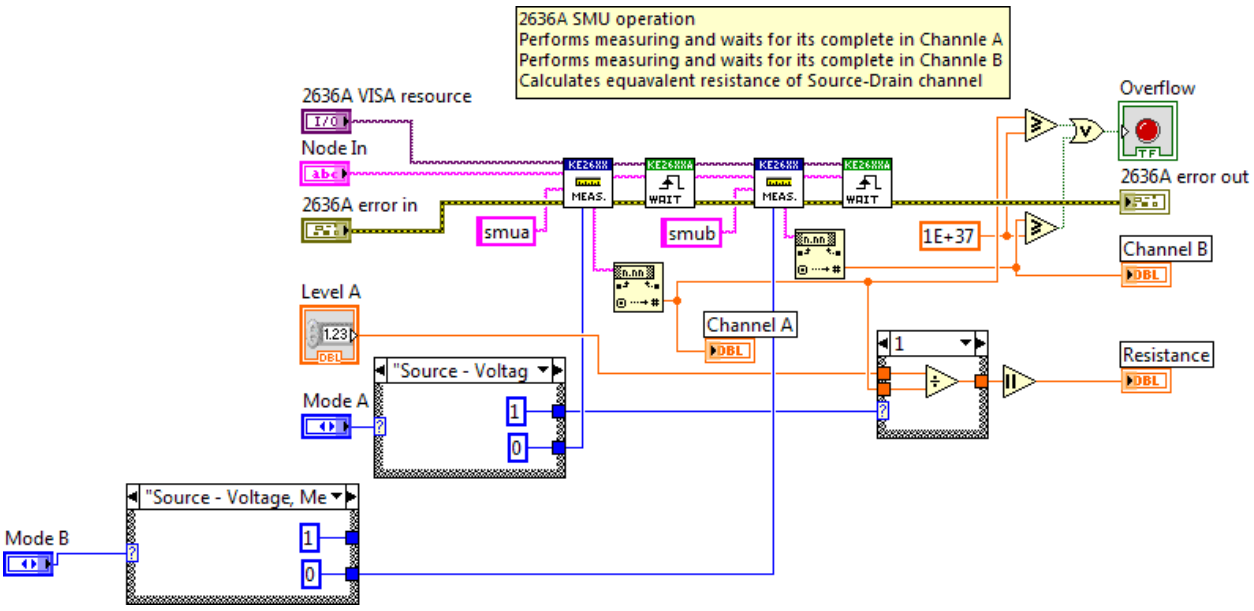


**Figure C.19 LabVIEW Block Diagram for Hall effect measurements. SubVI 2636A single measurement_full.vi.**

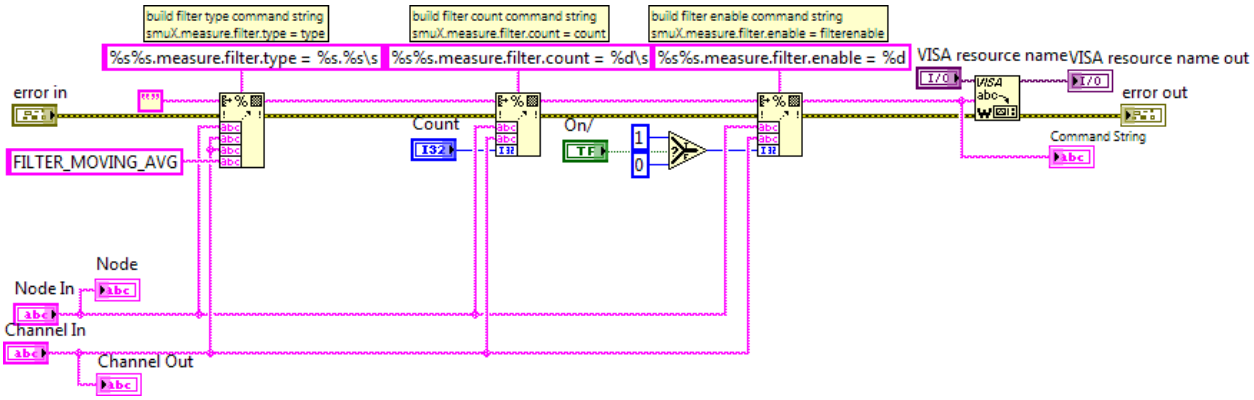


**Figure C.20 LabVIEW Block Diagram for Hall effect measurements. SubVI Keithley 2600 Series.lvlib:Config Measure Filter_mod.vi.**

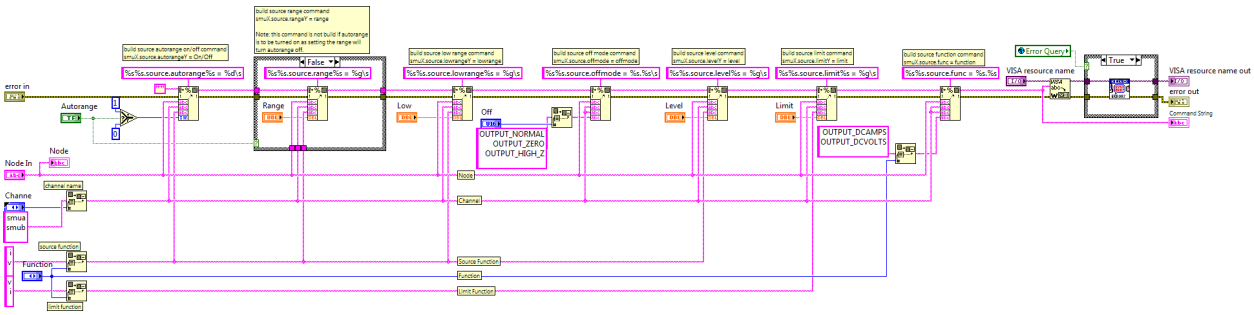

**Figure C.21 LabVIEW Block Diagram for Hall effect measurements. SubVI Keithley 2600 Series.lvlib:Config Source.vi.**

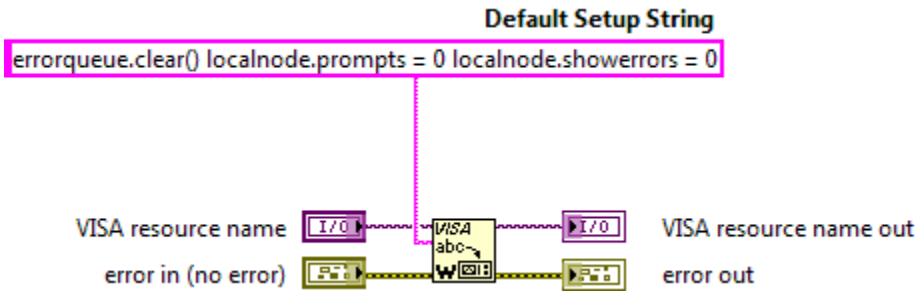


**Figure C.22 LabVIEW Block Diagram for Hall effect measurements. SubVI Keithley 2600 Series.lvlib:Default Instrument Setup.vi.**

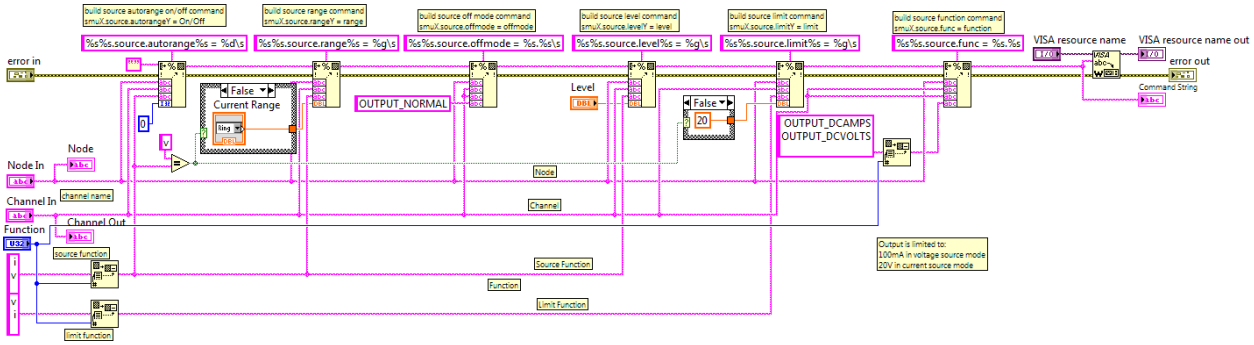


**Figure C.23 LabVIEW Block Diagram for Hall effect measurements. SubVI Keithley 2600 Series.lvlib:Config Source_mod1.vi.**

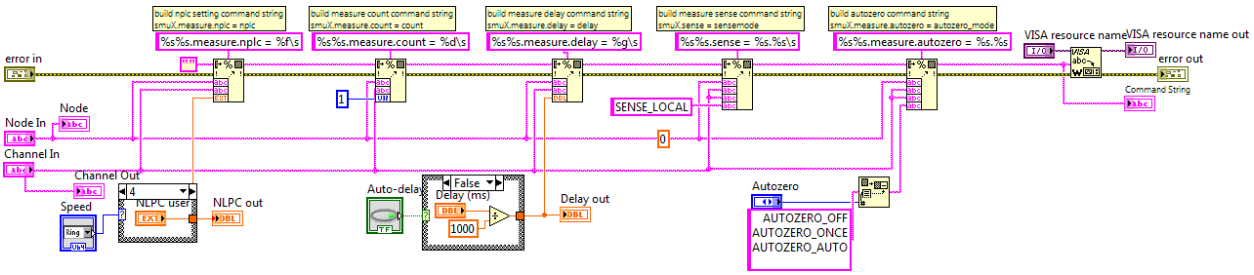


**Figure C.24 LabVIEW Block Diagram for Hall effect measurements. SubVI Keithley 2600 Series.lvlib:Config Measure Settings_mod.vi.**

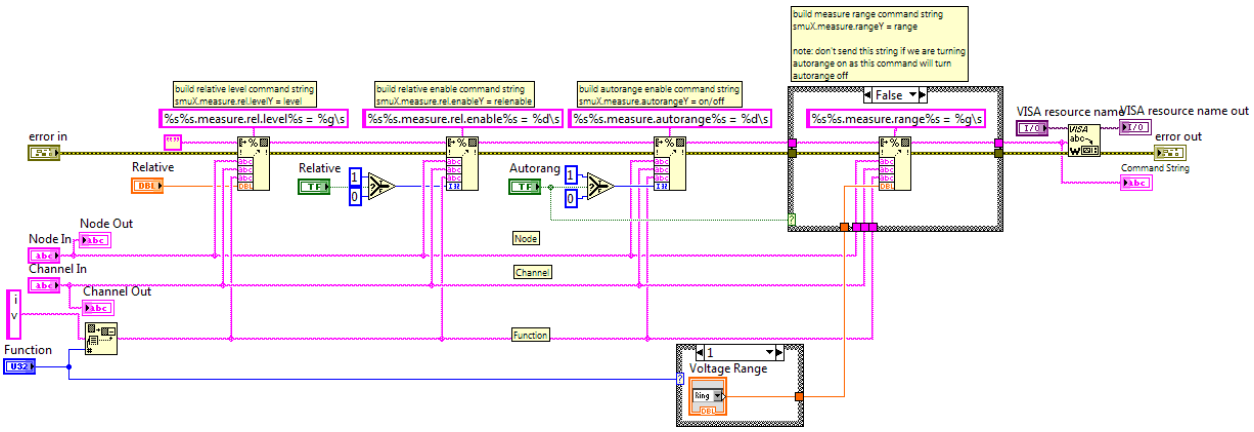


**Figure C.25 LabVIEW Block Diagram for Hall effect measurements. SubVI Keithley 2600 Series.lvlib:Config Measure Function_mod1.vi.**

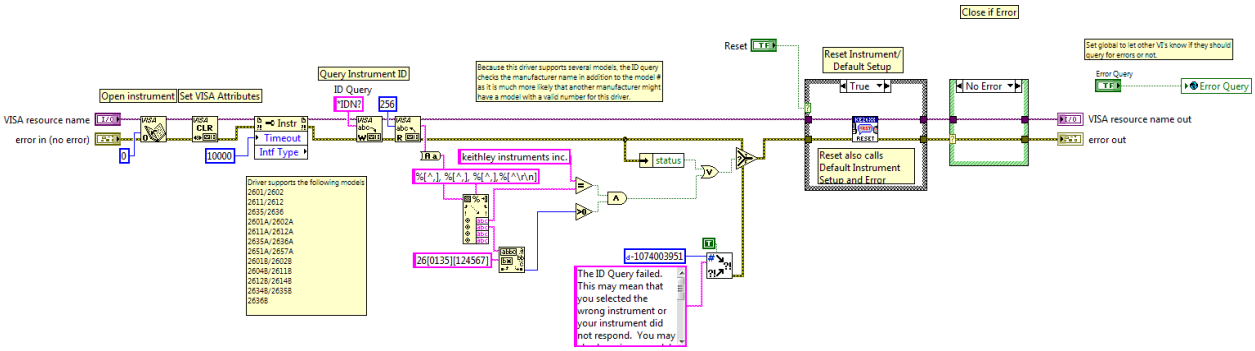


**Figure C.26 LabVIEW Block Diagram for Hall effect measurements. SubVI Keithley 2600 Series.lvlib:Initialize_mod.vi.**

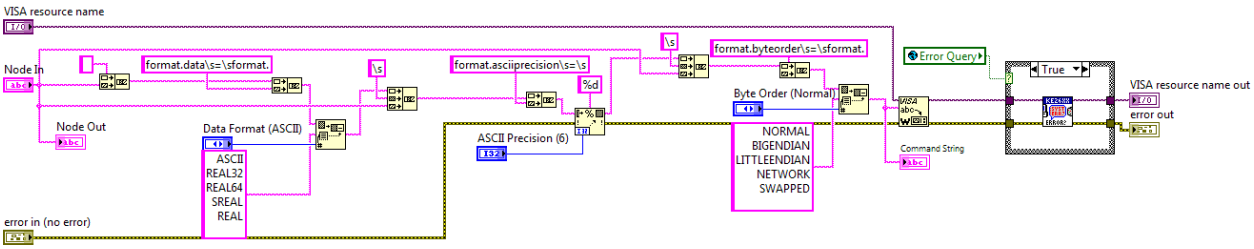


**Figure C.27 LabVIEW Block Diagram for Hall effect measurements. SubVI Keithley 2600 Series.lvlib:Data Output Format.vi.**

## Appendix C.2 References

1. Mishra, S.; Mondal, A. K.; Pal, S.; Das, T. K.; Smolinsky, E. Z. B.; Siligardi, G.; Naaman, R., *J. Phys. Chem. C* **2020,** 124, 10776-10782.

## Appendix D List of Publications

1. Wei, J., Bloom, B. P., Dunlap-Shohl, W. A., **Clever, C.,** Rivas, J. E., Waldeck, D. H., Examining the Effects of Homochirality for Electron Transfer in Protein Assemblies, *J. Phys. Chem. B*, 2023, *127*, 6462–6469.
2. Vadakkayil, A., **Clever, C.,** Kunzler, K. N., Tan, S., Bloom, B. P., Waldeck, D. H., Chiral Electrocatalysts Eclipse Water Splitting Metrics through Spin Control, *Nat. Commun.* 2023, *14*, 1067.
3. **Clever, C.**, Wierzbinski, E., Bloom, B. P., Lu, Y., Grimm, H. M., Rao, S. R., Horne, W. S., Waldeck, D. H., Benchmarking Chiral Induced Spin Selectivity Measurements - Towards Meaningful Comparisons of Chiral Biomolecule Spin Polarizations, *Isr. J. Chem.* 2022, e202200045.
4. **Clever, C.**, Valdiviezo, J., Beall, E., Pearse, A., Bae, Y., Zhang, P., Achim, C., Beratan, D. N., Waldeck, D. H., Delocalization-Assisted Transport through Nucleic Acids in Molecular Junctions, *Biochemistry* 2021, *60*, 1368-1378.
5. Beall, E., Sargun, A., Ulku, S., Bae, Y., Wierzbinski, E., **Clever, C.**, Waldeck, D., Achim, C., Molecular Conductance of Nicked Nucleic Acid Duplexes, *J. Phys. Chem. C* 2018, *122*, 13, 7533-7540.